Spring 2017

A ship advancing in a stratified fluid: the dead water effect revisited

Mehdi Esmaeilpour
University of Iowa

A SHIP ADVANCING IN A STRATIFIED FLUID: THE DEAD WATER EFFECT REVISITED

by

Mehdi Esmaeilpour

A thesis submitted in partial fulfillment
of the requirements for the Doctor of Philosophy
degree in Mechanical Engineering in the
Graduate College of
The University of Iowa

May 2017

Thesis Supervisor: Professor Pablo M. Carrica
Dr. J. Ezequiel Martin

Graduate College
The University of Iowa
Iowa City, Iowa

CERTIFICATE OF APPROVAL

_____

PH.D. THESIS

_____

This is to certify that the Ph.D. thesis of

Mehdi Esmaeilpour

has been approved by the Examining Committee for
the thesis requirement for the Doctor of Philosophy degree
in Mechanical Engineering at the May 2017 graduation.

Thesis Committee: _____
Pablo M. Carrica, Thesis Supervisor.

_____
J. Ezequiel Martin, Thesis Supervisor.

_____
H.S. Udaykumar

_____
James Buchholz

_____
Casey Harwood

ACKNOWLEDGEMENTS

First and foremost I would like to thank my supervisor, Professor Pablo M. Carrica, for all his support, guidance and encouragement in the preparation of this thesis. He accepted me in his research group and spent a lot of time for discussing concepts and reviewing my work. Without his helps this work could not have been accomplished. I would like to acknowledge Dr. Juan E. Martin for all his support and advice during my graduate studies. His expertise in ship hydrodynamics was quite valuable in helping me to achieve the project goals in my work. I would also like to thank my committee members, Professors Udaykumar, Buchholz and Harwood for their dedication to the examination of the thesis. Undoubtedly, their criticism, suggestions and support help me to improve my work significantly. My appreciation also extends to my amazing friends in my research group at the University of Iowa, whom provided a light-hearted working atmosphere and they certainly made work very enjoyable during this journey. I also like to express gratitude to the sponsors of this work. This research was partially supported by the Office of Naval Research, grant N000141310351, with Drs. Ki-Han Kim and Patrick Purtell as program officers. Computations were performed in the SGI Ice-X Spirit at the Air Force Research Laboratory DoD supercomputer resource center and The University of Iowa computer clusters Helium and Neon. Last, but not least, I want to deeply thank my parents, brother and sister who are always giving me support, encouragement and everlasting love during my years of study. Thank you all who have helped me in my life.

ABSTRACT

A computational fluid dynamics (CFD) methodology is presented to predict density stratified flows in the near-field of ships and submarines. The density is solved using a higher-order transport equation coupled with mass and momentum conservation. Turbulence is implemented with a $k-\varepsilon/k-\omega$ based Delayed Detached Eddy Simulation (DDES) approach, enabling explicit solution of larger energy-containing vortices in the wake. Validation tests are performed for a two-dimensional square cavity and the three-dimensional stratified flow past a sphere, showing good agreement with available data. The near-field flow of the self-propelled Research Vessel Athena advancing in a stably stratified fluid is studied, as well as the operation in stratified flow of the notional submarine Joubert BB2 also in self-propelled condition. The resulting density, velocity, pressure and turbulent quantities at the exit plane of the near-field computation contain a description of the relevant scales of the flow and can be used to compute the far-field stratified flow, including internal waves. The generation of internal waves is shown in the case of the submarine for two different conditions, one with the pycnocline located at the propeller centerline, and the second with the pycnocline located slightly below the submarine, concluding that distance to the pycnocline strongly affects the internal wave generation due to the presence of the vessel. It is also shown that, as in the case of surface waves, the generation of internal waves requires energy that results in an increase in resistance. For the case of the surface ship the near field wakes are mostly affected by the separation at the wet transom and propeller mixing. However, in the case of the underwater vessel, the disturbance of the background density profile by the presence of the submarine affects the near-field wakes. Finally, the dead-water phenomenon, which occurs at very

low Froude numbers, is studied for R/V Athena. Though the dead water problem has been studied in the literature using potential flow methods, this thesis presents the first attempt at using computational fluid dynamics (CFD) to analyze the flow. Results show that, while CFD can reproduce trends observed in potential flow studies, viscous effects are significant in the wake and the friction coefficient.

PUBLIC ABSTRACT

A stratified fluid is defined by its mean density variation with depth as a result of any change in salinity and/or temperature. Almost all fluids found in the environment are stratified except on very small scales, and stratified flows are prevalent in various natural environments such as oceans, lakes and estuaries. Therefore, the flow caused by moving objects in these media are of importance and have directed much attention to the subject of stably stratified flows. This thesis presents contributions to simulate stratified flow effects on moving surface ships and submarines. Two different geometries are considered, the research vessel Athena, a surface ship, and the Joubert BB2 geometry, a generic submarine. It is observed that the structure of the stratified flow is completely different from the non-stratified one and the presence of buoyancy forces due to stratification has a substantial effect on the flow development and mixing processes around both geometries and hence influences the flow pattern and results in different resistance forces. Also, when a ship sails slowly in stratified seas she loses steering power and speed and experiences a large change in resistance force. This resistance force can be as high as that of the ship moving two to three times faster in non-stratified flow, a phenomenon known as the dead-water effect. Though the dead water problem has been studied in the literature using potential flow methods, this thesis presents the first attempt at using computational fluid dynamics (CFD) to analyze the flow. Results show that CFD can reproduce trends observed in potential flow studies, and also account for significant viscous effects in the wake and the friction coefficient. Studying this phenomenon shows the design factors for manufacturing a ship with high level of efficiency will change.

TABLE OF CONTENTS

LIST OF TABLES

LIST OF FIGURES

CHAPTER 1 INTRODUCTION

1.1 Overview

Density stratification is an important feature of geophysical flows such as those occurring in the oceans and the atmosphere. Stratification can have significant effects on the mixing process and the dynamics of fluid flows. There are countless examples of stratified flows in nature including rivers, oceans, estuaries, groundwater reservoirs and the atmosphere. Density stratification can even be observed in various manufacturing, chemical, food and industrial processes. Therefore, understanding the dynamics of stratified flows is paramount to predicting and solving relevant fluid mechanics problems in both industry and nature. In lakes and oceans, stratification occurs due to density variations resulting from changes in temperature, salinity or concentration of any other solute, or as a combination of some of these, and it is disrupted by different natural processes including breaking waves, wind action, Coriolis forces and tides, resulting in flows of interest in oceanography. Except at very small scales, all fluid flows in the environment are stratified. Variations in density can occur in any direction, but only vertical stratification is stable in the absence of other forcing. Estuarine flows are examples of situations where horizontal density gradients are important. At their largest scale, planetary flows must consider horizontal density gradients. However, for all the cases of interest for this work, only vertical stable stratification is of interest.

Naval hydrodynamics is a branch of engineering related to the design and operation of surface ships and underwater vehicles, as well as other flows of naval importance. Areas of study in naval hydrodynamics include free surface flows, fluid-structure interaction, propeller efficiency, submarine and ship hull design and others. Improving ship hull design

to enhance hydrodynamic performance is one of the most important goals in this field. The flow field around marine vessels is usually studied using experimental and numerical tools and review of most studies reveals that the fluid is usually considered of constant density and thus the effect of stratification is ignored. However, ships and submarines advancing in stratified media result in problems of importance and produce interesting hydrodynamic phenomena. To understand the structure of stratified flows it is a necessity to become familiar with the dominant parameters of stratified fluid motion, as described in the next sub-sections.

1.1.1 Brunt-Vaisala Frequency

In describing the stratification of a flow, the Brunt-Vaisala or buoyancy frequency is an important parameter. Considering a vertical density gradient $\partial\rho/\partial z$, the buoyancy frequency is defined as $N = \sqrt{-(g/\rho_0)\,(\partial\rho/\partial z)}$, with g the gravity acceleration and ρ_0 a reference density. A physical interpretation of the meaning of the Brunt-Vaisala frequency can be obtained by considering a fluid parcel with volume V and density ρ_0 at elevation z (see Fig. 1.1). By vertically displacing of fluid parcel over a small distance h in the negative direction, the parcel will be surrounded with heavier fluid of density $\rho(z-h)$, and the buoyant force will be stronger than the parcel weight, pushing it upwards. As the parcel fluid rises, it gains momentum and overshoots its original position at z. Eventually, it comes to rest surrounded by lighter fluid at location of $z+h$. At this time, the parcel weight overcomes buoyancy and pushes the parcel downward. As a result, the fluid parcel oscillates with a natural frequency that can be derived as follows.

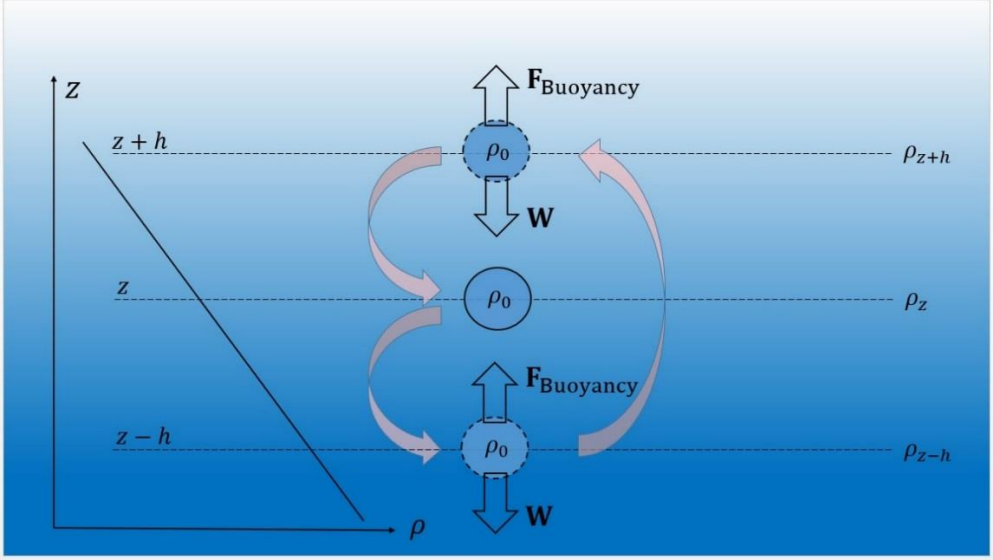

Figure 1.1: Vertical displacement of a fluid parcel inside a stratified environment.

As it is shown in Fig. 1.1, the net forces acting on the fluid volume are weight and buoyancy. From Newton's second law:

$$\rho_z V \frac{d^2h}{dt^2} = \mathbf{F}_{Buoyancy} - \mathbf{W} = (\rho_{z+h} V g - \rho_z V g) \tag{1.1}$$

Assuming that the density differences are very small and ρ_z can be replaced by the reference density ρ_0. Also, on the right hand side of Eq. (1.1), a Taylor series expansion can be used for ρ_{z+h} as $\rho_{z+h} \approx \rho_z + h(\partial\rho/\partial z)$. Dividing both sides of Eq. (1.1) by the parcel volume V, and after a few simplifications, the new equation is:

$$\frac{d^2h}{dt^2} - \left(\frac{g}{\rho_0}\frac{d\rho}{dz}\right)h = \frac{d^2h}{dt^2} + N^2 h = 0 \tag{1.2}$$

Eq. (1.2) represents a differential equation for the oscillation of the parcel with frequency of N. By solving Eq. (1.2) for different values of N^2, various conditions are defined as unstable stratification, neutral stratification and stable stratification:

- *Unstable stratification*: For $N^2 < 0$ since $\partial\rho/\partial z > 0$, Eq. (1.2) has solution as $exp\sqrt{-N^2}t$. Therefore, once the fluid parcel moves from its initial position its displacement grows exponentially and mixing occurs inevitably. This is the unstable stratification and it happens when the top fluid is heavier than the bottom one.
- *Neutral stratification*: For $N^2 = 0$ since $\partial\rho/\partial z = 0$, no oscillation will happen and the fluid parcel remains in the new position.
- *Stable stratification*: For $N^2 > 0$ since $\partial\rho/\partial z < 0$, Eq. (1.2) has periodic solutions as $Sin(Nt)$ and $Cos(Nt)$. Therefore the fluid parcel oscillates around the initial position with frequency N. The oscillation will continue until viscous forces (not considered in the simple system presented in Eq. (1.2)) dampen the oscillation and eventually bring it to rest. This is then a stable stratification and it occurs when lighter fluid sits on top of a heavier one.

The stability of the stratification depends on the buoyancy frequency and this frequency increases with the strength of the density gradient in the vertical direction ($\partial\rho/\partial z$). In the upper layer of the ocean, the buoyancy frequency N is about $10^{-2} rad\, s^{-1}$ (Sutherland, 2005) while in deeper regions is more than ten times smaller. In the atmosphere, in the troposphere (the lowest $11km$ portion of Earth's atmosphere) the buoyancy frequency is in the order of $10^{-2} rad\, s^{-1}$ and in the stratosphere, the layer in top of the troposphere, the buoyancy frequency is up to twice as large. In stably stratified fluids, any perturbation at a frequency less than the Brunt-Vaisala frequency will generate internal waves as explained in this chapter.

1.1.2 Richardson Number

Another key parameter in stratified flow is the Richardson number. Generally, in a fluid with constant density the shear velocity creates a source for instability which results in generation of turbulence. However, in a stably stratified fluid the density gradient provides the opposite effect, stabilizing the fluid flow and resisting mixing by velocity shear. A good example of competition between shear and buoyancy forces is the fundamental problem of the stratified shear layer between two flows moving parallel with different speeds while the upper fluid has smaller density than the lower one. Therefore, in a stably stratified flow, both mechanisms are important and the nature of the balance between these two forces is specified by the gradient Richardson number, Ri_g, defined as:

$$Ri_g = \frac{\text{square of the buouyancy frequency}}{\text{square of the vertical velocity shear}} = \frac{-\left(\frac{g}{\rho_0}\frac{d\rho}{dz}\right)}{\left(\frac{du}{dz}\right)^2} \tag{1.3}$$

where du/dz is the vertical shear velocity. The minus sign in Eq. (1.3) represents the usual density increases with increasing depth. For a finite number of density layers and when the density and velocity are available at least at two levels, an alternative to the gradient Richardson number is the Bulk Richardson number which is defined as:

$$Ri_b = \frac{(\rho_{\text{top}} - \rho_{bottom})}{\rho_0}\frac{g(z_{top} - z_{\text{bottom}})}{(u_{\text{top}} - u_{\text{bottom}})^2} \tag{1.4}$$

Depending on physics of the problem, both gradient and bulk Richardson numbers can be used. Analytical and experimental works related to Kelvin-Helmholtz instability in parallel shear flow (Miles, 1961; Thrope, 1973) show that in a stratified flow the onset of the turbulence depends on the Richardson number, with flows being turbulent for values

lower than a critical value of this parameter. When the Richardson number decreases below its critical value, Kelvin- Helmholtz waves appeared as the flow transitions into a turbulent flow.

1.1.3 Internal Waves

The ocean has a layered density structure with three zones. The upper zone of the three-layered ocean is called surface zone or mixed layer which extends from the surface to a maximum depth of about 500 meters (depending on the seasons and latitude). In this zone, which accounts for about 2% of the ocean water by volume in the world, both temperature and salinity are approximately constant with depth because of mixing by wind and waves. Just below the surface zone there is a region called the pycnocline where density changes rapidly with depth due to extreme environmental changes. Pycnocline refers in general to density, but corresponding nomenclature can be alternatively used to indicate a change due to salinity (halocline) or temperature (thermocline). Generally, the pycnocline covers about 18% of ocean water by volume and extends for depths of 500 to 1000 meters. Finally, the lower dark and cold layer where the water moves very slowly contains about 80% of ocean water by volume and is called the deep layer. This layer is located below the pycnocline and has relatively constant temperature and salinity distributions.

The pycnocline is the only ocean layer which exhibits remarkable changes of density. In this naturally stable stratified environment, perturbations such as wind action or the motion of a body in the fluid can lead to the creation of internal waves. Internal waves can propagate over large distances and transport energy in the ocean and atmosphere. In special circumstances, layering might occur much closer to the surface. In the ocean a light

layer of warm water due to the solar heating or dilution by fresh water due to rain or runoff from shore can occur on top of the saltier, colder bulk of water below.

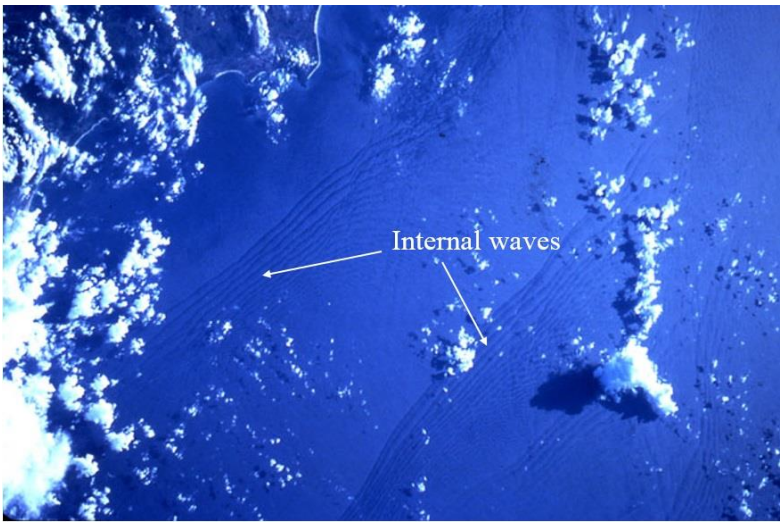

Figure 1.2: Internal waves in the South China Sea (captured by NASA's Shuttle- June 1983).

The motion of ships and submarines in the oceans and seas disturbs the stable stratification equilibrium producing internal waves and anisotropic turbulence. Oceanic internal waves can be seen in images obtained with remote sensing devices from both spacecraft and aircraft, as is the case of synthetic aperture radar (SAR) that can detect surface roughness variations accompanying internal waves; a satellite photo of internal waves in the South China Sea is shown in Fig. 1.2. Submarines often move below the pycnocline region to avoid detection since the pycnocline surface distorts acoustic signals of active sonars and sea vessels. In addition to surface waves, marine vessels can produce internal waves in the saltwater-freshwater boundary in littoral areas. Due to the work done in generating these internal waves, the resistance can be affected considerably in presence of a stratified environment.

It is interesting to note that there are remarkable differences in amplitude, period and phase velocity between surface gravity waves and internal waves. In free surface, the density difference between air and water is large and causes a stronger restoring force. However, the density contrast between layers of water in the same fluid is much smaller which leads to weaker restoring force. As a result, internal waves have longer period, larger amplitude and smaller phase velocity $C_I = \sqrt{(\delta\rho/\rho_0)gh}$, where $(\delta\rho/\rho_0)$ is the specific value of the density change in the ocean with the order of 0.001-0.003.

1.1.4 Dead Water Phenomenon

A surface ship or an underwater vehicle advancing in a stratified environment generates both free surface and internal waves with complex flow structures. In some cases, these internal waves are responsible for a phenomenon known as dead water. The dead-water phenomenon occurs when a surface vessel sailing in stratified seas with a speed close to the celerity of the internal waves, which causes the ship to experience increased resistance and loss of steering power. The internal wave-making resistance is analogous to the free surface wave-making resistance, and it can result in a forces several times higher than those for a vessel sailing in non-stratified waters. To describe this phenomenon the densimetric (or internal) Froude number is defined as:

$$Fr_i = \frac{U_s}{c^*} \tag{1.5}$$

where U_s is the ship velocity and c^* represents the celerity of the longest internal waves, expressed as:

$$c^* = \sqrt{\frac{\Delta\rho}{\rho_0} g L_0} \tag{1.6}$$

where L_0 is the reference depth, ρ_0 is the reference density and $\Delta\rho$ is a reference density difference typically chosen as the density difference from the free surface and a location at depth. The dead water phenomenon is most likely to occur when the densimetric (internal) Froude number is in the order of $Fr_i = O(1)$, causing generation of large internal waves and an increase of power to maintain speed. If this additional power is not available from the ship's power plant then the maximum speed is severely limited. The dead-water phenomenon was reported for the first time by Nansen (1897). In his Arctic Ocean journey to the North Pole during 1893-1896, he observed the loss of steering power and speed experienced by the ship due to generation of internal gravity waves. His report about this phenomena encouraged scientists and engineers to investigate the topic and the problem of advancing ships and submarines in stratified environments, still a problem of importance and rising interest for hydrodynamic phenomena.

1.2 Literature Review on Stratified Flow

There are extensive experimental, numerical and theoretical studies on the problem of stratified flow around objects, aiming at understanding the nature and characteristics of this interesting topic. Different models have been used to simulate stratified flow around canonical geometries such as spheres, cylinders and spheroids. Since the goal of this thesis is the study of stratification for ship hydrodynamics applications without any geometric or theoretical simplifications, a short review of most of studies in stratification, regardless of simplicity of the geometry, can be helpful in understanding the physics of stratified flow. In more relevant studies, research activities were performed to observe the effects of stratification on ship performance. Literature related to the study of moving bodies in a

stably stratified fluid is presented first. Next, experimental or numerical research related to generation of internal waves by passing ships or submarines is presented. Finally, literature discussing the dead-water phenomenon is reviewed in detail.

1.2.1 Moving Body in Stably Stratified Fluid

Experimental investigations on internal wave field generated by a sphere towed in a stratified fluid were presented by Hopfinger *et al*. (1991), Chomaz *et al*. (1991) and Bonneton *et al*. (1993). The authors analyzed the internal waves and the turbulence waves using fluorescent dye technique. The results showed that in stratified flow over sphere, there are four types of waves: lee waves due to the moving sphere; waves due to the wake collapse; waves due to the instabilities in the near-field; and finally random waves due to turbulence. It was observed that the transition from a lee-wave-dominated to a random-wave-dominated regime occurs independently of the Reynolds number at $Fr_i = 4.5$. Also, the amplitude of the lee waves decreased as $1/Fr_i$ while for random waves the amplitude increased with internal Froude number. By introducing a non-dimensional time Nt (where N is the buoyancy frequency and t is the time), Hopfinger *et al*. (1991) studied a subcritical condition with $Re = 3 \times 10^3$ and found that the stratification would be felt by the wakes at $Nt > 2$, the collapse of wakes would occur at $Nt > 14$, and wakes would have two-dimensional features at $Nt > 20$. Also, it was shown that for random waves, the vertical angle of energy propagation and the wavelength would decrease with time according to $(Nt)^{-1}$. Boyer *et al*. (1989) and Lin *et al*. (1992a-1992b) also distinguished two different internal waves. The first type was a lee wave observed in low internal Froude and Reynolds numbers, where the flow was not transitional or turbulent. The second kind was created by

wake collapse in presence of stratification and strong buoyancy force. Moreover, the near-wake turbulence zone grew horizontally for all internal Froude numbers while vertical growth was limited to $Fr_i > 2$. There was a strong dependency of the maximum normalized vertical thickness of the wakes with the internal Froude number, due to the interaction between stratification and turbulence. In another study (Spedding *et al*., 1996), the growth rate of wake width in both stratified and non-stratified cases was compared, observing that the normalized wake width growth rate increased at approximately the same rate as in homogeneous fluid flow, but with decreasing internal Froude number it became narrower, not wider, showing the importance of stratification. Also, the centerline defect velocity reached values one order of magnitude larger than those measured for three-dimensional wakes of homogeneous flow at equivalent downstream locations. A maximum Reynolds number $Re = 2 \times 10^4$ was attained, at which point collapse of wake width and enstrophy ensued. Vortical interactions were also present, usually between co-rotating vortices. During this interaction and merging process, the vortices initially had no vertically axial symmetry, but after the interaction the resulting vortices exhibited axial symmetry without further interactions downstream. Lofquist and Purtell (1984) conducted an experiment to measure the difference of stratified and non-stratified drag coefficient $\Delta C_D(Re, \kappa)$, with $Re = 2Ua/\nu$ and stratification parameter $\kappa = Na/U$, with U and a the velocity and radius of the sphere, respectively, and N the Brunt-Vaisala frequency. The authors found that the drag force on the sphere could decrease or increase as a result of stratification effects. For different values of $\Delta\rho/\rho_0$, shadowgraph and dye visualization techniques were used to observe the evolution of the stratified wake. It was shown that ΔC_D was insensitive to Re for the range of Reynolds numbers used, 150 to 5000. For $Re = 200$ and internal Froude number range from 0.25 to

200, Hanazaki (1988) used finite differences simulations to solve the flow past a sphere of a non-diffusive stratified fluid using the Boussinesq approximation. The drag coefficient was determined from the pressure distribution and velocities around the sphere. Both drag force and lee wave behavior outside the boundary layer depended on the internal Froude number, and the Reynolds number only affected the location of the separation line on the sphere which resulted in changes in the drag coefficient. Also, the amplitude and the wavelength of the internal waves were computed to obtain the relation between internal waves and separation process on the sphere and compared with previous experimental and theoretical results. To study the effect of the Prandtl number on a turbulent stratified wake, de Stadler *et al*. (2010) used direct numerical simulation (DNS) to solve the flow field of a towed sphere in a stratified fluid. For a Reynolds number of 10,000 and a range of Prandtl numbers, it was observed that vorticity and mean quantities such as defect velocity and wake dimension were weakly affected by the Prandtl number. However parameters such as wave flux, the transfer of energy between potential and kinetic modes, total energy of the wake and mixing efficiency were strongly affected by the Prandtl number.

A number of experimental and numerical studies on the wake of self-propelled objects in stratified flow have been reported in the literature. Schooley and Stewart (1963) conducted an experimental study for a self-propelled submerged body moving in both homogeneous and stably stratified fluids. The horizontal and vertical average wave widths were compared in these two flows and it was observed that there were differences in the turbulent wakes between stratified and non-stratified cases. In the case of homogenous fluid the turbulent flow behind the moving object and its acting propeller had a continually irregular conical shape, while for the stratified environment there was a vertical collapse

along with horizontally spreading of the turbulent wake due to the action of restoring buoyant forces which resulted in internal waves. Meunier and Spedding (2006) presented further experimental work to investigate the wake of a bluff body in three configurations: momentum-excess, momentumless, and momentumless with a slight angle of attack, finding that the coherent structures in the wake were different in all these three cases. The momentum wake displayed two layers of counter-rotating vorticity, with an evident coherent pattern. The momentumless case, however, had the same counter-rotating layers of vorticity but no coherent pattern evident. A series of experimental tests on self-propelled wakes were conducted by Lin and Pao (1973, 1974a, 1974b) and Lin *et al*. (1976), along with a comprehensive review on wakes generated by moving bodies in stratified fluids from Lin and Pao (1979). The results showed that the wake started to meander around a mean position for $4.5 < Nt < 9$. Beyond $Nt \approx 9$, a quasi two-dimensional staggered 'pancake street' of coherent vortices was identifiable. Brucker and Sarkar (2010) used direct numerical simulation (DNS) to compare towed sphere and self-propelled spheroid wakes at $Re = 50{,}000$. The authors compared the mean velocity in both cases and observed that in the self-propelled case, due to the higher shear, the mean velocity decayed more rapidly than for the towed case, resulting in a faster rate of energy transfer to the turbulence field. Also, by comparing the vertical wake thickness in both cases, it was observed that the self-propelled wakes were thicker than those for the towed case. The presence of buoyancy resulted in a mean-to-turbulence energy transfer in the vertical direction, allowing the wake to survive longer, and in the case of self-propelled body it decoupled the regions of negative and positive momentum in the vertical direction. Using the same simulations, de Stadler and Sarkar (2012) studied the turbulent wake behind an accelerating self-propelled

axisymmetric body in a stratified environment. To create the acceleration for studying the effects of excess momentum on the initially momentumless self-propelled wake, a velocity profile corresponding to the net thrust was added to the self-propelled velocity which resulted in small and moderate excess momentums. The study showed that parameters such as wake width, mean kinetic energy and defect velocity depended on the amount and shape of this excess momentum. Also, the turbulent kinetic energy and the dissipation rate increased as the shear in the mean profile increased.

1.2.2 Ships and Submarines in Stratified Flows

The generation of internal waves by passing ships or submarines has been investigated experimentally and numerically. "Two-layer" models, in which fluids with different density are separated by an interface (the pycnocline), are simplest and have received particular attention. Hudimac (1961) used the two-layer model to simulate the stratification problem with an infinitely deep lower layer. Both surface and internal waves were computed, showing that the internal waves had the same pattern as the Kelvin free surface waves. Also, the pattern of the internal waves strongly depended on the speed of the source, with divergent and transverse waves for subcritical cases and only divergent waves for supercritical speeds. Crapper (1967) used a simple analytical method to solve the two-layer model and found that stratification hardly changed the free surface waves, however, the density gradient and upper layer depth strongly affected the pattern and amplitude of the internal waves. Internal waves induced by a moving ship in a shallow thermocline were studied by Tulin and Miloh (1991). A semi-submerged spheroid was used as ship hull and a nonlinear hyperbolic PDE was solved numerically to obtain the near-field flow

disturbances around the ship body. The authors showed that there was similarity between ship-induced narrow V-shape wakes on the free surface and the internal wave patterns. The internal waves strongly depended on the ship hull geometry, the densimetric Froude number and the thermocline conditions. Ma and Tulin (1993) conducted experiments to study the internal waves created by the passing of a ship modeled as a half spheroid. A shallow layer of freshwater on top a deeper layer of salty water with a total density difference ranging from 0.2 to 0.6 percent was used. The internal wave fields were measured for supercritical densimetric Froude numbers, $Fr_i > 1$, and compared with the theoretical results by Tulin and Miloh (1991). Nicolaou *et al*. (1995) studied an impulsively accelerating source in a thermocline using ray theory (Stevenson, 1973; Woodhead, 1983) with focus on unsteady waves, analyzing both oblique and transverse internal waves. It was observed that low speeds created transverse waves with longer wavelength and they could be decomposed as a sum of baroclinic modes with permanent presence of the lowest mode. Also, a finite difference simulation was used to validate the analytical results of the wave patterns. For a large density difference and large speed of ship compared to internal wave velocity, Yeung and Nguyen (1999) investigated the case of the stratification with finite depth. A detailed study of both internal and surface modes were considered, concluding that when the ship velocity was slow both surface and internal waves had the same divergence as a Kelvin pattern, $\theta = 19.28^{\circ}$. When the velocity was further increased the angle of ship wave started to decrease, but the pattern of the ship waves then consisted only of the divergent waves. Radko (2001) compared the amplitudes of the various systems of internal and surface with *n*-density layers and showed that the results for two-layer fluids by Yeung and Nguyen (1999) could be extended to the models with more layers of stratification. Vasseur *et al*.

(2008) provided two videos to show the motion of a boat on two-layer and three-layer fluids and observed large amplitude interfacial waves and not much change in surface waves. Chen *et al*. (2007) conducted an experimental study to explore wave mechanism and evolution in stratified flow. Their experiment included a two-layer fluid system of fresh and brine water inside a channel. In that work the authors presented a statistical model for the internal waves and obtained suitable regression models.

1.2.3 Dead-Water

The "Dead-Water" phenomenon was reported for the first time by Nansen (1897) in his arctic journey to the North Pole during 1893-1896. From that time to present, the generation of internal waves in a stratified ocean has been investigated in many experimental and numerical works to describe this phenomenon. The internal waves are created as the motion at the interface of two-layer fluid with different densities (pycnocline zone) in the oceans. To see the effect of stratification on ship motion, Ekman (1904) conducted an experimental study as his PhD thesis, by towing a ship model through a stratified fluid inside a glass-sided tank. He concluded that a ship moving in stratified environment experienced a powerful drag due to the internal waves, and this drag force got larger when the ship speed reached to the maximum wave celerity of the interfacial waves. Mercier *et al*. (2011) provided a detailed study related to Ekman's work by setting up a new experiment and for different stratification cases including two-layer, three layer and linearly stratified flows with different densimetric Froude numbers (see Fig. 1.3). This work included remarkable information about ship behavior in stratified flow since most of

previous works were related to only two-layer fluid condition while this experiment analyzed the three-layer and linear stratified flows as more realistic stratification condition.

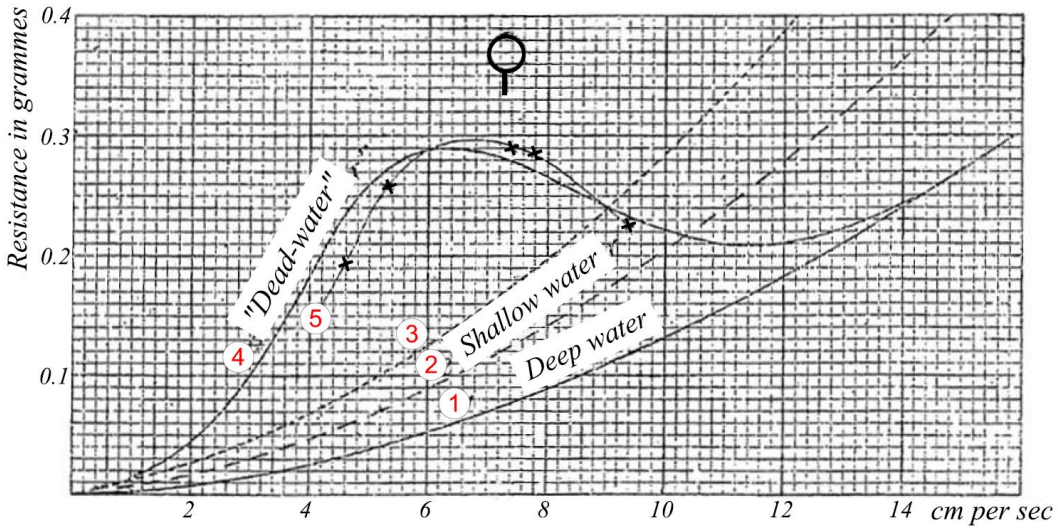

Figure 1.3: The variation of Resistance to Ship speed at different conditions (Figure from Mercier *et al*., 2011). This figure is a result from Ekman (1904) which compares the non-stratified deep and shallow cases with stratified case of a boat towed in a two-layer fluid with 3% density difference in dead water phenomenon.

According to this work, the same unsteady behavior associated with dead-water was observed in both two-layer and three layer fluid, and in a case of lineally stratified flow several waves were generated when the ship evolved in it with propagation of an infinite number of modes. Miloh *et al*. (1993) used a linear theory to simulate the dead water phenomenon in a two-layer fluid with finite depth. The ship was simulated by half of prolate spheroid as a slender body moving steadily on the free-surface of a surface layer of light fluid resting upon heavy fluid. Using Green's function method, they presented the wave resistance, the interface and free surface disturbances and found a sudden rise of internal-wave resistance at subcritical speed with densimetric Froude number about 0.9 caused by the dead-water phenomenon encountered by slow ship moving in stratified flow. An

experimental study to explore wave mechanism and evolution in stratified flow was conducted by Chen *et al*. (2007). Their experiment included a two-layer fluid system of fresh and brine water inside channel and in that work the authors presented a statistical model for the internal waves and obtained suitable regression models. The dead water resistance and internal wave of a ship moving at subcritical speed along the upper layer of a two-layer fluid were studied through a three-dimensional theoretical-numerical model by Grue (2015). For different ship draught, b_0, varying from 0.25 to 0.9 of the upper layer depth, h_0, and for densimetric Froude number in the range close to critical speed with $Fr \approx 0.875 - 1.125$, the author calculated dead water resistance function as $C_{dw}/(b_0/h_0)^2$, and it was observed that the regardless of the ship draught the dead water resistance only depended on the densimetric Froude number. Also, it was shown that this function reached a maximum value at subcritical Froude number depending on the ship draught. Finally, good agreement was obtained by comparing the three-dimensional wave patterns at critical speed with experimental results.

1.3 Objectives and Approach

As the ship evolves through a stable stratified background it disturbs the flow and creates internal waves that propagate downstream. While the effect of stratification on resistance and propulsion can be strong for extreme conditions, as in the case of dead-water, the main focus of the study of stratification is in wakes and signature effects. There is a considerable difference in scales between the near-field flow, which is restricted to the region around the vessel, to the far-field where the internal waves are only important. The near-field flow is produced by the direct interaction of the stably stratified flow in the ocean

with the advancing vessel and all its parts including the hull, propeller, control surfaces and rudders. These interactions between vessel and its surroundings are responsible for the formation of some interesting flow features. Therefore, the methodology to predict the near-field density stratified flows of ships and submarines is of prime interest in ship hydrodynamics and can be helpful for ship and submarine engineers.

In general, laboratory experiments have been used as first and most reliable procedure to study many different cases of stratified flow. Moreover, they have been used to benchmark analytical and numerical results. However, certain features of these flows, cannot be captured, due to scale and measurement limitations in these models. Consequently, numerical simulations can be carried out to further investigate the details of stratified flows over bodies. Computational fluid dynamics (CFD) is widely seen as a key technology in this respect. CFD denotes techniques solving fluid dynamics equations numerically, usually involving significant computational effort. Numerous models can be used to solve the stably stratified flow from simple theoretical models to expensive direct numerical simulation (DNS). However, these models can only be used for simple cases such as channel flow or flow around simple obstacles, and using these models to simulate flow around the complex geometry of a ship or submarine is computationally prohibitive. Therefore, as a challenge of this thesis, RANS and hybrid RANS/LES models commonly based on turbulent kinetic energy (TKE) closure schemes are modified and used to simulate the flow around advancing vehicle inside the stable stratified flow. This thesis further develops the naval hydrodynamics code REX, an overset, block-structured flow solver designed for ship applications, to handle density transport. Stratification is added by lumping together the two main sources of density change: thermal and salinity stratification

thereby transporting the density directly, instead of either temperature or salinity, and this density is directly used in liquid phase momentum equations. This approach uses a density transport equation and modifications to the mass and momentum conservation equations and turbulence model equations to include appropriate effects due to changes in density. Boundary and initial conditions are also modified to impose a background density distribution. Finally, by solving the near-field density stratified flows of ships and submarines, the dead-water phenomenon is simulated for surface ship by predicting the internal wave resistance and patterns at different conditions of stalely stratified background.

1.4 Thesis Structure

The body of this thesis consists of six chapters, in which different aspects of stratification in ship hydrodynamics are studied. These chapters can be read separately. Chapter 2 includes the mathematical models and numerical methods in REX code in detail. In Chapter 3, the implementation of the numerical model and other modifications into the governing equations are discussed. As a result, the new version of REX can simulate the stratified flow in ship hydrodynamic application regardless of any simplifications such as geometric simplification (using sphere or even point source instead of real submerged bodies) and theoretical simplification (ignoring the effect of viscosity). This new version of REX is used for validation of two separate cases including a two-dimensional square cavity (Al-Amiri *et al*., 2007) and three-dimensional stratified flows past a sphere (Bonneton *et al*., 1993). In the case of the sphere, the object is towed in a stable stratified flow and the structures of the wakes and flow were studied in details. In Chapter 4, we address the problem of the three-dimensional structure of the stratified flow around research vessel

(R/V) Athena and the notional submarine Joubert BB2 operating near the surface in a stably stratified fluid. The computations are performed for a relatively strong stratification condition measured at the Kitimat Bay Station, BC, in the case of R/V Athena, and for two-layer hyperbolic tangent profiles for Joubert. This chapter is self-contained and divided into subsections with problem statement, solution strategy, and simulation design along with results and discussion, and conclusions. The problem of dead water is presented in Chapter 5. The bare hull R/V Athena is towed in a two-layer stratified flow, and for both stratified and homogeneous flows the resistance force is compared to show the effect of dead water phenomenon on ship performance. Finally, Chapter 6 summarizes conclusions and recommendations for future work.

CHAPTER 2 COMPUTATIONAL METHODS

2.1 Introduction

The computational naval hydrodynamics code REX is used in this thesis. REX is an overset, block-structured CFD solver designed for ship applications using either absolute or relative inertial non-orthogonal curvilinear coordinate system for arbitrary moving but non-deforming control volumes (Carrica *et al*., 2007a). The code includes high order finite difference schemes with conservative formulations, parallelization based on a domain decomposition approach using the message-passing interface (MPI), and captive, semi-captive, and full 6DOF capabilities for multi-objects with parent/child hierarchy (Carrica *et al*., 2007b). Turbulence models include blended $k-\varepsilon/k-\omega$-based isotropic and anisotropic RANS, DES and DDES approaches with near-wall or wall functions for full scale simulations. A single-phase level-set method is used for free-surface capturing. By separating the water flow field and air flow field, the water field is decoupled from the air solution and then the air field uses the unsteady water field as immersed boundary condition, solving air/water problems in a semi-coupled fashion (Huang *et al*., 2008). Propulsion can be simulated with a simple axisymmetric body force model, with a more complex coupling with the potential flow code PUF-14 (Chase *et al*., 2013; Martin *et al*., 2015) or with direct simulation of the rotating propeller/impeller. Feedback controllers (linear and non-linear PID) are available to control a variety of processes, including speed (used for instance to find the self-propulsion condition or in an autopilot), heading, roll, pitch and depth controllers. Numerical methods include advanced iterative solvers, higher order finite differences with conservative formulation, projection method for pressure-velocity coupling

and PETSc for solving pressure Poisson equation. Dynamic overset grids use Suggar (Noack, 2005) or Suggar++ (Noack *et al*., 2009) to compute the domain connectivity. REX also has unique capabilities with a new pressure-velocity coupling approach that improves enforcement of the continuity and enables high void fraction or air/water computations (Li *et al*., 2015a) to simulate polydisperse bubbly flows (Castro and Carrica, 2013). Moreover, the code includes a quaternion-based multibody dynamics (MBD) approach to solve bodies and cables simultaneously and coupling with the MBD code Virtual lab (Li *et al*., 2015b) and a universe/system/planet overset decomposition technique to run large-scale motion problems.

2.2 Mathematical Modeling

2.2.1 Governing Equations

In this section, the mathematical modeling used in CFD code REX is summarized briefly. The equations are non-dimensionalized using reference speed, U_0, length, L_0, and fluid properties such as density and viscosity. The mass and momentum equations are written as:

$$\frac{\partial u_i}{\partial x_i} = 0 \tag{2.1}$$

$$\frac{\partial u_i}{\partial t} + \frac{\partial u_i u_j}{\partial x_j} = -\frac{\partial p}{\partial x_i} + \frac{\partial}{\partial x_j}\left[\frac{1}{Re_{eff}}\left(\frac{\partial u_i}{\partial x_j} + \frac{\partial u_j}{\partial x_i}\right)\right] + S_i \tag{2.2}$$

where u is the velocity in inertial earth-fixed coordinates (X, Y, Z), $Re_{eff} = U_0 L_0/(\nu+\nu_t)$ is the effective Reynolds number and S_i is the body force source term. The non-dimensionless piezometric pressure is defined as:

$$p = \frac{p_{abs}}{\rho_0 {U_0}^2} + \frac{z}{Fr^2} + \frac{2}{3}k \tag{2.3}$$

where $Fr = U_0/\sqrt{gL_0}$ is the Froude number, p_{abs} is the absolute pressure and $k = 1/2(\overline{u'^2} + \overline{v'^2} + \overline{w'^2})$ is the turbulent kinetic energy, with u', v', and w' the velocity fluctuations.

2.2.2 Level-Set Free Surface Model

REX uses a single-phase level-set method to capture the interface between two immiscible fluids defined as the zero level-set of a signed distance to the interface. The single level-set method is used for the flow field in the denser field only (water for ship hydrodynamic applications). In this method, the surface tension effects on free surface, and also the viscosity and density of the air are considered negligible. Based on this assumption, the level-set function, ϕ, is defined in the whole domain and the its sign is arbitrarily set to positive in water and negative in air and the iso-surface $\phi = 0$ shows the free surface between water and air. The equation for the level-set function without mass transfer on the free surface can be written as (Carrica *et al*., 2007a):

$$\frac{\partial \phi}{\partial t} + u_j \frac{\partial \phi}{\partial x_j} = 0 \tag{2.4}$$

Eq. (2.4) satisfies the kinematic free surface boundary conditions automatically. The dynamic boundary conditions at the water-air interface need to be explicitly imposed. The pressure is assumed constant on the air side and the effect of the turbulent kinetic energy on the free surface is neglected which leads to the dimensionless piezometric pressure at the interface. Therefore, the boundary condition for pressure on the free surface is:

$$p_{int} = \frac{z_{int}}{Fr^2} \tag{2.5}$$

Neglecting friction on the air, the jump condition in the tangential direction reduces to (Carrica *et al*., 2007a):

$$\mathbf{N}.\nabla\mathbf{u}|_{\text{Interface}} = 0 \tag{2.6}$$

where $\mathbf{N} = -\nabla\phi/|\nabla\phi|$ is the unit normal vector from the free surface into air. By enforcing Eq. (2.5) on the interface and solving Eq. (2.6) in air along with Eqs. (2.1)-(2.2) in water, the free surface boundary conditions are enforced.

The air/water interface does not lay necessarily on a grid point, requiring an artificial pressure on neighboring grid points in the air side so that the free surface pressure satisfies Eq. (2.5) at the location of the interface. Using a linear interpolation, the pressure condition on the neighbor point is obtained as:

$$p_a = \frac{p_{int}}{\eta} - p_w \frac{1-\eta}{\eta} \tag{2.7}$$

where p_a is the pressure of any neighbor in air side, p_w is the pressure in water side and $\eta = \phi_p/(\phi_p - \phi_{na})$ is the distance fraction from the local point to the interface. Also, it is critical for single-phase level-set to keep ϕ as a distance function throughout whole computation. So, the level-set function is reinitialized periodically by solving:

$$\mathbf{N}.\nabla\phi = sign(\phi_0) \tag{2.8}$$

where ϕ_0 is the level set function prior to reinitializing. Eq. (2.8) is nonlinear since $\mathbf{N}$ is a function of ϕ and thus requires nonlinear iterations. Details of the level set method used, including reinitialization techniques are described in Carrica *et al*. (2007a).

2.2.3 Turbulence Modeling

Menter's blended $k-\varepsilon/k-\omega$ turbulence model (Menter, 1994) is used. In this model the $k-\omega$ model (Wilcox, 1988) is used near walls while the $k-\varepsilon$ model is used elsewhere. The turbulent kinetic energy, k, and the specific dissipation rate, ω, are computed as

$$\frac{\partial k}{\partial t}+\left(u_j-\sigma_k\frac{\partial v_t}{\partial x_j}\right)\frac{\partial k}{\partial x_j}-\frac{1}{Pe_k}\frac{\partial^2 k}{\partial x_j^2}+S_k=0 \tag{2.9}$$

$$\frac{\partial \omega}{\partial t}+\left(u_j-\sigma_\omega\frac{\partial v_t}{\partial x_j}\right)\frac{\partial \omega}{\partial x_j}-\frac{1}{Pe_\omega}\frac{\partial^2 \omega}{\partial x_j^2}+S_\omega=0 \tag{2.10}$$

where the turbulence viscosity, ν_t, and sources for k and ω are defined as:

$$\nu_t=\frac{k}{\omega} \tag{2.11}$$

$$s_k=G-\beta^*\omega k=G-D_{RANS}^k \tag{2.12}$$

$$s_\omega=\gamma\frac{\omega}{k}G-\beta^*\omega^2+2(1-F_1)\sigma_{\omega 2}\frac{1}{\omega}\nabla k.\nabla\omega \tag{2.13}$$

$$G=\nu_t\boldsymbol{\tau}:\nabla\mathbf{v} \tag{2.14}$$

where F_1 is the blending function, that switches between the $k-\omega$ model near the wall to the $k-\varepsilon$ model on the free-stream region and it is defined as

$$F_1=tanh\left[\left(min\left(max\left(\frac{\sqrt{k}}{0.09\omega\delta};\frac{1}{Re}\frac{500}{\delta^2\omega}\right);\frac{4\sigma_{\omega 2}k}{CD_{k\omega}\delta^2}\right)\right)^4\right] \tag{2.15}$$

$$CD_{k\omega}=max\left(2\sigma_{\omega 2}\frac{1}{\omega}\left(\frac{\partial k}{\partial x_j}\right)\left(\frac{\partial \omega}{\partial x_j}\right);10^{-20}\right) \tag{2.16}$$

where $\gamma=\frac{\beta}{\beta^*}-\sigma_\omega\kappa/\sqrt{\beta^*}$, $\sigma_{\omega 2}=0.856$, $\beta^*=0.09$ and $\kappa=0.41$. δ is the distance to the nearest no-slip surface. The Peclet numbers are also defined as

$$Pe_k = \frac{U_0 L_0}{\nu + \sigma_k \nu_t} = \frac{1}{1/Re + \sigma_k \nu_t} \tag{2.17}$$

$$Pe_\omega = \frac{U_0 L_0}{\nu + \sigma_\omega \nu_t} = \frac{1}{1/Re + \sigma_\omega \nu_t} \tag{2.18}$$

The constants of the model are defined as

$$\psi = F_1 \psi_1 + (1 - F_1)\psi_2 \tag{2.19}$$

and these constant are presented in Table (2.1).

Table 2.1: The constant parameters in blended $k - \varepsilon/k - \omega$ and SST models.

ψ	ψ_1	ψ_2	$\psi_{1,SST}$
γ	0.0553	0.04403	0.0553
σ_ω	0.5	0.856	0.5
σ_k	0.5	1.0	0.85
β^*	0.09	0.09	0.09
β	0.075	0.0828	0.075

The SST version of the model (Menter, 1994) accounts for transport of the principal turbulent stresses, with improved results for flows with adverse pressure gradients. The differences between the SST model and the standard model are the value of σ_k and the definition of eddy viscosity:

$$\nu_t = \frac{0.31k}{max(0.31\omega, \Omega F_2)} \tag{2.20}$$

$$F_2 = tanh\left[\left(max\left(\frac{2\sqrt{k}}{0.09\omega\delta}; \frac{500}{\delta^2\omega}\right)\right)^4\right] \tag{2.21}$$

where Ω is the absolute value of the vorticity. The reader is referred to Carrica *et al*. (2007a) for details on the model. At the free surface, it is customary to use zero normal gradient for both k and ω, which translates in the following conditions:

$$\nabla k.\mathbf{N} = \nabla \omega.\mathbf{N} = 0 \tag{2.22}$$

Equations (2.6) and (2.22) are solved in air to transport the velocity, k and ω from the interface into the air. This is called a normal extension and naturally enforces the zero normal gradient of these quantities. The $k-\varepsilon/k-\omega$ model is extended to detached eddy simulation (DES) and delay detached eddy simulation (DDES). The dissipative term of the k-transport equation is modified as (Travin *et al*., 2002; Xing *et al*., 2010):

$$D_{RANS}^{k} = \beta^{*}\omega k = \frac{k^{3/2}}{l_{k-\omega}} \tag{2.23}$$

$$D_{DES}^{k} = \frac{k^{3/2}}{l_{DES}} \tag{2.24}$$

$$D_{DDES}^{k} = \frac{k^{3/2}}{l_{DDES}} \tag{2.25}$$

where the length scale for RANS, DES and DDES are:

$$l_{k-\omega} = \frac{k^{1/2}}{\beta^{*}\omega} \tag{2.26}$$

$$l_{DES} = \min(l_{k-\omega}, C_{DES}\Delta) \tag{2.27}$$

$$l_{DSES} = l_{k-\omega} - f_{DDES} \times \max(0, l_{k-\omega} - C_{DES}\Delta) \tag{2.28}$$

with Δ as the mesh scale, $C_{DES} = 0.65$ as the DES constant, adopted from typical homogeneous turbulence problems, and f_{DDES} as a modified blending function.

2.2.4 Propeller Modeling

Two propeller approaches are available in REX. A simplified model (Stern *et al*., 1998) is utilized to prescribe axisymmetric body force with tangential and axial components, and the radial distribution of forces is based on the Hough and Ordway

circulation distribution with zero loading at the tip and root. In the case of real discretized propeller, propeller is gridded and rotates according to an imposed rotational speed or controlled by a controller. The discretized propeller naturally provides all forces and moments from hub and blades, including thrust. These forces and moments are used by the motions solver to predict motions.

2.2.5 Controller Modeling

REX uses a proportional-integral-derivative controller (PID controller) modeling as a generic control loop feedback mechanism to impose a variety of conditions in propeller rotational speed, heading control, autopilot, speed control and turning and zig-zag maneuvers. The general form of PID controller equation is:

$$\delta(t) = Pe + I\int_0^t edt + D\frac{de}{dt} \tag{2.29}$$

which includes three separate terms. In Eq. (2.29), the first term represents the proportional response which makes a change to the output that is proportional to the current error value. As it is shown in Eq. (2.29), this term is obtained by multiplying the proportional gain, P, by the error, $e = A_t - A_c(t)$. The error represents the difference between desired value, A_t, and the current value, $A_c(t)$. The second term in Eq. (2.29) represents the integral term which is proportional to both the duration of the error and the magnitude of the error. A constant integral gain, I, is multiplied by the accumulated error is added to the controller output. By adding the integral term into the proportional term, the process of controlling and reaching into the set-point will be accelerated. But, sometimes it could cause overshooting since this integral term is responding to accumulated errors from the past. Finally, the third term in Eq. (2.29) represents the derivative term which is responsible for

determining the reaction to the rate at which the error has been changing. In this term, the rate of change of the process error will be calculated by finding the slope of the error over time and it is multiplied by the derivative gain, D. By adding this term into the PID controller equation, the magnitude of the overshoot produced by the integral term will be reduced, but this term is sometimes sensitive to noise in the error term, and may cause the process to become unstable.

2.2.6 Ship Motion Equations and 6DOF Module

To simulate the moving object in a fluid, REX uses six nonlinear coupled equations as the 6DOF rigid body equations of motion representing the translational and rotational motions of the object. The solution of the fluid flow equations is performed in an earth-based inertial reference frame. The continuity and momentum equations (2.1) and (2.2) are strongly coupled with the rigid body equations of motions to solve 6DOF equations of ship motion. In REX, the 6DOF equations of motions are solved in non-inertial ship fixed coordinate while the flow field is solved in inertial earth-fixed coordinates. For the simulation of moving propellers and rudders, a hierarchy of objects is used in the way that the children objects such as the rudders or propeller inherit the motions from the parent which is usually the ship or submarine and add its own motion respect to the parent object.

To compute the force, piezometric pressure, friction and hydrostatic pressure force are integrated on the earth system separately on children and parent objects as:

$$F_p = \int p dA \tag{2.30}$$

$$F_f = \int \frac{1}{2Re}(\nabla U + \nabla U^T) dA \tag{2.31}$$

$$F_b = \int \frac{z}{Fr^2} dA \tag{2.32}$$

where F_p is the dynamic pressure force, F_f is friction force and F_b is the hydrostatic pressure force, and A is the outward pointing area vector. After integrating over the wetted surface area, the total force, F_T, is calculated by summation of Eqs. (2.30)-(2.32) and this total force in absolute inertial earth-fixed coordinate system is projected into the non-inertial ship-fixed coordinate system using Euler angle rotation matrix, J_1, as:

$$F_B = J_1 F_T \tag{2.33}$$

The Euler angle rotation matrix, J_1, is defined as:

$$J_1 = \begin{bmatrix} cos\psi cos\theta & -sin\psi cos\varphi + cos\psi sin\theta sin\varphi & sin\psi sin\varphi + cos\psi sin\theta cos\varphi \\ sin\psi cos\theta & cos\psi + sin\psi sin\theta sin\varphi & -cos\psi sin\varphi + sin\psi sin\theta cos\varphi \\ -sin\theta & sin\theta sin\varphi & cos\theta cos\varphi \end{bmatrix} \tag{2.34}$$

where ψ, θ and φ are the roll, pitch and yaw angles, respectively. The same process is used to calculate the moment value by integrating the elemental forces by friction and pressure with the distance to the center of gravity, r_{CG}, as:

$$M_T = \int r_{CG} \times \left[\left(\frac{1}{2Re}(\nabla U + \nabla U^T) - \left(z - \frac{z}{Fr^2}\right)\mathbf{I}\right).dA\right] \tag{2.35}$$

$$M_B = J_1 M_T \tag{2.36}$$

After finding forces and moments in the non-inertial ship-fixed coordinate system, the equations of motion for the can be written as:

$$m\{\dot{u}_t - v_t r_t + w_t q_t - x_G(q_t^2 + r_t^2) + y_G(p_t q_t - \dot{r}_t) + z_G(p_t r_t + \dot{q}_t)\} = X \tag{2.37-a}$$

$$m\{\dot{v}_t - w_t p_t + u_t r_t - y_G(r_t^2 + p_t^2) + z_G(q_t r_t - \dot{p}_t) + x_G(q_t p_t + \dot{r}_t)\} = Y \tag{2.37-b}$$

$$m\{\dot{w}_t - u_t q_t + v_t p_t - z_G(p_t^2 + q_t^2) + x_G(r_t p_t - \dot{q}_t) + q_G(r_t q_t + \dot{p}_t)\} = Z \tag{2.37-c}$$

$$I_x \dot{p}_t + (I_z - I_y)\dot{q}_t \dot{r}_t + m[y_G(\dot{w}_t - u_t q_t + v_t p_t) - z_G(\dot{v}_t - w_t p_t + u_t r_t)] = K \tag{2.37-d}$$

$$I_y\dot{q}_t + (I_x - I_z)\dot{r}_t\dot{p}_t + m[z_G(\dot{u}_t - v_t r_t + w_t q_t) - x_G(\dot{w}_t - u_t q_t + v_t p_t)] = M \qquad (2.37\text{-e})$$

$$I_z\dot{r}_t + (I_y - I_x)\dot{p}_t\dot{q}_t + m[x_G(\dot{v}_t - w_t p_t + u_t r_t) - y_G(\dot{u}_t - v_t r_t + w_t q_t)] = N \qquad (2.37\text{-f})$$

where the LHS terms include linear, angular, Coriolis, and centripetal accelerations and the RHS are applied forces and moments. In these equations, m is mass, (X, Y, Z) are surge, sway, and heave forces, (K, M, N) are the roll, pitch, and yaw moments, (u_t, v_t, w_t) are linear velocities, $(\dot{u}_t, \dot{v}_t, \dot{w}_t)$ are angular accelerations, (x_G, y_G, z_G) are coordinates of center of gravity, $(p_t, q_t, r_t) = (\dot{\psi}_t, \dot{\theta}_t, \dot{\phi}_t)$ are angular velocities, $(\dot{p}_t, \dot{q}_t, \dot{r}_t)$ are angular accelerations, and (I_x, I_y, I_z) are moment of inertia of the ship (see Fig. 2.1). To solve Eq. (2.37), both explicit and implicit methods with a predictor- corrector approach are used for solving these equations of motions (Carrica *et al*., 2007b).

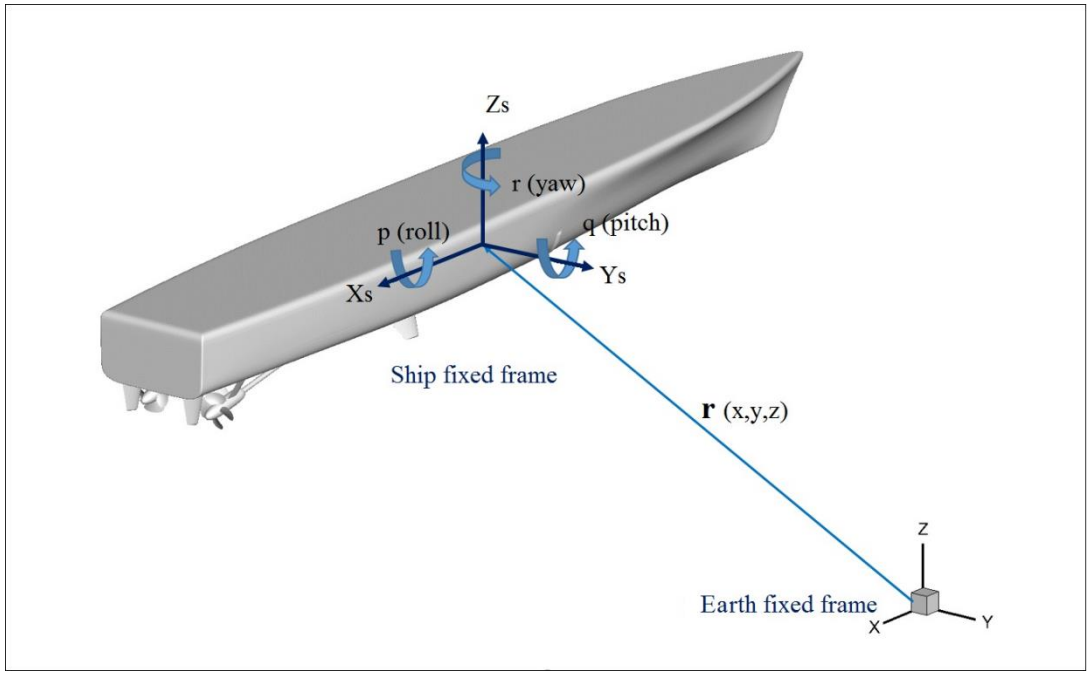

Figure 2.1: The Earth and ship fixed reference systems.

2.2.7 Dynamic Overset Grid

In any numerical simulation, the grid generation would be the most important concern and creating a grid system with the best quality is of great importance. Complex geometry is hard or impossible to generate with a single grid. Therefore, the overset methodology could be helpful in simplifying the grid generation for complex geometries since it uses different blocks for different parts of it, and it is especially helpful in cases when the computational domain is composed of static and moving grids with application in aerospace and ship hydrodynamics. In fact, overset grids are used to enable large relative motions between grid components and simplify the grid generation process. Overset blocks can be added in regions where refinement is needed, to add appendages, and providing great flexibility to the simulation of complex geometries (Noack *et al*., 2009). Figure 2.2 shows an example of grid system of fully appended R/V Athena as a body fitted blocks around the moving ship hull inside a static background grid. This grid system includes many blocks as ship hull, refinement and background grids. In a grid system, all grids need to be classified as moving or static regarding their ability to move, in order to compute the grid connectivity at run time when the grid blocks experience relative motion during the simulation. For instance, in Fig. 2.2, the background grid is considered as a static grid fixed to the earth system and it does not move at all, and the free surface and the outer boundary conditions are defined in this grid.

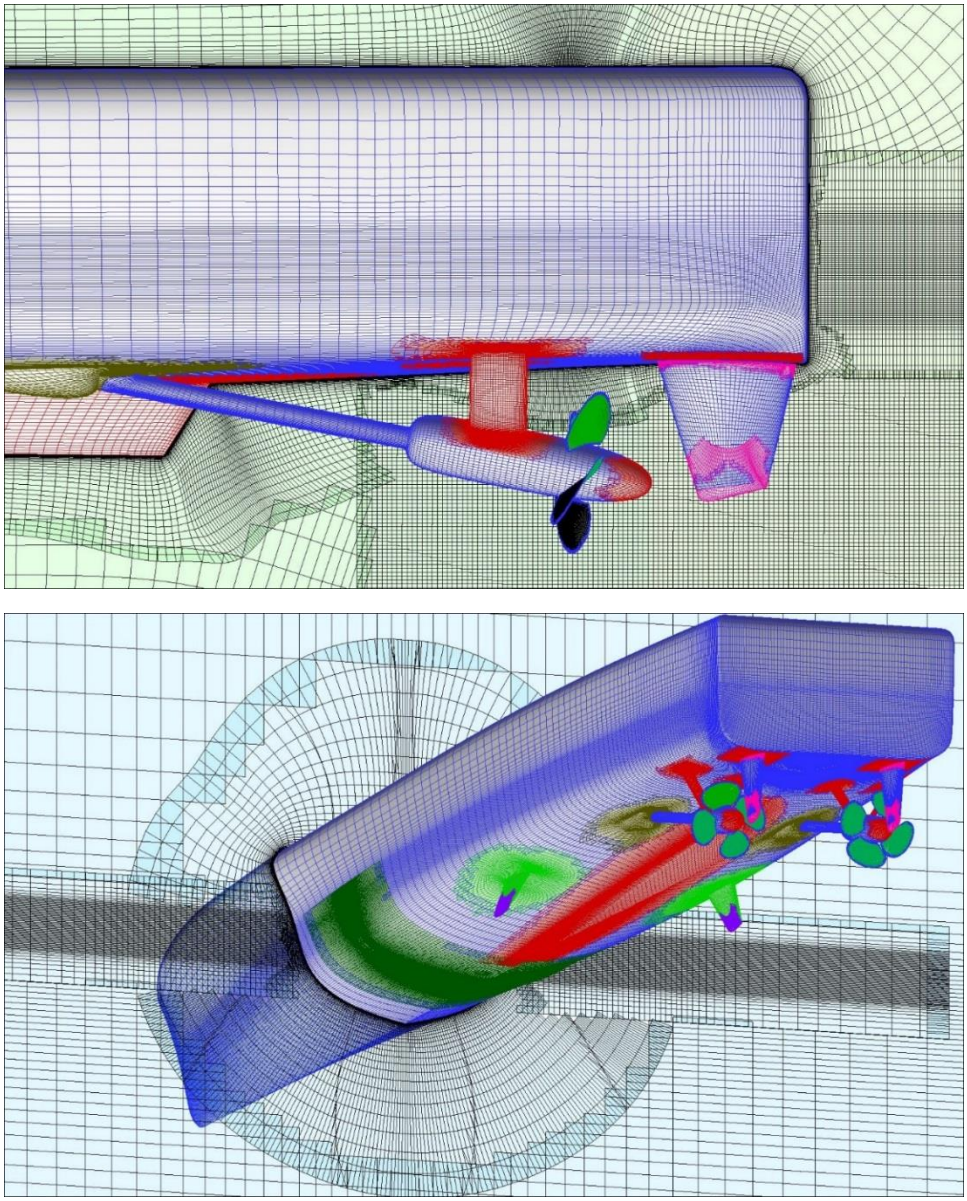

Figure 2.2: The overset grid structure around fully appended R/V Athena.

The ship hull grid with all its appendages such as propeller and rudders is considered as moving grid and the predicted-prescribed motions are applied to this grid. Finally, the refinement grid moving with the ship in the water has some degree of freedom such as surge, sway and yaw but not heave, roll or pitch. In computational domain any point is classified as a hole, interpolated or active points. Active points are points inside the computational

domain and the calculations are done on these points. Contrary to active points, hole points are inside the objects or outside the computational domain and they can be excluded from the computations by "blanking out". Interpolated points are links between different overset grids. In each time step, new interpolation coefficients are computed to link any moving grid with the static grid or between each other. Figure 2.3 from Carrica *et al*. (2007b) is a good example showing the overset grid system of active, interpolated and hole points inside a computational domain, and also donor cell with grid points in air and conforming the free surface.

To accomplish the simulation, the dynamic overset grid along with the external software Suggar (Noack, 2005) or Suggar++ (Noack *et al*., 2009) will be used to compute the domain connectivity for node centered solvers such as REX code or element centered solvers. The Suggar/Suggar++ is designed for any moving body problems and it can communicate with a motion controller such as the 6DOF module in REX code. In each time step, Suggar/Suggar++ is run separately from REX code to prescribe motions and provide the interpolation between the overset grids to the flow solver in REX code. Also, Suggar/Suggar++ can decrease the amount of overlap between the different grids by blanking out unneeded grid points in the overlap region which is helpful in minimizing the numerical inaccuracies introduced by overset by interpolating cells of dissimilar sizes. Another capability of Suggar is that this software can write the transformed grid system. To run Suggar, all objects within a general hierarchical organization and their motions are listed in an input file, including relative motions of child objects with respect to its parent such as a moving control surface attached to the ship hull that is also moving. Besides obtain interpolation coefficients, a treatment is needed to calculate the area, forces and moments

at no-slip surface of solid surfaces where grids have overlap. To avoid counting the same area more than once, another tool named USURP (Boger and Dreyer, 2006) is used to provide weights to the active points on the no-slip surfaces resulting in the correct area, forces, and moments. USURP is utilized as a pre-processing step since there is no change in overlap on the solid surfaces such as the bare hull ship geometry at running time.

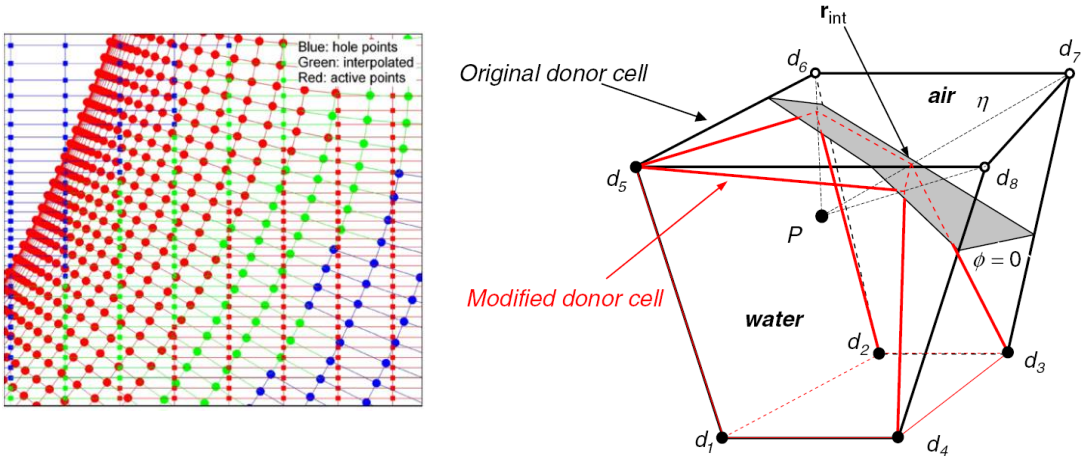

Figure 2.3: The overset grid system for (left) overset grid arrangement of hole, interpolated and active points (right) donor cell with grid points in air and conformation to free surface (Figures from Carrica *et al*., 2007b).

2.3 Numerical Methods

For numerical simulation of complex geometry using REX, a coordinate transformation is used to transform physical domain in Cartesian coordinates (X, Y, Z, t) into the computational domain in non-orthogonal curvilinear coordinates (ξ, η, ζ, τ). Therefore, all governing equations including the mass, momentum and turbulence equations (2.1), (2.2), (2.9) and (2.10) are change into the new form as:

$$\frac{1}{J}\frac{\partial}{\partial \xi^j}\left(b_i^j u_i\right) = 0 \tag{2.38}$$

$$\frac{1}{J}\frac{\partial}{\partial\tau}(Ju_i)+\frac{1}{J}b_j^k\left(u_j-\frac{\partial x_j}{\partial\tau}\right)\frac{\partial u_i}{\partial\xi^k} \tag{2.39}$$

$$=-\frac{1}{J}b_i^k\frac{\partial p}{\partial\xi^k}+\frac{1}{J}\frac{\partial}{\partial\xi^j}\left(\frac{b_i^j b_i^k}{JRe_{eff}}\frac{\partial u_i}{\partial\xi^k}\right)+\left(\frac{b_j^k}{J}\frac{\partial v_t}{\partial\xi^k}\frac{b_i^l}{J}\frac{\partial u_j}{\partial\xi^l}\right)+S_i$$

$$\frac{\partial k}{\partial\tau}+\frac{1}{J}b_j^k\left(u_j-\frac{\partial x_j}{\partial\tau}\right)\frac{\partial k}{\partial\xi^k}=\frac{1}{J}\frac{\partial}{\partial\xi^j}\left(\frac{1}{J}\left(\frac{1}{Re}+\sigma_k\gamma_t\right)b_i^j b_i^k\frac{\partial k}{\partial\xi^k}\right)+S_k \tag{2.40}$$

$$\frac{\partial\omega}{\partial\tau}+\frac{1}{J}b_j^k\left(u_j-\frac{\partial x_j}{\partial\tau}\right)\frac{\partial\omega}{\partial\xi^k}=\frac{1}{J}\frac{\partial}{\partial\xi^j}\left(\frac{1}{J}\left(\frac{1}{Re}+\sigma_\omega\gamma_t\right)b_i^j b_i^k\frac{\partial\omega}{\partial\xi^k}\right)+S_\omega \tag{2.41}$$

where in Eqs. (2.40) - (2.41) the corresponding sources are:

$$S_k=\gamma_t\frac{1}{J^2}\left(b_j^k\frac{\partial u_i}{\partial\xi^k}+b_i^k\frac{\partial u_j}{\partial\xi^k}\right)\left(b_j^n\frac{\partial u_i}{\partial\xi^n}\right)-\beta^*\omega k \tag{2.42}$$

$$S_\omega=\gamma\gamma_t\frac{\omega}{k}\frac{1}{J^2}\left(b_j^k\frac{\partial u_i}{\partial\xi^k}+b_i^k\frac{\partial u_j}{\partial\xi^k}\right)\left(b_j^n\frac{\partial u_i}{\partial\xi^n}\right)-\beta\omega^2+2(1 \tag{2.43}$$

$$-F_1)\sigma_{\omega 2}\frac{1}{\omega}\frac{1}{J^2}\left(b_i^m\frac{\partial k}{\partial\xi^m}\right)\left(b_i^n\frac{\partial\omega}{\partial\xi^n}\right)$$

In these equations J represents the Jacobian and b_i^j is the matrices of the transformation. Also, the transport mass equation (2.4) is also re-written as:

$$\frac{1}{J}\frac{\partial}{\partial\tau}(J\phi_i)+\frac{1}{J}b_j^k\left(u_j-\frac{\partial x_j}{\partial\tau}\right)\frac{\partial\phi_i}{\partial\xi^k}=0 \tag{2.44}$$

As the discretization strategy, the finite difference scheme is applied to discretize the equations using second-order implicit Euler scheme in time derivatives, second/fourth-order upwind for spatial discretization in convective terms and also second-order centered scheme for the viscous terms.

2.4 Solution Strategy in REX code

The solution strategy in REX code includes different steps summarized in Fig. 2.4. By running the code all the grids are read and split according to user directives for domain decomposition parallelization. Based on input file information, the user can specify the degrees of freedom of each moving grids at run time in grid system where these motions are prescribed or predicted on each degree of freedom. Generally, each block in grid system belongs to an object and this object can move independently from others or remain static. Each moving object is split into separate processors and by using the Message Passing Interface (MPI) based domain decomposition approach, each decomposed block is mapped to one processor which is responsible for computing the motion 6DOF equations for that object. After initializing all variables and setting initial conditions, Suggar (Noack, 2005) or Suggar++ (Noack *et al*., 2009) is called for the first time to obtain the initial overset interpolation information.

A nonlinear Picard iteration loop is used to converge the flow and motion equations within each time step. At the beginning of each iteration the overset information is read from a binary file produced by Suggar/Suggar++, the grids are moved according to the motions resulting from the 6DOF predictor/corrector steps, and the transformation metrics and grid velocity are computed. Inside this loop, each solver is called in sequence: the turbulence equations are solved first implicitly and the turbulent viscosity is computed in this step.

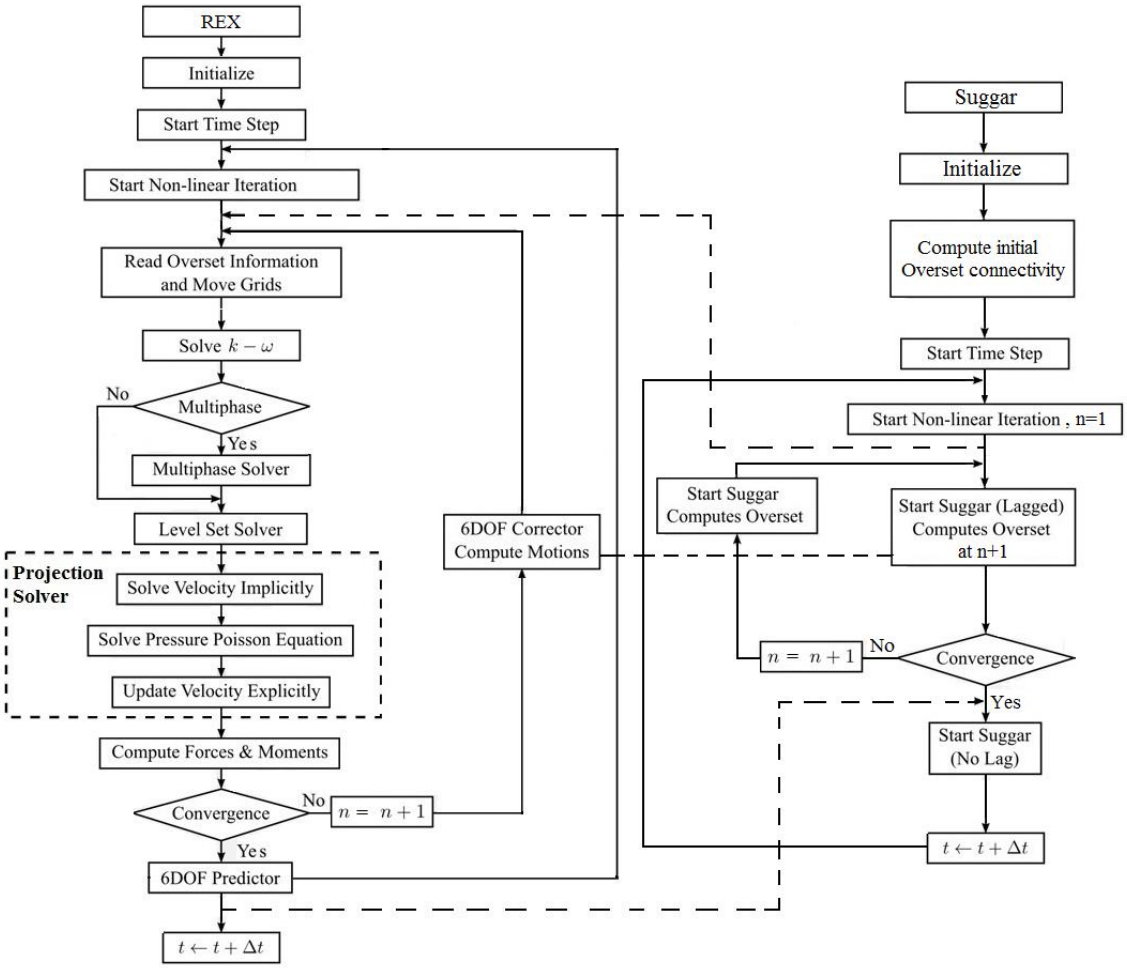

Figure 2.4: The solution strategy in REX code.

For two phase flow, the multiphase solver is included as an additional block in this sequence of solvers' calls to simulate the bubbly flow. In this step the gas momentum equations for each group are solved first in sequence. Then, in a sequence of time-splitting stages, entrainment, rectified diffusion, intergroup transfer and transport are solved in multiphase section. After computing the total void fraction in each non-linear iteration, the next step is followed by the level-set function transport and reinitialization. Then the momentum and mass equations are solved together using a projection method which in this step the new location of the free surface the pressure gradient is computed. By computing

the velocity field, the forces and moments are weighted with coefficients provided as a preprocessing step by USURP (Boger and Dreyer, 2006) used to compute forces and area on overlap regions for a ship hull with all its appendages. Finally, the motions are predicted for the next time step and Suggar/Suggar++ is called to compute the interpolation given the new location of the moving grids. Usually two to five inner iterations are required to have a converged flow flied and pressure within each time step. The inner iteration ends and goes to the next time-marching step when the residuals of all the variables reach into the convergence criteria set in input file (about $10^{-3} - 10^{-5}$).

2.5 Summary

In this Chapter the description of the numerical implementation of the mathematical model in REX is presented. Most of the specific equations including continuity, momentum, level-set and turbulence modeling in the solver are discussed briefly. As it is mentioned, REX uses a finite difference approach to discretization of the governing equations, and it is fully parallelized based on MPI domain decomposition. The parallel environment facilitates the communication of the CFD solver with other software available for specific calculation of required auxiliary information, such as overset connectivity, propeller modelling, or multibody dynamics.

CHAPTER 3 STRATIFICATION IMPLEMENTATION IN REX

3.1 Introduction

A short review of most of studies in fluid mechanics reveals that the fluid is usually considered to have constant density and the buoyancy term existing in real flows is ignored. Current stratified flow research in ship hydrodynamics applications is only limited to the phenomenon of wave propagation in the far-field rather than the mechanism of wave evolution and it is difficult to find a comprehensive numerical work that simulates the stratified flow around a ship or submarine. Most of the numerical simulations in stratified show that DNS and LES are the most common methods used for this phenomenon rather than other methods, which is impractical for ship applications. However, a few modifications in RANS methods can change this approach into suitable method for the simulation of stratified flow around objects. For instance, Venayagamoorthy *et al*. (2003) suggested a few modifications to RANS turbulence model to simulate the effects of stratification numerically. The newly modified model was applied to cases with weak and moderate stratification in open channel flow to show the effects of buoyancy on the flow field, and the velocity and density profiles inside the channel were compared with the results of DNS method showing acceptable accuracy for the modified model. However, it was only used for channel flow and not for flow over a complex geometrical object.

Therefore, the challenge for this thesis is to simulate the ocean stratification in ship hydrodynamics by incorporating the numerical model into the naval hydrodynamics code REX and provide a new version of the code that can run the same complex situations that the single phase version can run. In the next sections, the implementation and code

development contributions for stratification are presented and the new modifications to governing equations are used to simulate the stratified flow in the flow field of surface ships and submarines. The new model and numerical approach for stratified flow is validated against data for two different geometries including a square cavity and for the generation of internal waves in the flow past a sphere.

3.2 Implement of Density Stratification into REX

In general, non-stratified turbulent flows have a complex nature and the numerical simulation of these flows with constant density only requires the mass and momentum equations to describe the fluid flow. Since the density is constant, it does not play a major rule in simulations. However, when the flow is stratified by means of salinity-temperature differences, an additional level of complexity is added to the flow and the energy equation, a simple advection-diffusion equation of density, coupled with mass and momentum equations is required to solve the fluid flow. In a natural stratified environment such as the oceans and seas the density distribution can be defined as a constant reference density, ρ_0, plus a small departure term which can be considered as fluctuating part, $\rho'(x, y, z, t)$, as:

$$\rho(x, y, z, t) = \rho_0 + \rho'(x, y, z, t) \tag{3.1}$$

It is assumed that density fluctuations are negligible in the inertial terms and it can be retained as buoyancy term in momentum equation when $\rho'/\rho_0 \ll 1$. By defining the $\rho' = \tilde{\rho}.\Delta\rho$, the governing equations for stratified flow can be written as:

Mass:

$$\frac{\partial(\tilde{\rho} Ri\, Fr^2)}{\partial t} + \frac{\partial\left(1 + \tilde{\rho} Ri\, Fr^2\right)u_j}{\partial x_j} = 0 \tag{3.2}$$

Momentum:

$$\frac{\partial\left(1+\tilde{\rho}Ri\,Fr^2\right)u_i}{\partial t}+\frac{\partial\left(1+\tilde{\rho}Ri\,Fr^2\right)u_iu_j}{\partial x_j}=-\frac{\partial p}{\partial x_i}+\frac{\partial}{\partial x_j}\left[\frac{1}{Re_{eff}}\left(\frac{\partial u_i}{\partial x_j}+\frac{\partial u_j}{\partial x_i}\right)\right]-Ri\rho^*\vec{\mathbf{k}} \tag{3.3}$$

where $\tilde{\rho}=(\rho-\rho_0)/\Delta\rho$ is the instantaneous excess density with respect to the reference density ρ_0, with $\Delta\rho$ as reference density difference typically chosen as the density difference from the free surface and a location at depth, $\rho^*=(\rho-\rho_H(z))/\Delta\rho$ is the excess density with respect to the unperturbed background density profile $\rho_H(z)$, and p the piezometric pressure, all dimensionless. A modified piezometric pressure can be defined to include background stratification as $p=\frac{p_{abs}}{\rho_0U_0^2}+\frac{2}{3}k+Ri\int_0^z\left(\frac{\rho_H(z')}{\Delta\rho}\right)dz'$ with p_{abs} the absolute pressure respect to atmosphere and k the turbulent kinetic energy. The definitions of Reynolds and Froude numbers are the same as provided in Chapter 2. The third term in R.H.S of Eq. (3.3) includes a non-dimensional number representing the ratio of buoyant to inertial forces and it is defined as bulk Richardson number:

$$Ri=\frac{\Delta\rho}{\rho_0}\frac{gL_0}{U_0^2} \tag{3.4}$$

The bulk Richardson number can also be expressed as an internal, reduced or densimetric Froude number, Fr_i, which is defined as :

$$Fr_i=\frac{U_0}{\sqrt{\frac{\Delta\rho}{\rho_0}gL_0}} \tag{3.5}$$

Therefore, the relation between bulk Richardson number, usual Froude number and densimetric Froude number can be expressed as:

$$Ri = \frac{\Delta\rho}{\rho_0}\frac{1}{Fr^2} = \frac{1}{{Fr_i}^2} \tag{3.6}$$

For the homogeneous flow the Richardson number, Ri, is equal zero and subsequently the buoyancy term is zero. An increased complexity related to stratification is obtained by the extra buoyancy term in the Navier-Stokes equations. The only external force included in these equations is gravity force. The simulation of stratified flows requires additional equations due to density variable since it affects the behavior of Eqs. (3.2) and (3.3). For an incompressible flow as a special case of energy conservation, the transport of density can be considered as the transport of any scalar coupled with Eqs. (3.2) and (3.3). The density transport equation is defined as an advection-diffusion equation given by:

Density:

$$\frac{\partial\tilde{\rho}}{\partial t} + \frac{\partial\left(\tilde{\rho}u_j\right)}{\partial x_j} = \frac{\partial}{\partial x_j}\left[\left(\frac{1}{Re.Pr} + \frac{\nu_t}{Pr_t}\right)\frac{\partial\tilde{\rho}}{\partial x_j}\right] \tag{3.7}$$

where $Pr = \nu/\alpha$ is the Prandtl number with α the molecular diffusivity and ν is the fluid viscosity.

In section 2.2.3 and through Eqs. (2.9) and (2.28) a detailed definition of turbulence model used in REX code is presented which is applicable for non-stratified flow. For the case of stratified flow, the blended $k-\varepsilon/k-\omega$ model is modified by adding buoyancy source term. The modified source terms in the turbulence equations (2.9)-(2.10) are defined as (Menter, 1994; Yeoh and Tu, 2010):

$$S_k = -\nu_t\tau_{ij}\frac{\partial u_i}{\partial x_j} + \beta^* k\omega - Ri\frac{\nu_t}{\sigma_\rho}\frac{\partial\tilde{\rho}}{\partial z} \tag{3.8}$$

$$S_\omega = \omega\left(\beta^*\omega - \frac{\gamma\nu_t}{k}\tau_{ij}\frac{\partial u_i}{\partial x_j}\right) - 2(1-F_1)\frac{\sigma_{\omega 2}}{\omega}\frac{\partial k}{\partial x_j}\frac{\partial \omega}{\partial x_j} - \alpha_3 Ri\frac{\nu_t}{\sigma_\rho}\frac{\omega}{k}\frac{\partial \tilde{\rho}}{\partial z} \tag{3.9}$$

The buoyancy terms in Eqs. (3.8)-(3.9) are modeled following Yeoh and Tu (2010) as:

$$\alpha_3 = F_1\alpha_1 + (1-F_1)\alpha_2 \tag{3.10}$$

where $\alpha_1 = 0.31$ and $\alpha_2 = 0.44$. Also a turbulent Schmidt number $\sigma_\rho = 1$ is defined for the buoyancy terms (Venayagamoorthy *et al*., 2003; Shih *et al*., 2005).

3.3 Numerical Methods

In this section the numerical methods used to solve the fluid flow and implementation of density solver into the REX code are described in details. Eq. (3.7) includes three terms as time derivation, convection and diffusion. For the dimensionless density field, $\tilde{\rho}$, the following approximation can be used for time derivatives to advance the solution from t_n to t_{n+1}:

$$\frac{\partial}{\partial t}(\tilde{\rho}) = \frac{1}{\delta t}\{w_{n-1}\tilde{\rho}^{n-1} + w_n\tilde{\rho}^n + w_{n+1}\tilde{\rho}^{n+1}\} \tag{3.11}$$

where w is the weight coefficient and depending on its value, it determines the time marching scheme including Implicit Euler, second order backward difference formula (BDF2) and Crank-Nicolson. For the convection term, different schemes can be used to discretize the density transport equation. In REX, these schemes include 1st –order upwind, 2nd –order upwind, 3rd –order upwind, 4th–order upwind and 2nd /3rd order hybrid. The strategy to solve the density transport equation in REX is sketched in Fig. 3.1. The solver starts with an iteration loop to build a matrix system including convection and diffusive terms. The diffusion term of the matrix is built every time by updating the diffusion

coefficient as the computation evolves. Finally, after assembling the matrix an ADI-like iteration for all three spatial directions is done and the iteration will continue until the residual of all density field reaches into the convergence criteria set in input file (typically 10^{-3}-10^{-5}). The density solver is placed before the level-set solver in the main loop of REX (see Fig. 2.4).

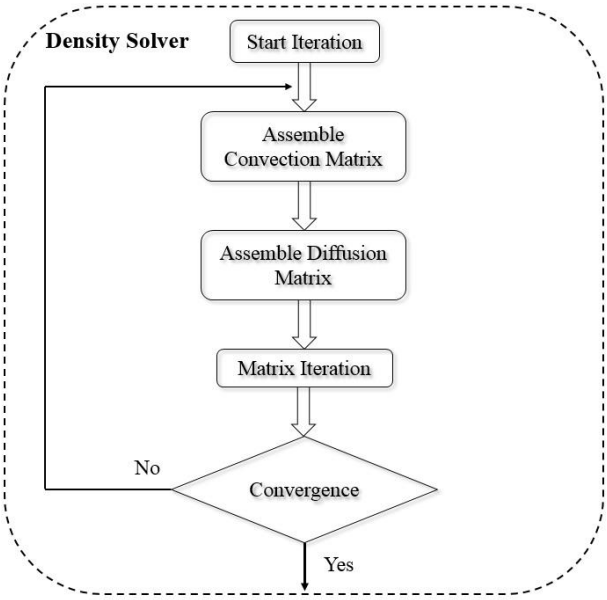

Figure 3.1: Iterative scheme for the density transport equation implemented in REX code.

3.4 Validation

The predictability and behavior of the implemented model in REX are examined by comparing the numerical simulations against numerical and experimental results from two independent studies. As the first case, a simple two-dimensional square cavity is chosen and then a three dimensional more complex case of stratified flow around a sphere at different conditions is simulated numerically for validation of the code.

3.4.1 Square Cavity

The first test case, used to check the implementation of the density equation, is the laminar flow inside a 2D square cavity with a temperature gradient, which causes a density change. The relation between density and temperature is defined as $\rho = \rho_0(1 - \beta_T(T - T_{cold}))$, where ρ_0 is a characteristic density, and β_T is the volumetric expansion coefficient. This case was studied by Al-Amiri *et al*. (2007), with the boundary conditions shown in Fig. 3.2. The upper boundary moves with constant unit velocity while all other boundaries are at rest. The side walls are adiabatic (which translates in the present formulation to a zero gradient condition, $\partial\tilde{\rho}/\partial x = 0$), while the upper and lower walls have Dirichlet boundary conditions $\tilde{\rho} = 0$ and $\tilde{\rho} = 1$, respectively. $Pr = 1$, $Re = 500$, and $Ri = 4 \times 10^{-4}$ were used. All results are shown in dimensionless units.

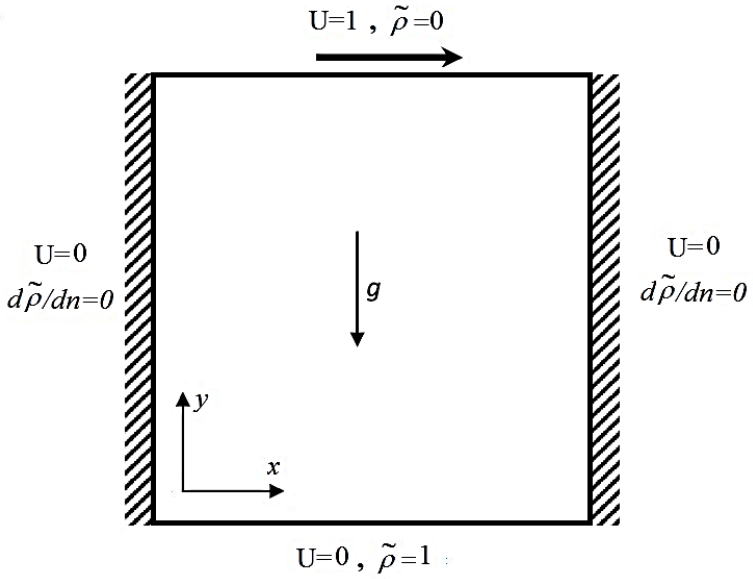

Figure 3.2: Boundary conditions for square cavity with temperature gradient.

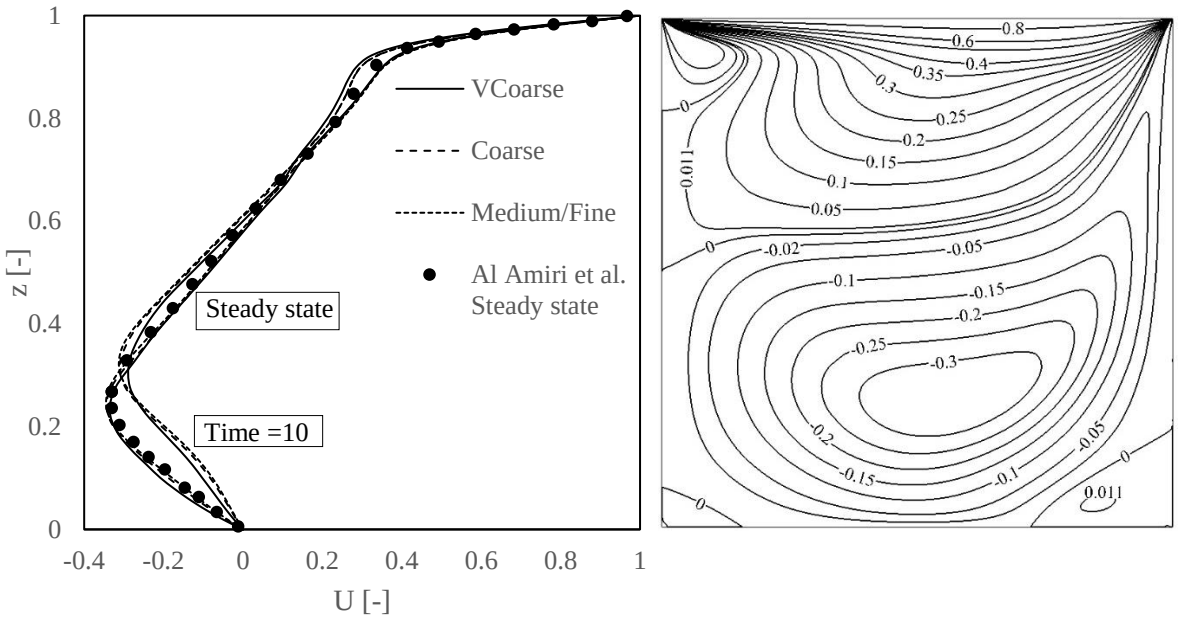

Figure 3.3: U-velocity profile at the vertical center line (left) and contours (right) for the lid-driven cavity.

To evaluate grid convergence, computations were performed on four non-uniform grids with 41×41, 81×81, 161×161 and 321×321 grid points, named Very Coarse, Coarse, Medium and Fine grids. Time steps were varied between $\Delta t = 0.02$ for the Very Coarse grid to $\Delta t = 0.0025$ for the Fine grid, maintaining a constant Courant number.

Figure 3.3 shows the axial velocity at the vertical centerline of the cavity, which is in excellent agreement with the work of Al-Amiri *et al*. (2007). Since the solutions for the Medium and Fine grids are indistinguishable in the figure, they are shown as a single line. Axial velocity contours for the medium grid are also shown in Fig. 3.3. The density profile at mid-section shown in Fig. 3.4 exhibits again remarkable agreement compared with the results of Al-Amiri *et al*. (2007). In all cases solutions converge well in grid. Isocontours of density for this case are also depicted in Fig. 3.4, showing good agreement with Fig. 5 in Al-Amiri *et al.* (2007), though in their figure the authors do not show the contour magnitude.

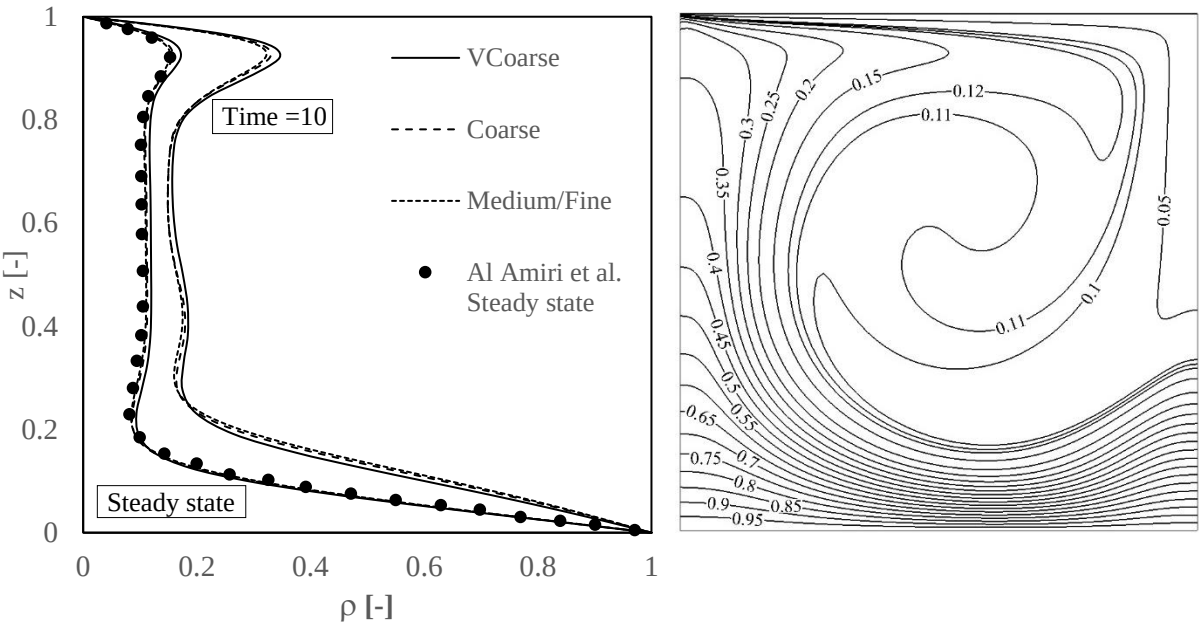

Figure 3.4: Density profile at the vertical center line (left) and contours (right) for the lid-driven cavity.

Time step convergence was analyzed for the medium grid, using time steps $\Delta t = 0.04, 0.02, 0.01, 0.005$ and evaluating solutions at $t = 10$. Grid and time step convergences were studied following the procedures described in Stern *et al*. (2001). Results for the maximum vertical velocity and density gradients at the top and bottom walls for steady state for the grid study and at $t = 10$ for the time step study are shown in Tables 3.1 and 3.2. For these studies a very large number of inner iterations was used so that the iterative error could be neglected. The grid study using the Very Coarse, Coarse and Medium grids showed that the solutions converge, but the Very Coarse grid is not in the asymptotic range, yielding unrealistically high order of accuracy P_G. Using the Coarse, Medium and Fine grids the study results in an order of accuracy close to second for all three variables evaluated, as expected since all equations are discretized to second order in space except the convection terms which are fourth order. The uncertainty U_{GC} is highest for the density gradient at the top

wall at approximately 0.4% of the fine mesh value. The time step analysis using the three smallest time steps, shown in Table 3.2, yields an order of accuracy a bit lower than second, though in time all equations are discretized using a second order Euler backward scheme. This may be because the differences between time steps are very small (on the fifth or sixth significant digit) and even tighter iterative convergence may be needed. Using the three larger time steps the order of accuracy is slightly closer to second. In both cases the time step uncertainty U_{TC} is very low, with the highest about 0.0006% in the bottom wall density gradient.

To further validate the model, the simulation of stratified flow over a sphere is considered and presented in next section. For different internal Froude numbers, the internal waves are simulated and compared to show the effect of internal Froude number on the pattern of internal gravity waves.

Table 3.1: Grid study for the density gradient and velocity along the vertical line at the center of the cavity in steady state.

Variable	Coarse Mesh	Medium Mesh	Fine Mesh	$\mathbf{R_G}$	$\mathbf{C_G}$	$\mathbf{P_G}$	$\mathbf{U_{GC}}$	Convergence type
$\left(\frac{d\rho}{dz}\right)_{Bottom\ wall}$	7.632039	7.625449	7.624179	0.19	1.34	2.37	1.2E-4	Monotonic
$\left(\frac{d\rho}{dz}\right)_{Top\ wall}$	3.913535	3.836199	3.814099	0.29	0.84	1.81	1.48E-3	Monotonic
$U_{z,max}$	0.065180	0.065665	0.065813	0.31	0.76	1.71	1.57E-5	Monotonic

Table 3.2: Time step study for density gradient and velocity along the vertical line at the center of the cavity at time=10.

Variable	$\Delta t = 0.02$	$\Delta t = 0.01$	$\Delta t = 0.005$	$\mathbf{R_T}$	$\mathbf{C_T}$	$\mathbf{P_T}$	$\mathbf{U_{TC}}$	Convergence type

$\left(\frac{d\rho}{dz}\right)_{Bottom\ wall}$	3.136232	3.136546	3.136651	0.333	0.666	1.59	1.75E-5	Monotonic
$\left(\frac{d\rho}{dz}\right)_{Top\ wall}$	7.862150	7.861966	7.861895	0.382	0.538	1.39	2.01E-5	Monotonic
$U_{z,max}$	0.103577	0.103571	0.103570	0.244	1.034	2.03	4.77E-8	Monotonic
	$\Delta t = 0.04$	$\Delta t = 0.02$	$\Delta t = 0.01$					
$\left(\frac{d\rho}{dz}\right)_{Bottom\ wall}$	3.134871	3.136232	3.136546	0.231	1.111	2.11	1.22E-5	Monotonic
$\left(\frac{d\rho}{dz}\right)_{Top\ wall}$	7.862702	7.862150	7.861966	0.34	0.67	1.6	3.07E-5	Monotonic
$U_{z,max}$	0.103597	0.103577	0.103571	0.303	0.765	1.71	6.05E-7	Monotonic

3.4.2 Towed Sphere

As the second case to test the implementation of the density equation, a sphere of diameter D is considered, moving steadily horizontally at a constant speed U in a uniformly stratified fluid with the density of $\bar{\rho}(z)$ (Bonneton *et al.*, 1993). The schematic representation of the problem is shown in Fig. 3.5. In the numerical simulation, the system is equivalent to the flow of an incompressible fluid uniformly stratified in density past a fixed sphere. In the experimental work, for an incompressible fluid the buoyancy (Brunt-Vaisala) frequency, N, is related to the undisturbed density field, $\bar{\rho}(z)$, by $N = \sqrt{-g/\rho_0\ \partial\bar{\rho}/\partial z}$ where ρ_0 is the density of the undisturbed liquid at the center level of the sphere and the flow is characterized by three external scales such as the squared buoyancy frequency, N, the diameter of sphere, D, and the speed of the sphere, U. These three parameters can be combined to form dimensionless similarity parameters for this stratified flow as Reynolds number, $Re = U\ D/\nu$, internal Froude number, $Fr_i = \frac{2U}{ND}$, and bulk Richardson number, Ri.

The internal Froude number is defined as the ratio of the inertia force to the buoyancy force and it is frequently used to characterize flow wakes in a stratified fluid.

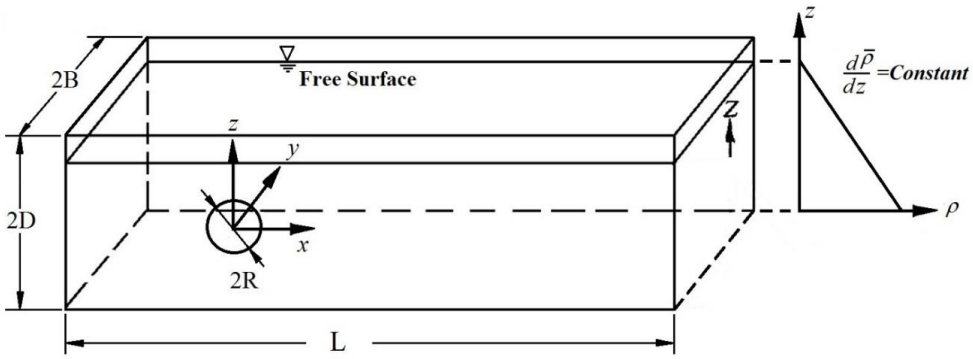

Figure 3.5: Schematic of the problem for the sphere towing in a tank.

The focus of this experimental work was on the generation of lee-waves and wake-emitted internal waves. For a range of Reynolds and internal Froude numbers, and using visualization techniques of internal waves, the authors showed the difference between lee waves and random waves. In this experiment, a sphere with diameter of $D = 2.24\ cm$ was towed in a tank filled with stably stratified salt water, whose linear density gradient creates a buoyancy frequency $N \approx 1.17\ s^{-1}$. For a given stratification and a given sphere, as the velocity changes, the two dimensionless numbers Fr_i and Re change together with the linear relation is $Re(Fr_i) = Re(1)Fr_i$, where $Re(1) = 2R^2N/\nu$ is the Reynolds number when $Fr_i = 1$. A constant $Re(1) = 253$, corresponding to experimental $N \approx 1.17$ rad/s and $R = 0.0112\ m$, was used for all simulations, although experimentally $Re(1)$ was varied in a larger range by changing the sphere diameter. This $Re(1)$ was chosen because of the extensive data available, and because is the lowest Reynolds number tested that allows computations in laminar mode without turbulence model. Details of the overset grid system are shown in Fig. 3.6 and Table 3.3. The computational domain extends $50D \times 20D \times 20D$ and is

discretized in $327 \times 269 \times 269$ points in x, y, and z directions, respectively, for a total of 23.7M grid points. The grid for the sphere, centered at $(x_c, y_c, z_c) = (0, 0, -60)$, is discretized with three overset blocks for a total of 2.8M points. No turbulent model was used for the simulations.

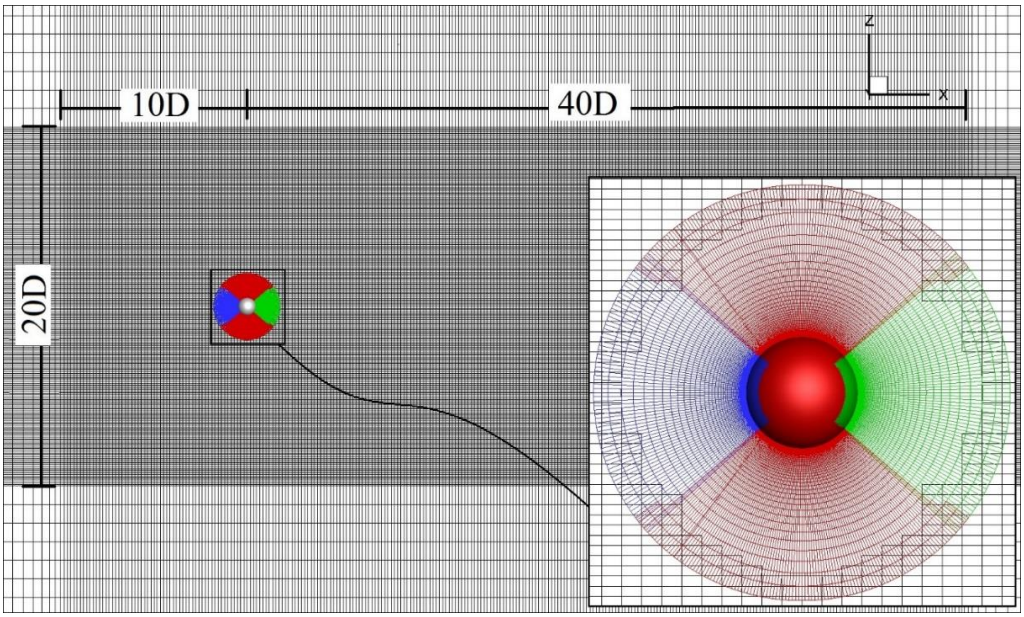

Figure 3.6: Overset grid system for the towed sphere problem.

Table 3.3: Details of the grid for the towed sphere.

Grid	Size	Total Points
Sphere_block1	$122 \times 81 \times 121$	1,195,722
Sphere_block2	$138 \times 81 \times 73$	815,994
Sphere_block3	$73 \times 81 \times 138$	815,994
Background	$327 \times 269 \times 269$	23,662,047
Total		26,610,381

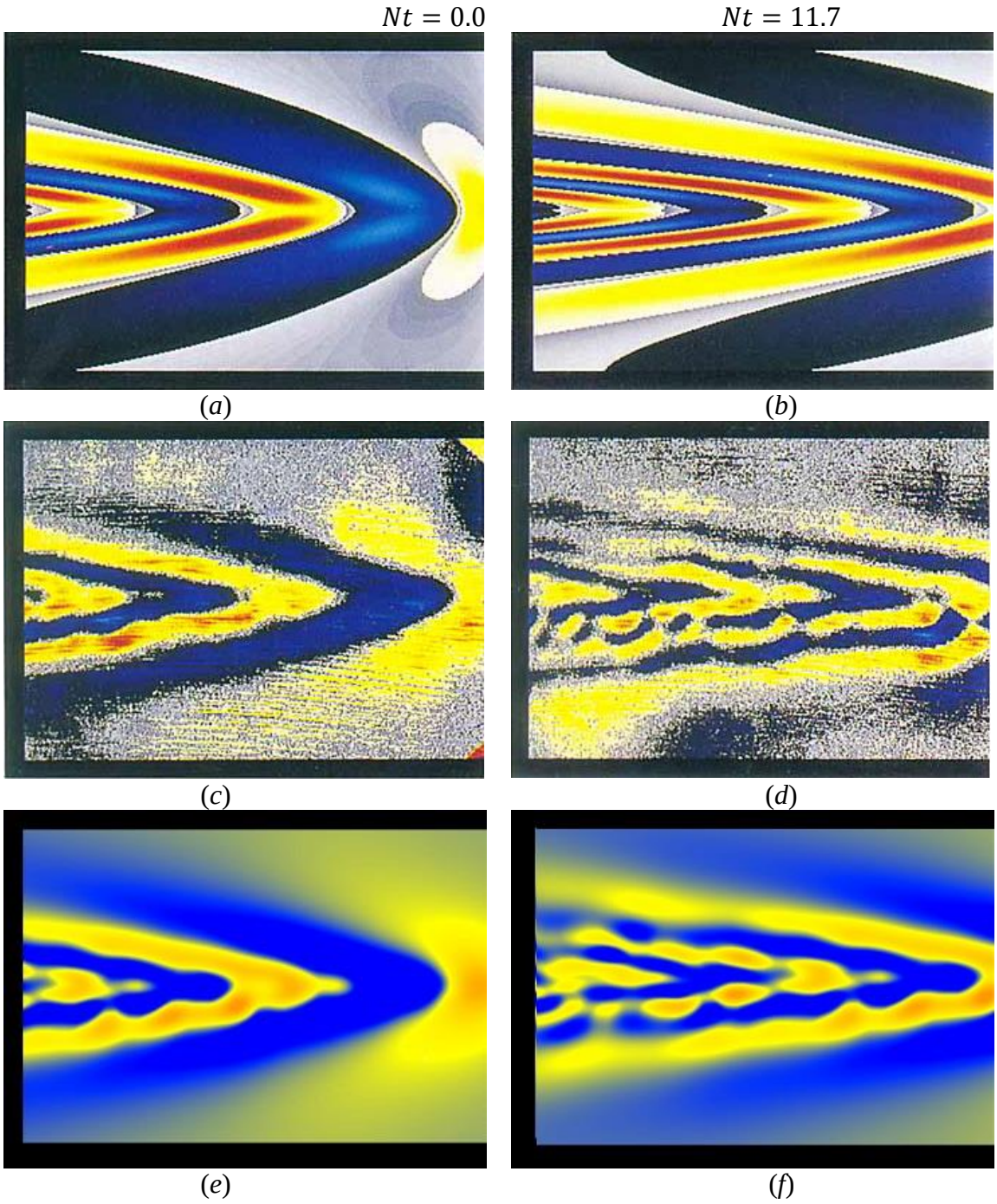

Figure 3.7: The linear theory (top), experimental visualization (middle) and CFD (bottom) results of vertical displacement ζ related to the lee wave in a horizontal plane at |z| = 3R below the center of the sphere for $Fr_i = 10/\pi$ and $Re(1) = 253$.

Figure 3.7 shows experimental and linear theory results from Bonneton *et al*. (1993) along with the present CFD results of vertical displacement ζ of the lee wave in a horizontal plane at $|z| = 3R$ below the center of the sphere and for $Fr_i = 10/\pi$ and $Re(1) = 253$, which corresponds to $Re \approx 803$. The vertical displacement ζ of the lee wave in a horizontal plane is presented at $|z| = 3R$ below the center of the sphere. The lee wave pattern is clearly captured by the CFD simulation, and the wave amplitude and the angle between the phase line and the *x*-axis are in good agreement with the experimental and linear theory results.

The same plane is shown in Fig. 3.8 for different internal Froude numbers $Fr_i = 10/\pi, 5,\ 30/\pi$, while maintaining the same $Re(1) = 253$ (as previously discussed, the actual Reynolds number increases linearly with Fr_i) to show the time dependence of the wave field. The results are consistent with Bonneton *et al*. (1993) and show a change from lee-wave-dominated regime to a random-wave-dominated one at $Fr_i \approx 4.5$. Their observation of Reynolds-independent transition was not checked in this work, as a single $Re(1)$ was considered. Similarly to experimental results presented in Bonneton *et al*. (1993), it is observed that for $Fr_i = 10/\pi$ the dominant waves are the lee waves in both $Nt = 0.0$ and $Nt = 11.7$. However, for $Fr_i = 30/\pi$ the dominant waves from the beginning are another wave type called random waves, observed as pieces of semicircular concentric (SCC) phase line patterns in flow domain. Internal Froude number $Fr_i = 5$ is close to the critical internal Froude number $Fr_{i,cr} = 4.5$, the transition between lee wave-dominated and random-wave dominated regime, and it is observed that in this case the lee waves observed at $Nt = 0.0$ and then at $Nt = 11.7$ both lee waves and random waves are observed in flow domain.

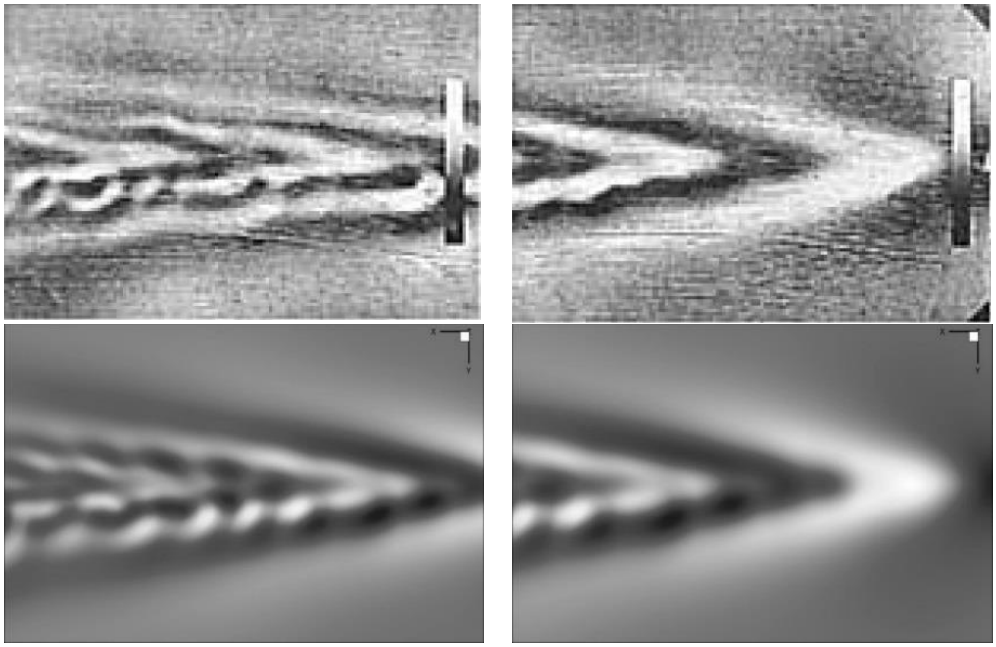

$Fr_i = 10/\pi$

EFD

CFD

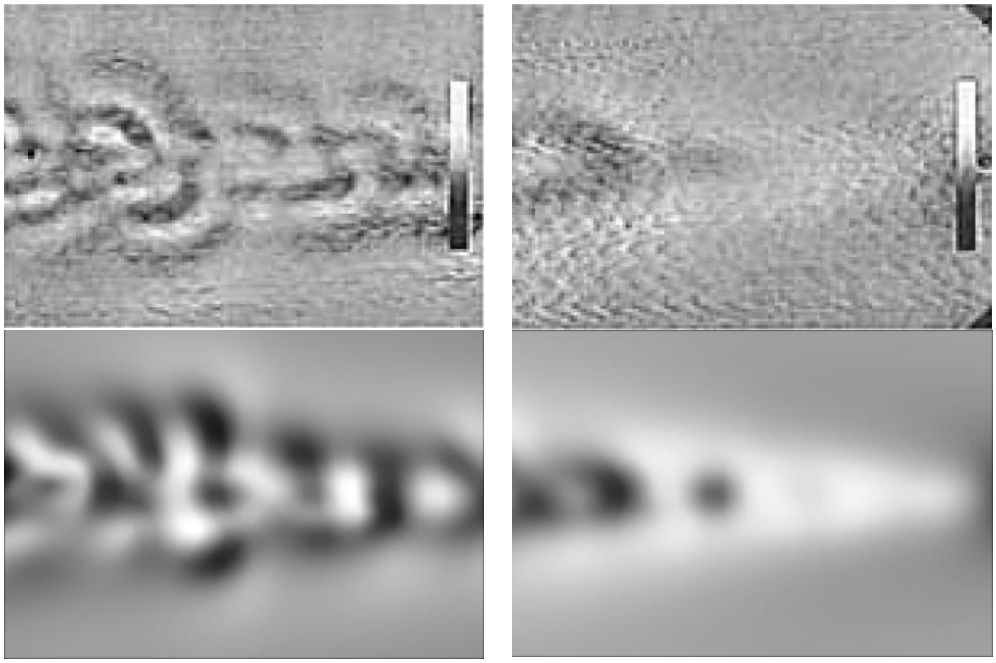

$Fr_i = 5$

EFD

CFD

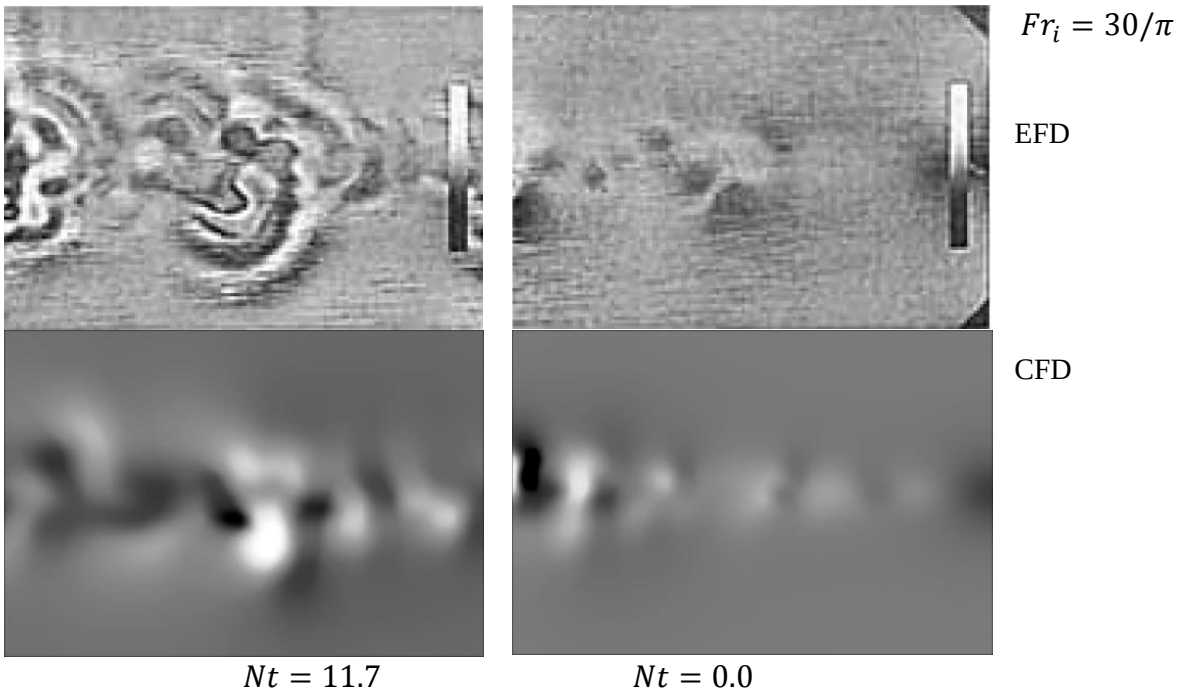

Figure 3.8: Temporal evolution of the visualization of the internal waves in a horizontal plane |z| = 3R below the center of the sphere. The scale is 46.5R × 32R.

The wavelength (Fig. 3.9) and wave amplitude (Fig. 3.10) were also analyzed. The wavelength of random waves is shown in Fig. 3.9 as presented by Bonneton *et al*. (1993). It is shown that the for both different internal Froude numbers the wavelength decreases while the Nt increases. Also, for the same Nt, the case with $Fr_i = 10/\pi$ has smaller wavelength than the case with $Fr_i = 5$.

The maximum wave amplitude of both lee waves and random waves are shown in Fig. 3.10. For the random waves, it is shown that the maximum amplitude increases as the internal Froude number increases which is in agreement with the experimental results. Current turbulent implementation in REX is not suitable for low Reynolds numbers, hence the highest $Re(1)$ used by Bonneton *et al*. (1993) was not simulated. Random wavelength

for the highest Fr_i number is not reported as it cannot be accurately obtained from our solution. Lee wave amplitude is also reported for the lowest Fr_i number only, as random wave dominates over lee waves as Fr_i increases. While there is some discrepancy between the computations and experimental results in Bonneton *et al*. (1993), likely due to the different Reynolds numbers used, Figs. 3.7-3.10 show a remarkable level of agreement between CFD and experiments, suggesting that the modeling approximations and numerical implementation are appropriate to capture the main features of the flow, including wavelength and amplitude of internal wave in a stratified flow.

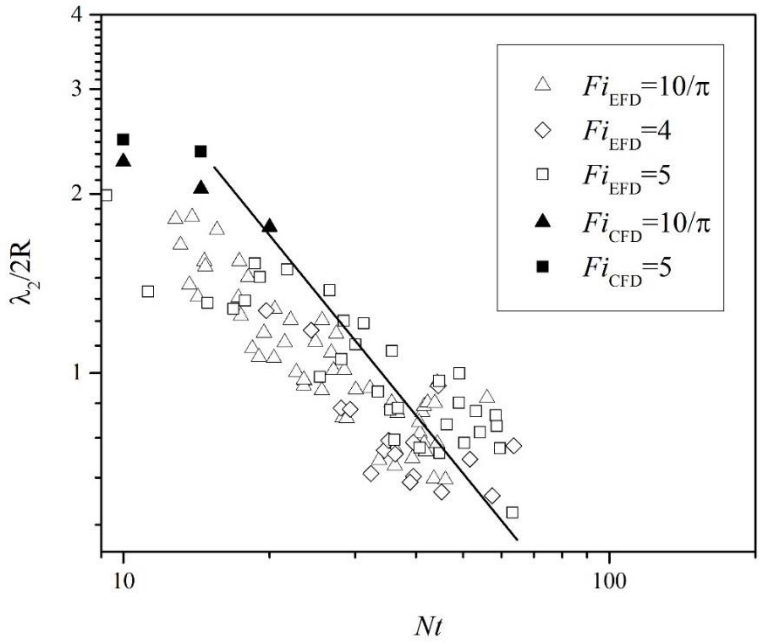

Figure 3.9: Wavelength of the random wave as a function of Nt, measured at the center of the sphere for internal Froude number $Fr_i = 10/\pi$ to $Fr_i = 5$ and $Re(1) = 253$.

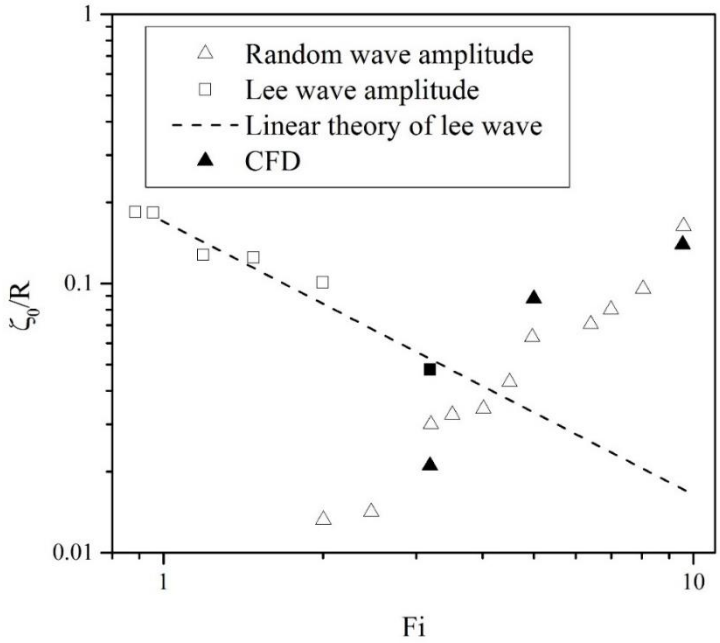

Figure 3.10: Internal wave amplitude as a function of the internal Froude number, measured at $|z| = 3R$ above the center of the sphere and 80R downstream, for $Fr_i = 10/\pi$ and $Re(1) = 253$.

3.5 Summary

In this Chapter full density effects were implemented into the naval hydrodynamics code REX to handle variable density effects in momentum transport and turbulence modeling in simulation of ocean stratification for ship hydrodynamics applications. All the governing equations including mass, momentum and turbulence equations were modified and a new transport equation for the density was introduced to solve the density field with a higher-order transport equation coupled with momentum and mass conservation. Also the boundary conditions in REX were also modified to handle the stratified flow. To test the implementation of the density equation into the REX code, two validations were performed for the cases of a heated square cavity and of a sphere advancing in a stably stratified fluid, showing in both cases good agreement with available numerical or experimental results.

CHAPTER 4 NEAR-FIELD FLOW OF SUBMARINES AND SHIPS ADVANCING IN STABLY STRATIFIED FLUID

4.1 Introduction

In this chapter numerical computations are performed to test the capabilities of the density solver added to REX for the simulation of a surface ship and submarine moving in different conditions of stably stratified flow. Some efforts studying the effects of density stratification on surface ship waves are available in the literature; in general these efforts are geared towards a description of the far-field rather than the accurate prediction of the interaction between the ship and the stratification field. Earlier works by Hudimac (1961) and Crapper (1967) presented analytical approaches to study the internal wave modes caused by a moving body in a two-layered ocean. It follows from their work that, just as for surface waves, at ship speeds sufficiently larger than the internal wave speed only divergent waves travel downstream of the ship, while both divergent and transverse waves are present for slower vessels. Tulin *et al*. (2000) suggested a nonlinear theory to capture internal wave behavior at high densimetric Froude number in weakly stratified flow that compared satisfactorily with available experimental results for a semi-submerged spheroid. Chang *et al*. (2006) presented one of the few available examples of CFD computation for vessel in a stratified medium. They computed the generated internal and surface waves of the notional DARPA Suboff submarine advancing in a two-layer fluid, for different surface Froude numbers ($Fr = U_0/\sqrt{gL_0}$), and found the evolution of the wave pattern consistent with previous predictions. As a detailed study in this area, in this chapter the evolution of the stratified flow in the near-field of a surface ship and a submarine is studied. The description of the vessels' geometry includes their moving control surfaces and propellers, resulting in

localized intense mixing absent in previous calculations of this type of problem. Finally, demonstration cases for the surface ship R/V Athena and the notional submarine Joubert operating near the surface in a stably stratified fluid are presented.

4.2 Near-Field Stratified Flow for a Surface Ship

As the ship surface geometry, the US Navy research vessel Athena is chosen to simulate the near-field stratified flow. The simulations are performed for both stratified and non-stratified flows to show the differences of all these environments and their effect on the ship motions. This high-speed research vessel is a transformed model of PG-94 Asheville-class patrol gunboat which was introduced in 1976. The ship has a variable pitch system of twin counter-rotating propellers, powered either by gas turbine or diesel engine reaching into the maximum speed of $U_s = 35$ or $13\ knots$, respectively. The hull is made of aluminum and the fully appended Athena geometry includes a skeg, starboard and port roll stabilizers and a compound masker ring on the hull at approximately $x/L_0 = 0.45$. The reason of choosing R/V Athena for these simulations is that the model scale of this ship has been used extensively for both experimental and numerical simulations during last decades (Crook, 1981; Day *et al*., 1980; Jenkins, 1984; Bhushan *et al*., 2009; Johansen *et al*., 2010; Bhushan *et al*., 2012) which enables the researchers to compare their results with benchmark data. Views of the ship model including the propellers are shown in Fig. 4.1, with main particulars listed in Table 4.1. For the stratified environment, a fairly strong stratified condition with density profile obtained at the Kitimat Bay station, Canada, is chosen.

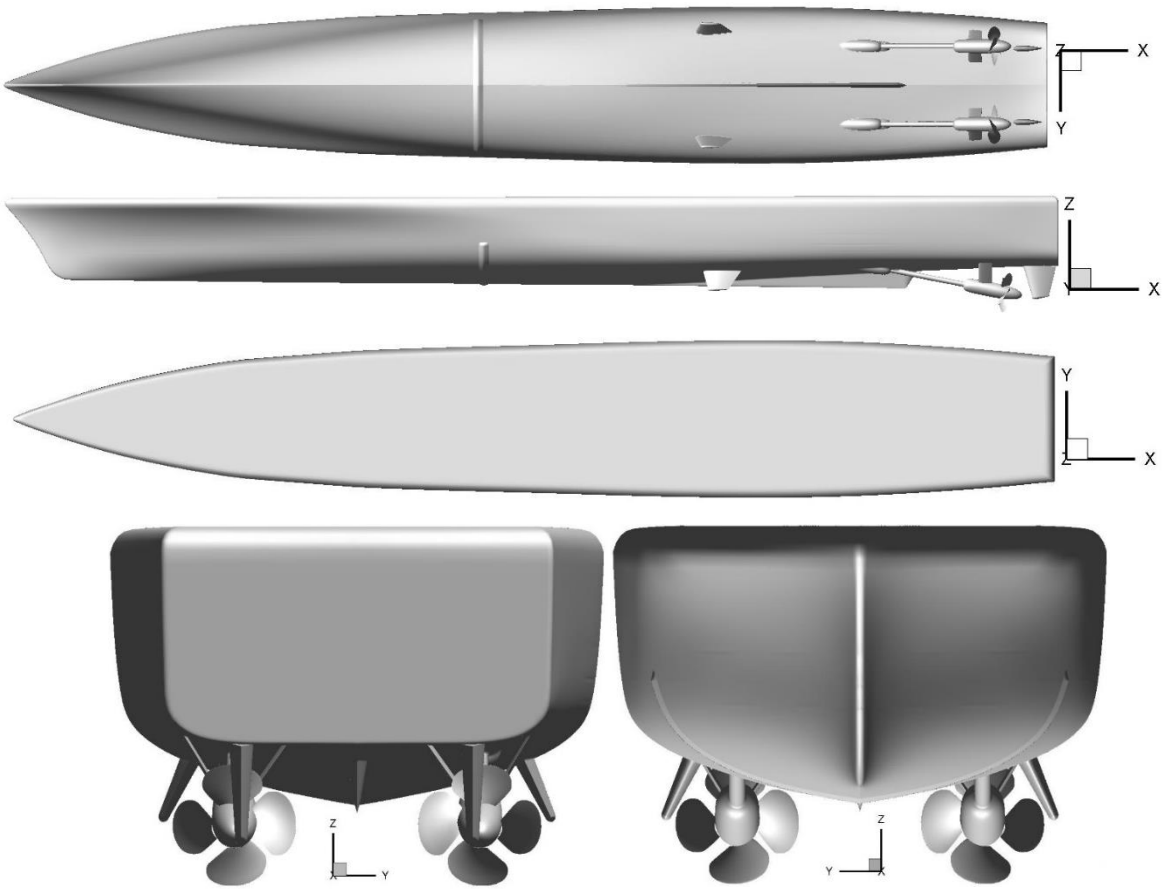

Figure 4.1: Research vessel Athena geometry and coordinate system.

Table 4.1: Main particulars of R/V Athena.

Length overall submerged	47.2 m
Beam	7.16 m
Maximum draft	3.2 m
Top speed	35 m/s
Maximum shaft power	9700 kW
Design displacement	245 tons

4.2.1 Grid Design of R/V Athena

The overset grid topology of fully appended R/V Athena is shown in Fig. 4.2, while details of the grid system are presented in Table 4.2. The computations are performed using discretized rotating propellers, while the rudders are also movable to enable computation of maneuvers. The grid contains of 65 grid blocks with about 31 million grid points, distributed for parallel computation. Processor distribution is dependent on machine characteristics, such as memory and speed, but a typical distribution uses 192 computing processors with 168 processors assigned to CFD calculation (about 110k grid points per processor) and 10 processors for running connectivity solver Suggar; idle processor are required to accommodate Suggar memory requirements. As it is shown in Table 4.2 most of the grid points belong to refinement and background blocks to resolve the flow around the propeller and rudder and on the wake to resolve vortical structures and flow features in those regions, and better capture the hull/propeller/rudder interactions. Appendages are handled using overset grids. The grids have a collar surface grid that conforms to the hull, and other surface grids that conform to the appendage itself. From these surface grids volume grids are generated using hyperbolic solvers provided by the commercial grid generation software Gridgen. The ship's grids move in six degrees of freedom (6DoF) following the predictions of the 6DoF solver, while free surface-attached grids only move with the ship in the horizontal plane. The propeller and rudder grids rotation around their shaft axes (as prescribed by the heading and speed controllers) is composed to the vessel predicted motion, using a hierarchical motion structure. The Cartesian grid connecting the ship to the far-field boundary conditions, called Background grid in Table 4.2, follows the ship but is not allowed to pitch, heave or roll so that the refinements in this grid, designed to resolve the

free surface, stay horizontal. The overset domain connectivity solver Suggar++ (Noack *et al*., 2009) is used, running in multiple lagged mode with 10 processes to match the execution time of the CFD solver. Before running the code for simulation, the longitudinal location of the center of gravity, the mass and the static wetted area of the ship in static condition with zero resulting pitching moment and weight balancing buoyancy are obtained using a pre-processing hydrostatic computation. Though these values are usually provided for design conditions, CFD values can deviate by a small amount (typically less than 0.1%) due to the fact that the geometry was discretized. The resulting dimensionless values for the mass, longitudinal location of center of gravity and static wetted area are 0.002588, 0.574055 and 0.162386, respectively. Generally, the preprocessing step requires setting up inputs and running Suggar++ with appropriate boundary conditions, generating the grids, checking the orphan points for grid system, and running USURP (Boger and Dryer, 2006) to obtain the information of overset surface panels for force integration over solid boundaries.

Table 4.2: Grid system for the self-propelled computations of R/V Athena.

	Grid	Type	Total Points	Moves with
Hull	Boundary layer starboard	Double-O	1,300,578	Ship
	Boundary layer port	Double-O	1,300,578	
	Rudder gap starboard	Curvilinear box	217,260	
	Rudder gap port	Curvilinear box	217,260	
Masker	Masker	Wrap	863,928	Ship
Skeg	Skeg starboard	Double-O	216,763	Ship
	Skeg port	Double-O	216,763	
Stabilizer (× 2)	Stabilizer body	----	220,150(× 2)	Ship
	Stabilizer cap	Wrap	109,908 (× 2)	
Shaft (× 2)	Shaft cap	Wrap	55,728 (× 2)	Ship
	Shaft	O	326,671 (× 2)	
	Shaft collar	O	109,908 (× 2)	
	Propeller-shaft gap	O	434,520 (× 2)	
Struts	Inner strut starboard	O	216,673	Ship
	Outer strut starboard	O	216,673	
	Inner strut port	O	216,673	
	Outer strut port	O	216,673	
Propeller (× 2)	Blade pressure side(× 4)	Wrap	109,908 (× 8)	Propeller
	Blade suction side(× 4)	Wrap	109,908 (× 8)	
	Blade tip (× 4)	Double-O	220,320 (× 8)	
Rudder (× 2)	Rudder tip	Wrap	109,908 (× 2)	Rudder
	Rudder top cap	Wrap	217,260 (× 2)	
	Rudder proper	O	162,640 (× 2)	
Wake/propellers' refinement	Propeller refinement starboard	O	1,025,595	Ship
	Propeller refinement port	O	1,025,595	
	Wake refinement	Cartesian	2,132,343	
	Stern refinement	Cartesian	3,221,199	
Bow waves' refinement	Bow ref. level 1 starboard	Curvilinear box	434,520	Ship
	Bow ref. level 1 port	Curvilinear box	434,520	
	Bow ref. level 2 starboard	Curvilinear box	2,438,637	
	Bow ref. level 2 port	Curvilinear box	2,438,637	
	Free surface refinement	Cartesian	3,221,199	Ship (planar DOF's)
	Bkg	Cartesian	3,221,199	Ship (planar DOF's)
Total			31,349,982	

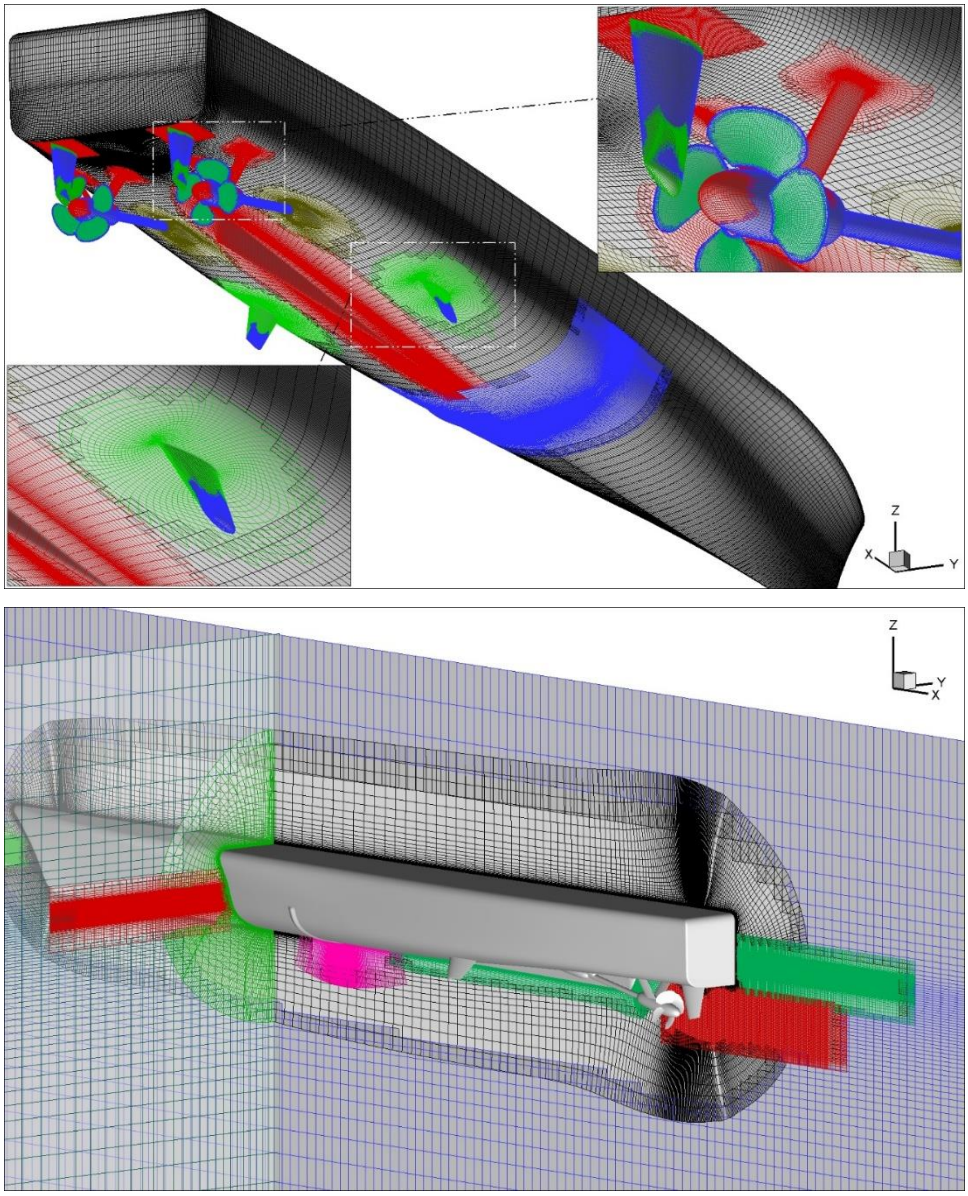

Figure 4.2: The geometry and grid topology for R/V Athena.

4.2.2 Simulation Condition of Ship Case

The simulations are conducted for a fairly strong stratified condition with density profile obtained at the Kitimat Bay (British Columbia, Canada) station as presented in Fig. 4.3. The position of this station is shown in Fig. 4.4. The data includes salinity, temperature

and depth, and corresponds to a seasonal average based on weekly measurements during the summer in July 2007 (Fissel *et al.*, 2010).

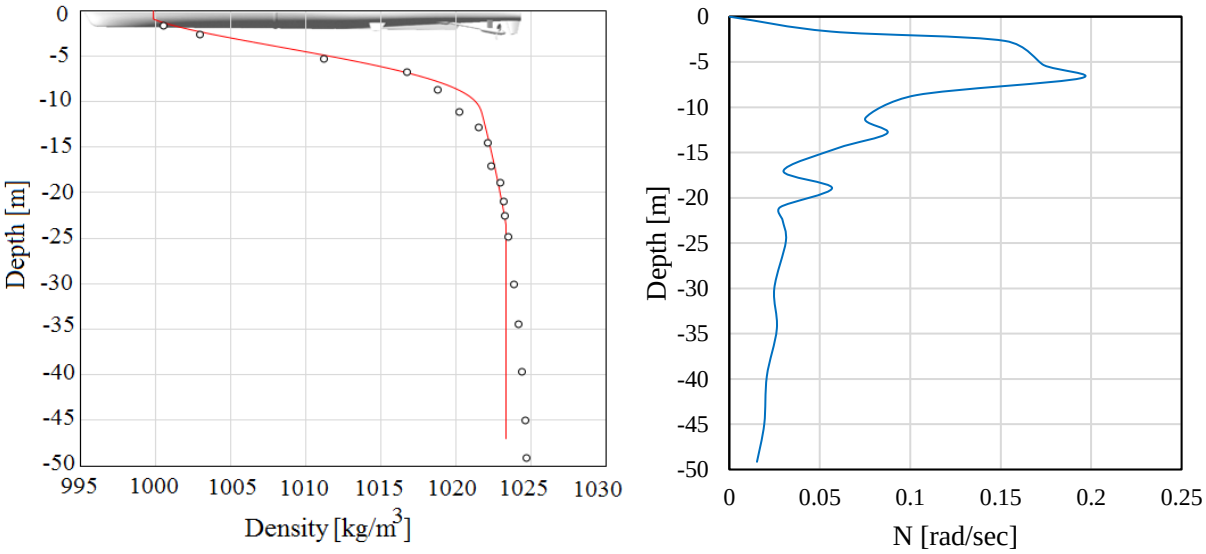

Figure 4.3: The density (left) and buoyancy frequency (right) profiles from Kitimat Bay station.

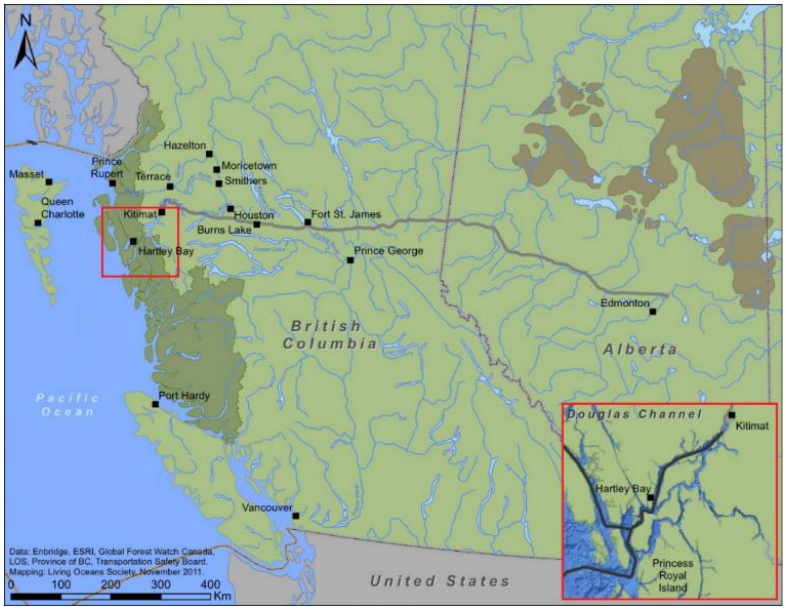

Figure 4.4: Location of Kitimat Bay station, BC, Canada.

An analytical profile is adjusted to the data, with emphasis on capturing the appropriate density gradient in the region of operation of the vessel. A thin layer of constant density is used at the top to prevent unrealistically low values due to extrapolation. A stronger than measured pycnocline is considered. Also, a uniform density far from the vessel is adopted to improve numerical performance at the boundary condition. Neither of these two changes is expected to affect the solution of the near wake. Finally, this non-dimensional density profile is imposed as initial and inlet boundary conditions in the computational domain.

The self-propulsion simulation was conducted using a speed controller (Carrica *et al.*, 2010) to achieve $U_s = 10.5\ knots$, and the grid spacing on solid boundaries is designed to handle boundary layers corresponding to $Fr = 0.252$ and $Re = 2.53 \times 10^8$. Computations were performed at full scale using wall functions. The no-slip boundary condition with wall grid spacing $y^+ \leq 30$ required by turbulence model is used for solid surfaces. This wall grid spacing is calculated based on the Reynolds number, Re, and reference length, L_0, as:

$$\frac{\Delta y}{L_0} = \frac{5.5 y^+}{Re^{0.9}} \tag{4.1}$$

The simulation is performed using fully appended geometry including rotating discretized propellers, and a very small time step of about $\Delta t = 0.0003$ is required to properly resolve the flow. According to the definition of bulk Richardson number in Eq. (3.6) and using the information about R/V Athena in Table 4.1, the bulk Richardson number is calculated and it is set to $Ri = 0.38$ based on reference ship length of $L_0 = 47\ m$ and reference velocity of $U_0 = 10.5\ knot$ for the case of stratified flow. Also, since it is assumed that the simulation is performed for ocean water, the fluid Prandtl number is set into $Pr = 1$,

and turbulent Prandtl number is set into $Pr_t = 0.9$. As the turbulence model, delayed detached eddy simulation (DDES) is chosen for all computations. The far-field boundary conditions set into the background grid includes the inlet condition with zero velocity and imposed density profile, outlet condition with zero second derivative for velocity and zero gradient for other variables, and also zero gradient for all variables at the other four boundaries. Fourth and second order hybrid method are chosen for the momentum and level-set equations, respectively, and the convergence tolerance is set to 10^{-5} for both equations. To solve the density transport equation, a second order implicit Euler method for time discretization, second-order upwind for convection term and second-order-centered scheme for diffusion term are chosen and the convergence tolerance of the density field is set to 10^{-5}. Density transport is also solved as a passive scalar for non-stratified cases by setting the Richardson number to zero, making the momentum equation independent from the density transport equation.

4.2.3 Result and Discussion for Ship Case

As a ship advances through a stable stratified background it disturbs the flow due to stirring and displacement, creating unstable features that propagate downstream. The wavelength of the internal waves that is generated is much longer than the ship length, suggesting that the near-ship field and the far-field stratified flows can be computed separately, with the more expensive near-field simulation limited to about one ship length and the far-field using the exit of the near-field as inlet condition. Performing a fully resolved simulation of the near- and far-fields together would be extremely expensive due to the large size of the required domain, and the vastly different time steps needed to model

the rotating propeller, the fastest process in place, and the slow advance of the internal waves. The coupling of the near- and far-field stratified flow solvers is a subject of future research and is not discussed in this chapter.

The resulting density distribution at the center plane of the ship, $y/L_0 = 0$, and at the propeller plane, $y/L_0 = 0.04$, (approximately the propeller shaft axis location) for both stratified and non-stratified flows are presented in Fig. 4.5. This figure clearly shows the different layers of stratification resulting from the interaction of the stable stratified background with the self-propelled advancing ship. Moreover, it is observed that the density disturbances on the near wake are related to separation at the wet transom and propeller mixing, and to a less extent to the free surface wave system caused by the ship.

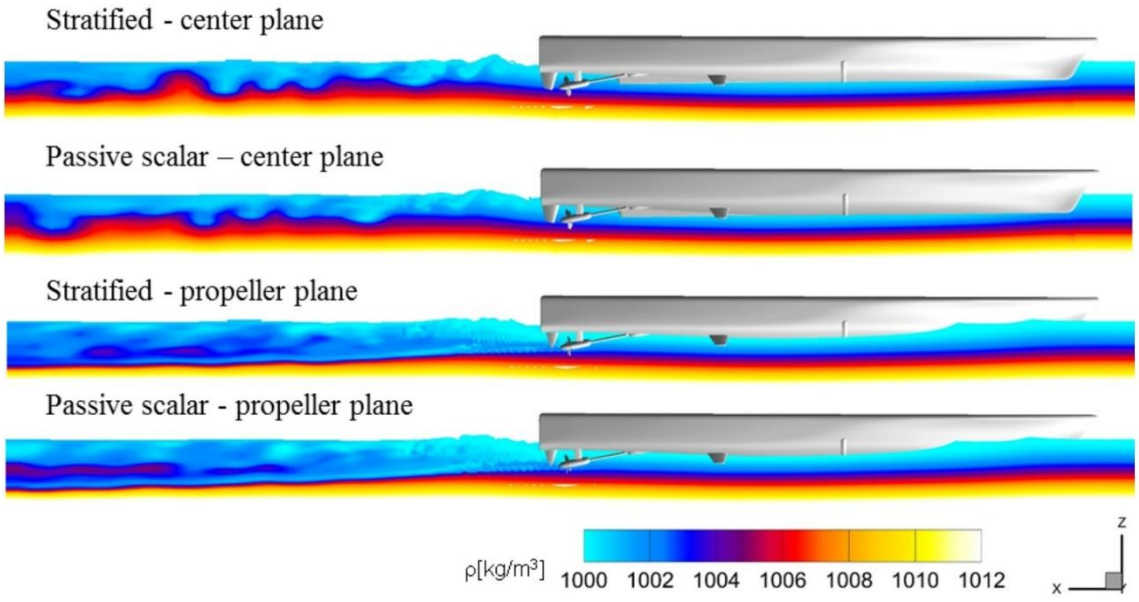

Figure 4.5: Density distribution at center plane ($y/L_0 = 0$; top) and at propeller plane ($y/L_0 = 0.04$; bottom). Stratified vs. passive scalar fields are shown for both locations.

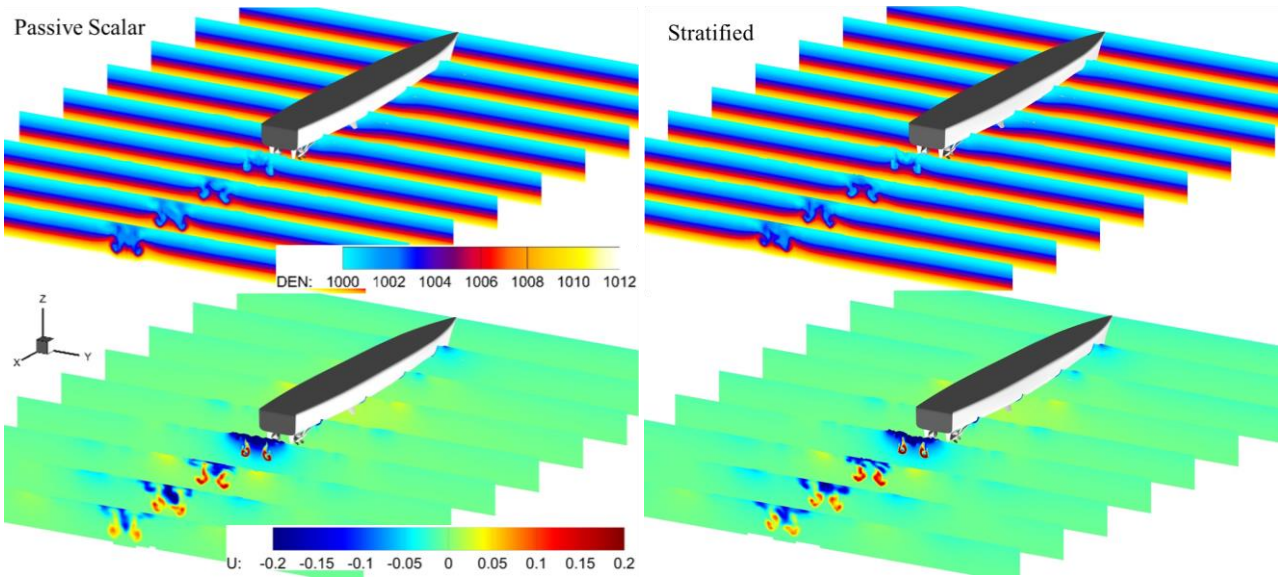

Figure 4.6: Axial cross sections showing density variations at different *x* locations (top), and longitudinal velocities (bottom) for the self-propelled case of passive scalar transport and stratified conditions.

The downstream evolution of the wake can be also appreciated in Figs. 4.6, which shows several longitudinal cross sectional planes colored with density and the free surface colored with axial velocity. For comparison, the transport of a passive scalar with the same inlet distribution as the background density is also shown in Fig. 4.6. While details of the instantaneous flow differ, it is found that for the simulated conditions and for the near wake, stratification effects are not dominant over inertial effects. As the wake velocity decays, most evident in the furthest downstream cross section in Fig. 4.6 at approximately one ship length from the stern, the strong stirring signature from the propellers that pushes light fluid down and pulls heavy fluid up, and from the stern that pulls heavier fluid closer to the free surface, is preserved. The stratification volume forces tend to maintain the wake defect higher near the surface than in the non-stratified case with the passive scalar, and similarly a stronger propeller wake.

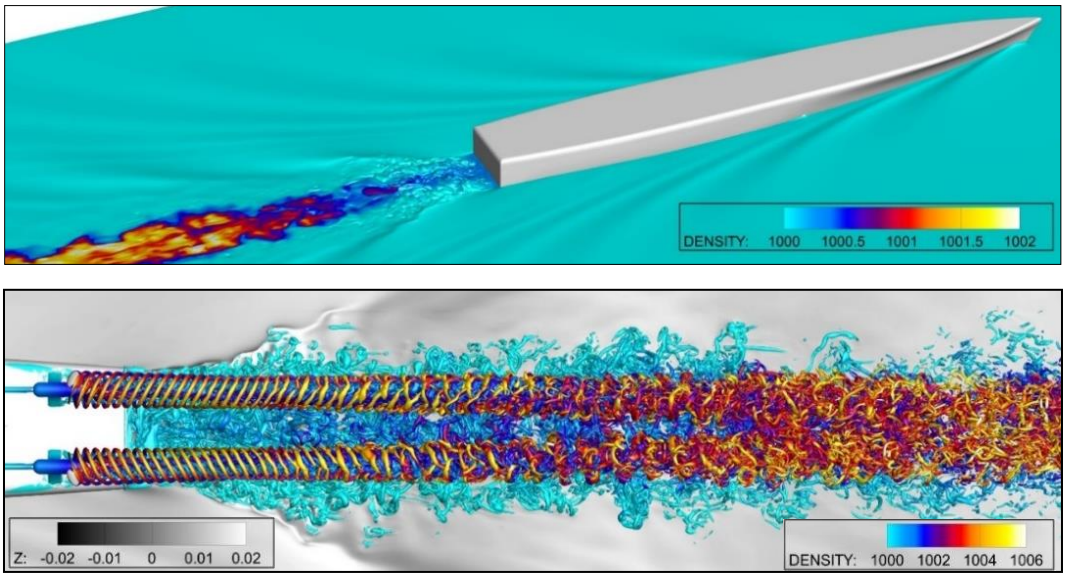

Figure 4.7: Instantaneous surface density distribution in the wake of self-propelled R/V Athena at 10.5 *knots* ($Fr = 0.25$).

Figure 4.7 shows R/V Athena advancing in a stratified condition, with the vortical structures represented by the isosurface $Q = 500$ of the second invariant of the velocity gradient tensor colored by non-dimensionless density and the free surface colored by axial velocity. The second invariant of the velocity gradient tensor is defined as:

$$Q = \frac{1}{2}\left(\Omega_{ij}\Omega_{ij} - \mathrm{S}_{ij}\mathrm{S}_{ij}\right) \tag{4.2}$$

where,

$$\Omega_{ij} = \frac{1}{2}\left(\frac{\partial u_i}{\partial x_j} - \frac{\partial u_j}{\partial x_i}\right) \quad , \quad \mathrm{S}_{ij} = \frac{1}{2}\left(\frac{\partial u_i}{\partial x_j} + \frac{\partial u_j}{\partial x_i}\right) \tag{4.3}$$

Notice the compression of the density isolines between the mixed region cause by the propeller action and the undisturbed background, as well as the slow pulsing of the region between the two propeller wakes under the action of surface wave originating in the ship's

transom. It should be noticed that self-propelled at 10.5 $knots$ the ship's wake is not momentumless due to wave-making resistance, resulting in net positive momentum of approximately 10% of the thrust in model scale in barehull condition (Jenkins, 1984).

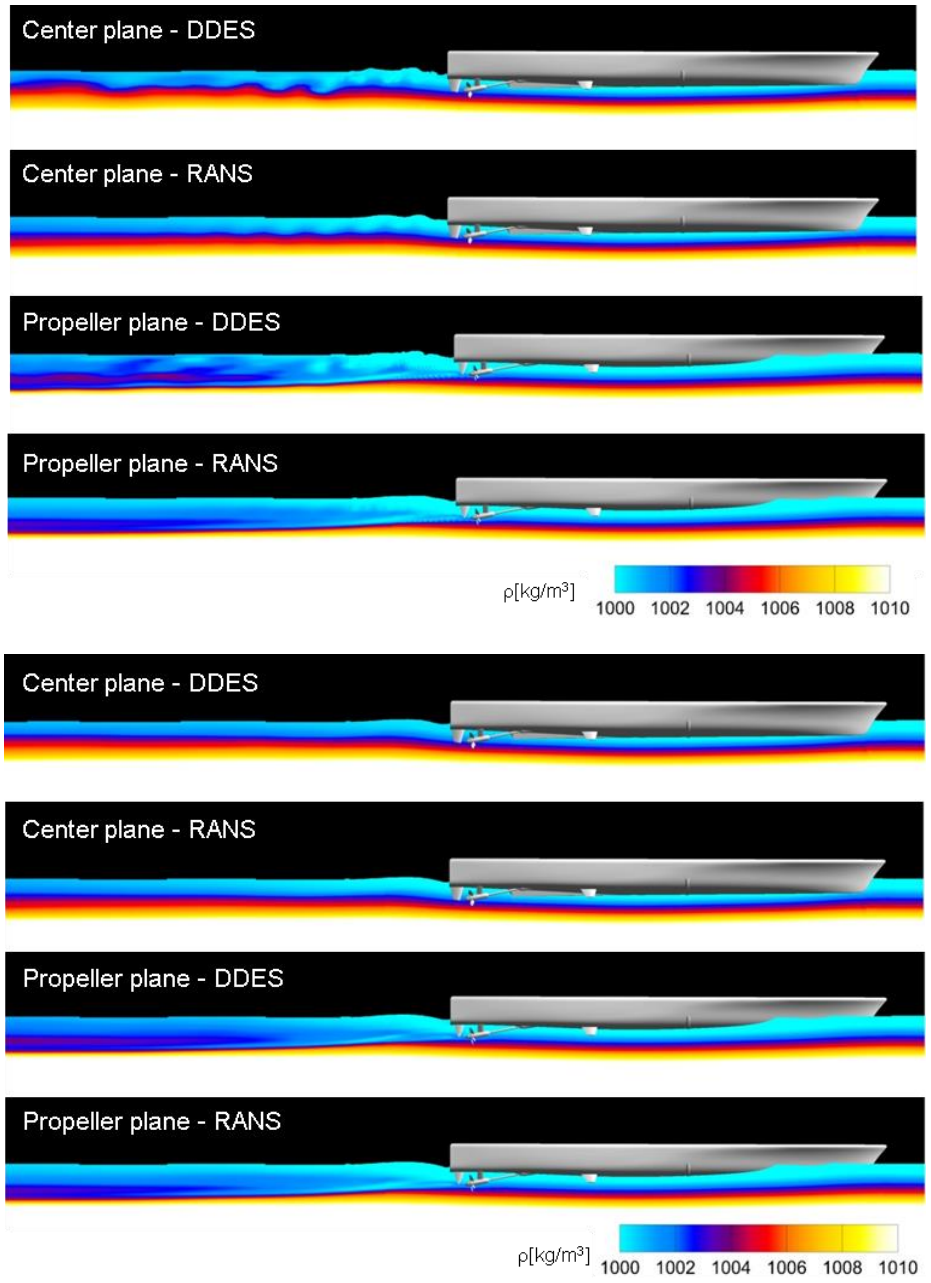

Figure 4.8: Instantaneous (top) and mean (bottom) density distributions at the center plane ($y/L_0 = 0$) and at the starboard propeller plane ($y/L_0 = 0.04$). Turbulence model used indicated in each panel.

Figure 4.8 shows both Instantaneous and mean density distributions at the center plane ($y/L_0 = 0$) and at the starboard propeller plane ($y/L_0 = 0.04$) using DDES and RANS approaches. Both instantaneous and average results are shown for both turbulent models; as expected, flow structures are better captured by the DDES approach. Differences in the mean are only important in the wake, away from solid surfaces, and are related to a lower prediction of mixing by RANS modeling. The downstream evolution of the wake can be also appreciated in Fig. 4.9, which shows several longitudinal cross sectional planes colored with density and the free surface colored with axial velocity. Figure 4.10 shows the resolved and modeled TKE for the same planes as in Fig. 4.9. For comparison, the transport of a passive scalar with the same inlet distribution as the background density is also shown in Figs. 4.9 and 4.10. Notice that the resolved TKE is computed using point averages for all times, and not a phase-averaged calculation with the propeller blade position, which would require very long statistics not available from the simulations. This results in reliable TKE results in the transom wake but results closer to the mean square of the fluctuations in the wake of the propellers. While details of the instantaneous flow differ, it is found that for the simulated conditions and for the near wake, stratification effects are small compared to inertial effects. As the wake velocity decays, most evident in the furthest downstream cross section in Fig. 4.9 at approximately one ship length from the stern, the propeller stirs the stratified flow which results in pulling heavy fluid up and pushing light fluid down, and due to favorable pressure gradient the ship stern pulls heavier fluid closer to the free surface. The stratification volume forces tend to maintain the wake defect higher near the surface than in the non-stratified case with the passive scalar, and similarly a stronger propeller

wake. At this plane, modeled TKE is weaker for the non-stratified case in the region immediately above the propeller wake, suggesting that the unstable stratification in that region is at this distance strong enough to have an effect as a sink of TKE.

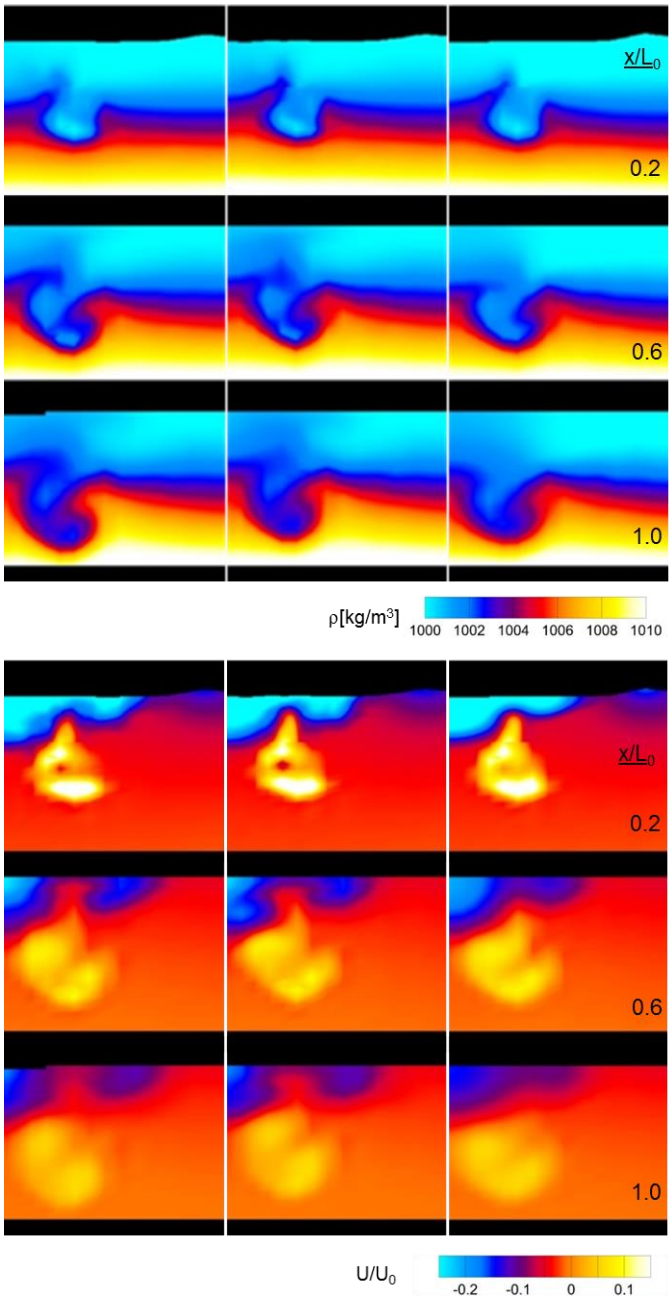

Figure 4.9: Axial cross sections for the self-propelled R/V Athena at different axial cross sections downstream of the stern of the ship (only starboard side shown). Mean density (top) and mean longitudinal velocity (bottom) are shown. Passive scalar transport with DDES (left), stratified conditions with DDES (center) and stratified conditions using RANS (right).

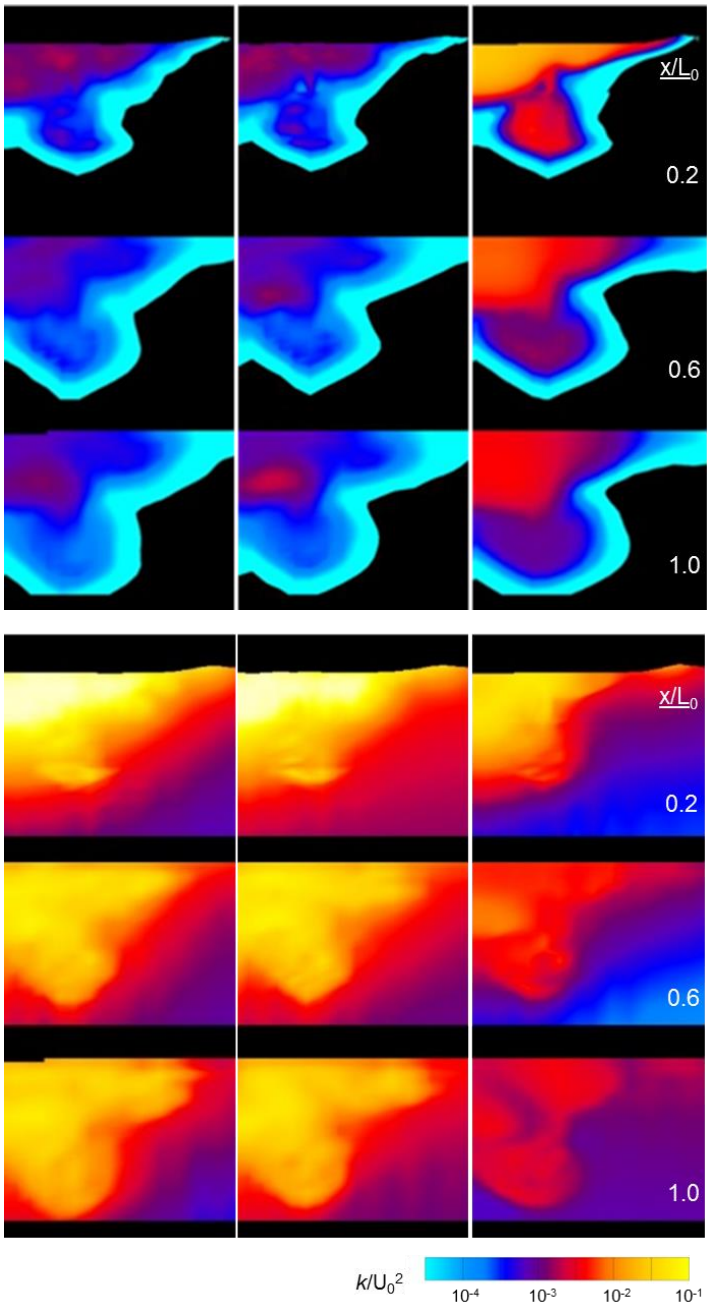

Figure 4.10: Axial cross sections for the self-propelled R/V Athena at different axial cross sections downstream of the stern of the ship (only starboard side shown). Mean modeled (top) and resolved (bottom) turbulent kinetic energy are shown. Passive scalar transport with DDES (left), stratified conditions with DDES (center) and stratified conditions using RANS (right).

4.3 Near-Field Stratified Flow for a Submarine

Computation and experimental fluid dynamic tools have been used to predict the hydrodynamic forces on different submarine geometries, such as the DARPA SUBOFF submarine (AFF-1 and AFF-8) and the Joubert BB1 and BB2 submarines (Bellevre *et al*., 2000; Toxopeus, 2008; Bettle *et al*., 2009; Phillips *et al*., 2010; Kumar *et al*., 2012; Chase and Carrica, 2013; Bettle *et al*., 2014; Ashok *et al*., 2015). In all these studies the near-field wake structure was investigated for different conditions such as self-propelled, maneuvering and zig-zag motions and force and moment were calculated successfully. In all these works, the underwater vehicles were simulated in a non-stratified medium with constant density and the effects of stratification were ignored. However, in real life the underwater vehicles move in a stratified medium which might modify the performance characteristics determined by the hydrodynamic loads on the vehicle significantly. As it is mentioned in Chapter 3, the reflection of acoustical signals of search sonars by the pycnocline surface in the stratified medium is a good reason for underwater vessels to operate in the vicinity of this region. Therefore, in this section, the numerical simulation of a submarine advancing in a stratified flow is presented in detail. As the submarine geometry, the Joubert BB2 is chosen to simulate the near-field flow. Operation near the surface is considered, and both internal and surface waves generated are investigated. A theoretical two-layer stratification is used; a hyperbolic tangent is used to produce analytically a thin transition zone between the layers. Two stratification conditions are considered, one with the pycnocline located at the propeller centerline, and the second with the pycnocline located below the submarine. The submarine geometry corresponds to the Joubert BB2 model hull form with overall full scale length of $L_0 = 70.2m$, which is a modified version of the original Joubert geometry

BB1 designed by the Defense Science and Technology Organization (DSTO) in Australia (Anderson *et al*., 2012). BB2 was designed by the Maritime Research Institute Netherlands (MARIN) with larger aft control surfaces and a thicker sail (NACA0022 section) that is moved slightly forward. Comparing to BB1 model, the deck and hull of BB2 were unchanged. The views of the fully appended submarine model including the sail, rudders and propeller are shown in Fig. 4.11, with main particulars listed in Table 4.3. The submarine has a 6-bladed propeller for the propulsion system and the main characteristics of the propeller are presented in Table 4.4.

Table 4.3: Main particulars of Joubert BB2.

Length overall submerged	70.2 m
Beam	9.6 m
Depth (to deck)	10.6 m
Depth (to top of sail)	16.2 m

Table 4.4: Main particulars of the Joubert BB2 propeller, MARIN stock propeller 7371R.

Number of blades	6
Propeller diameter	5.0 m
Hub diameter	1.114 m
Hub/diameter ratio	0.223
Pitch/diameter at 0.7R	0.966
Pitch at 0.7R	94.83 m
Expanded blade area ratio	0.7

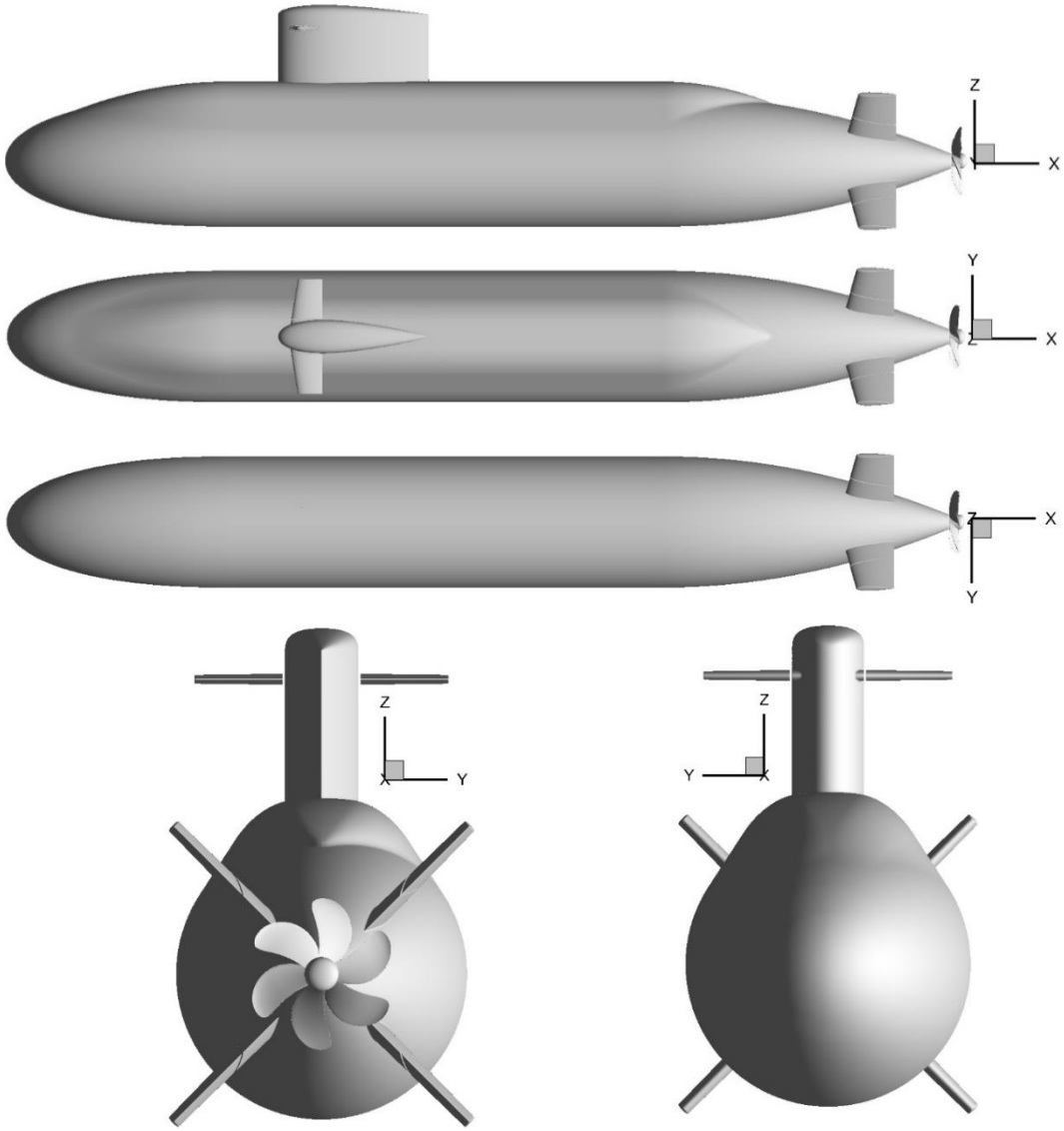

Figure 4.11: Joubert BB2 geometry and coordinate system.

4.3.1 Grid Design of Joubert BB2

The overset grid topology of the Joubert BB2 at the solid surfaces and cross-sections detailing the refinement and the propeller/rudder refinements are presented in Fig. 4.12. The overset grid system includes the hull, sail, propeller, stern planes, sail planes, refinements and domain background with 44.7 M or 48.7M grid points, depending on the refinements used, distributed into up to 470 processors for the largest case. All these 15 blocks with the

hierarchy of bodies used to run the simulation are distributed in 470 processors and listed in Table 4.5.

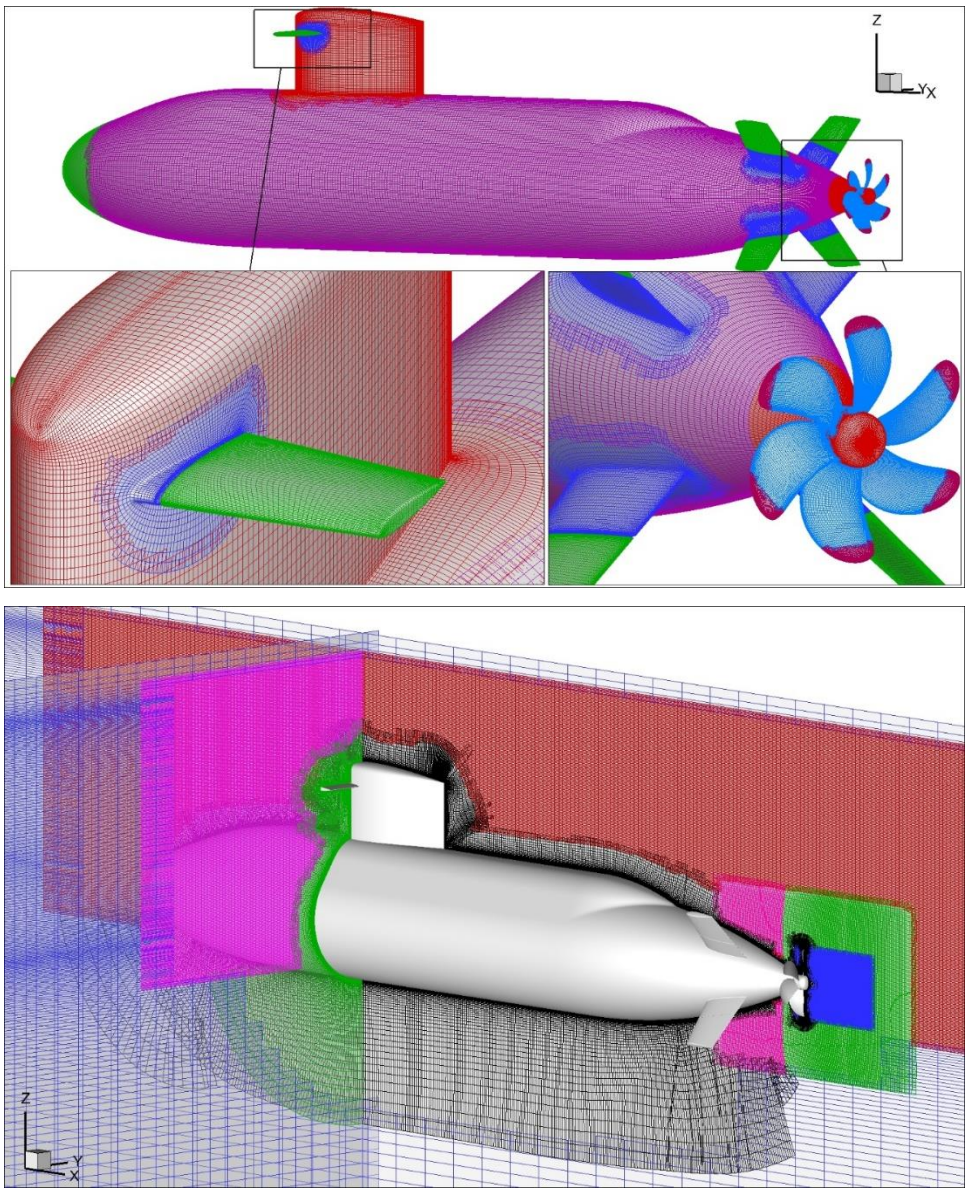

Figure 4.12: Joubert BB2 overset grid system topology.

Table 4.5: Grid dimensions for Joubert BB2 submarine.

Grid	Type	Total Points	Moves with
Hull	O	6,409,170	Submarine
Nose	Wrap	216,763	Submarine
Sail	Wrap	860,946	Submarine
Sail Planes Roots	Wrap	433,698	Submarine
Stern Planes Roots	Wrap	1,727,568	Submarine
Sail Planes	O	863,784	Submarine
Stern Planes	O	3,438,936	Submarine
Propeller Hub	O	430,473	Propeller
Propeller Blades	O	2,582,838	Propeller
Blade Tips	Wrap	1,300,578	Propeller
Refinement ($z_0/L_0 = -0.25$)	Cartesian	16,381,521	Submarine
Refinement ($z_0/L_0 = -0.33$)		20,340,801	
Refinement Stern Planes	Cartesian	3,778,377	Submarine
Refinement Propeller	Cartesian	3,778,377	Submarine
Background	Cartesian	2,528,835	Submarine (planar DOF's)
Total ($z_0/L_0 = -0.25$)		44,731,864	
Total $z_0/L_0 = -0.33$)		48,691,144	

Similarly to the R/V Athena case, all appendages are handled using overset grids. The grids have a collar surface grid that conforms to the hull, and other surface grids that conform to the appendage itself. From these surface grids volume grids are generated using hyperbolic solvers provided by the commercial grid generation software Gridgen. The hull grid consists of an O-type grid spaced to capture the strong gradients in the boundary layer. The overlapping appendage grids are intended to provide a fine computational mesh for the wake. A Cartesian background grid is considered as the background grid to impose far-field boundaries. Depending on the position of the interface of the two-layer fluid, a Cartesian refinement grid is used to better capture the wake of the submarine and internal waves of stratified flow. The domain connectivity needed to perform overset computations is obtained at run time using the code Suggar (Noack, 2005) while surface overlap is pre-

processed using USURP (Boger and Dreyer, 2006) to obtain the information of overset surface panels for force integration.

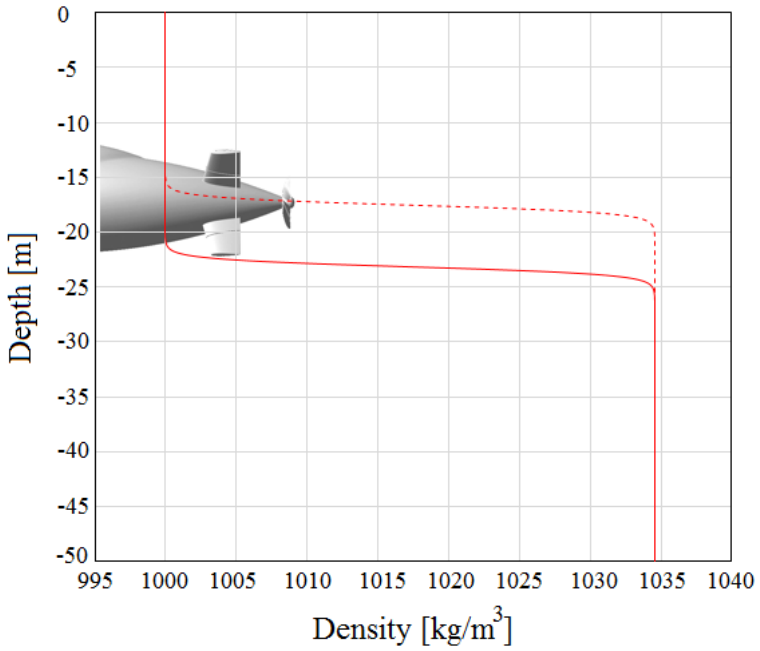

Figure 4.13: Density profile used for submarine simulations. Dashed line has maximum gradient at $z_0/L_0 = -0.25$, approximately the propeller centerline; solid line has maximum gradient at $z_0/L_0 = -0.33$, slightly below the submarine fins.

4.3.2 Simulation Condition of Submarine Case

For the Joubert BB2 with fully appended geometry including rotating discretized propellers, simulations are conducted using a two-layer stratification represented by a hyperbolic tangent density distribution (see Fig. 4.13). The density values corresponding to top and bottom layers are characterized as $\rho_1 = 1000\, kg/m^3$ and $\rho_2 = 1034\, kg/m^3$, respectively, while the interface between two layers is considered thin (see Fig. 4.13). The midpoint of the profile, for which the gradient is maximum occurs at $z_0/L_0 = -0.25$ (dashed line in Fig. 4.13), approximately the propeller centerline or at $z_0/L_0 = -0.33$ (solid line), slightly below the submarine fins. For each stratification condition, the non-dimensional

density profile and hydrostatic pressure distribution are imposed as initial and inlet boundary conditions using an input file into the code. In addition to the stratification cases, a complementary simulation for the latter case considering the density distribution as a passive scalar is also performed as the non-stratification case. The bulk Richardson number based on the boat length and density distribution is set into $Ri = 0.9$ for both stratified conditions; corresponding values based on depth are 0.225 and 0.297, respectively. Self-propulsion simulations with discretized propeller at full scale are conducted in calm water to achieve a speed of 10 $knots$, corresponding to $Fr = 0.195$ and $Re = 3.6 \times 10^8$. The depth is set at $0.25\, L_0$, so that the propeller shaft is located 17.55 m below the undisturbed free surface. Motions of the vessel are restricted on all directions except surge. This simplification is adopted to isolate the effect of propulsion on the stratified fluid. However, it is a good practice to simulate a full six-degree-of-freedom (6DoF) to find the effect of stratification in steady roll angle and pitch, though the final attitude at self-propulsion in experiments shows very small pitching angle and stern plane deflection (Overpelt, 2015). Self-propulsion is achieved after approximately 140 sec with a time step of 4.1 ms (about 34,000 time steps); simulations were then run for a few additional ship lengths at self-propulsion to obtain averaged quantities. The turbulence was modeled for all cases using DDES; a posteriori check of the dimensionless wall distance shows that at self-propulsion the average distance is y^+=50, with a standard deviation of 27.6. About 10% of the active surface points are below the recommended range of 30-300 for the application of the model; these points occur in areas of particularly low shear on the hull, near the propeller, where the friction forces are very small.

As the self-propulsion condition, the far-field boundary conditions set into the background grid includes the inlet condition with zero velocity and imposed density profile, outlet condition with zero second derivative for velocity and zero gradient for other variables, and also zero gradient for all variables at the other four boundaries. The delayed detached eddy simulation (DDES) is chosen as the turbulence model for all computations, and fluid Prandtl number and turbulent Prandtl number are set into $Pr = 1$ and $Pr_t = 0.9$, respectively. The time step is set into $\Delta t = 0.0003$ to properly resolve the fluid flow around the propeller throughout the whole computation domain and obtain accurate numerical solutions of both stratified and non-stratified conditions. Fourth and second order hybrid method are chosen for the momentum and level-set equations respectively, and the convergence tolerance is set into 10^{-5} for both equations. To solve the density transport equation, second order implicit Euler method for time discretization, second-order upwind for convection term and second-order-centered scheme for diffusion term are chosen and the convergence tolerance of the density field is set into 10^{-5}. For the non-stratified conditions, the density distribution is solved independently from momentum equation as a passive scalar by setting the bulk Richardson number to zero while the same density distribution is used for the computational domain.

4.3.3 Result and Discussion for Submarine Case

Figures 4.14 and 4.15 show results for the different self-propulsion cases simulated. In Figure 4.14 the two stratified cases considered are shown. The distortion of the density profile as result of the direct mixing and stirring due to the propeller action is evident on the case with the pycnocline situated at the propeller centerline. In the second case, changes to

the density profile occur indirectly, as fluid acceleration near the submarine creates an internal wave at the interface. No appreciable difference is observed on the free surface waves for either case, which are mainly the response to the submarine's pressure field as it sails near the surface. Variations on the vortical structure of the propeller and submarine's stern planes are better observed in Fig. 4.15. Vortices evolving near the pycnocline are noticeably modified by its presence, most notably the propeller's tip vortices in the case $z_0/L_0 = -0.25$, and the lower stern planes' tip vortices for $z_0/L_0 = -0.33$. Vortices away from regions with varying density resemble those for the passive scalar case (propeller tip vortices for $z_0/L_0 = -0.33$; upper stern planes' tip vortices).

The generation of an internal wave can be observed in Fig. 4.15. For the reference, non-stratified case, the only effect observed is the deformation of the interface as the propeller wake diffuses and increases in size, but such deformation has no effect on the dynamics of the interface that can only be transported by the flow as a passive scalar. For the other two cases, the presence of the submarine generates a standing internal wave, similar to those observed for the sphere case shown in Chapter 3. It is interesting to note that the internal wave amplitude is much larger when the interface does not interact directly with the body. The two main reasons for this behavior are (i) a reduction in stirring as the propeller does not interact with the interface, but more importantly (ii) the lack of a vertical acceleration of the fluid in the region between the submarine and the interface; instead only lateral perturbations to the interface are present when the submarine operates at the interface.

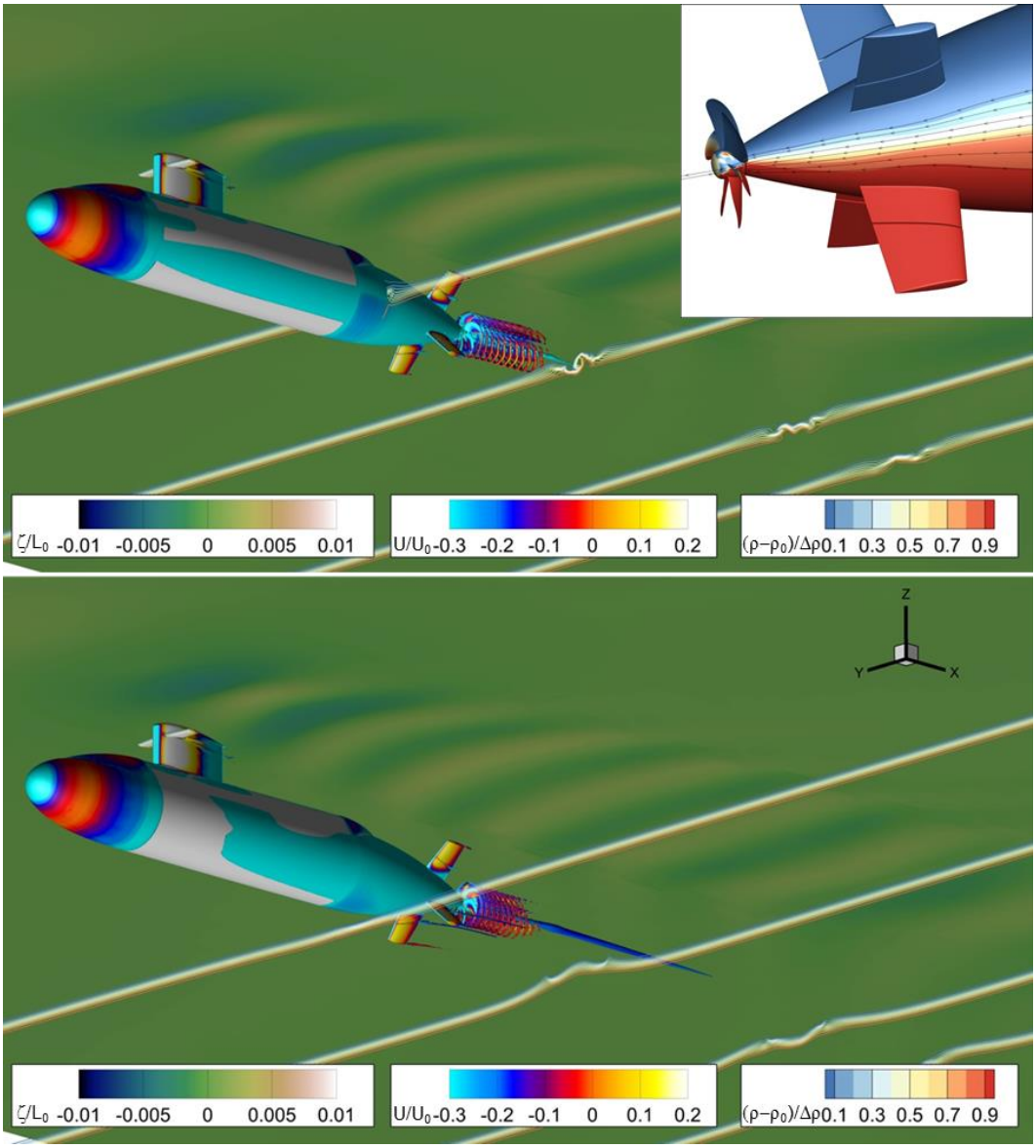

Figure 4.14: Joubert BB2 Self-propelled. Top: pycnocline at propeller centerline; bottom pycnocline below submarine. Free surface elevation, isosurface of $Q = 500$, colored with longitudinal velocity and density at different *x*-planes are shown.

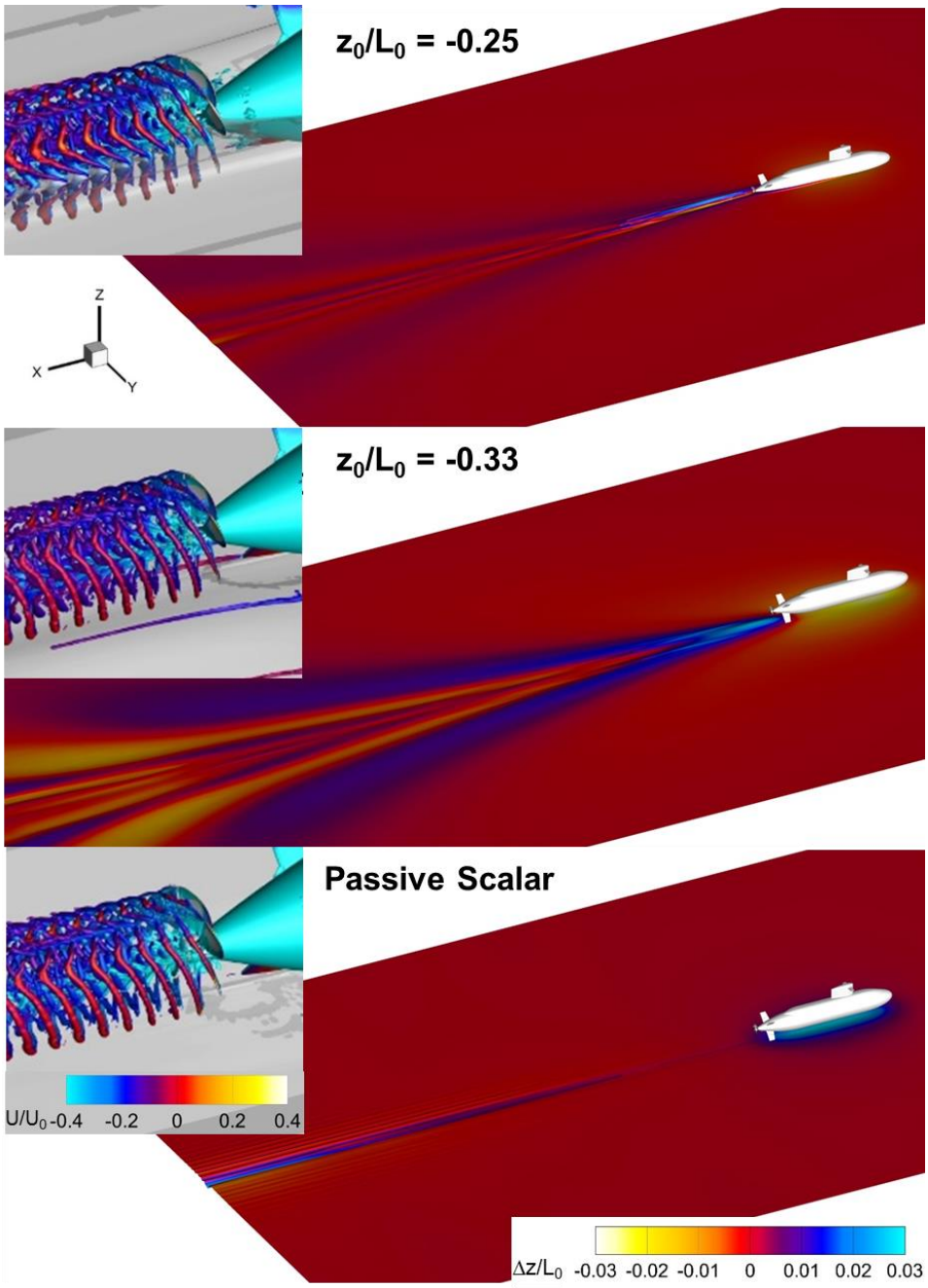

Figure 4.15: Self-propelled Joubert BB2. Isosurfaces for $\rho = \rho_0 + \Delta\rho/2$ are shown for the three cases considered (top: pycnocline at propeller centerline; middle: pycnocline below submarine; bottom: as previous but for passive scalar). Elevation difference with respect to background is shown. Details of isosurface of $Q = 500$ near the propeller are shown as inserts.

The celerity of a two-layered, deep internal wave is related to the celerity of surface wave by $C_i/C_s = \sqrt{\Delta\rho/(\rho_1 + \rho_2)}$, so the traditional Froude number for an internal wave is $Fr_i = Fr\sqrt{(\rho_1 + \rho_2)/\Delta\rho} \cong \sqrt{2}\, Fi$. This relation is not valid for more complex situations, like the case of R/V Athena in a littoral stratification with a complex profile, but can be used for the case of Joubert, where a two-layered stratification is used. For the conditions of the paper, $Fr_i \cong 1.5$, which can in principle be used to estimate the internal wave wavelength, which in this case is $\lambda_i \cong 14\, L_0$, and compares with a free surface wavelength $\lambda \cong 0.24\, L_0$. That is consistent with what is shown in Figs. 4.14 and 4.15, where one wavelength of the internal wave cannot be captured by the length of the domain, but the surface wave is resolved well.

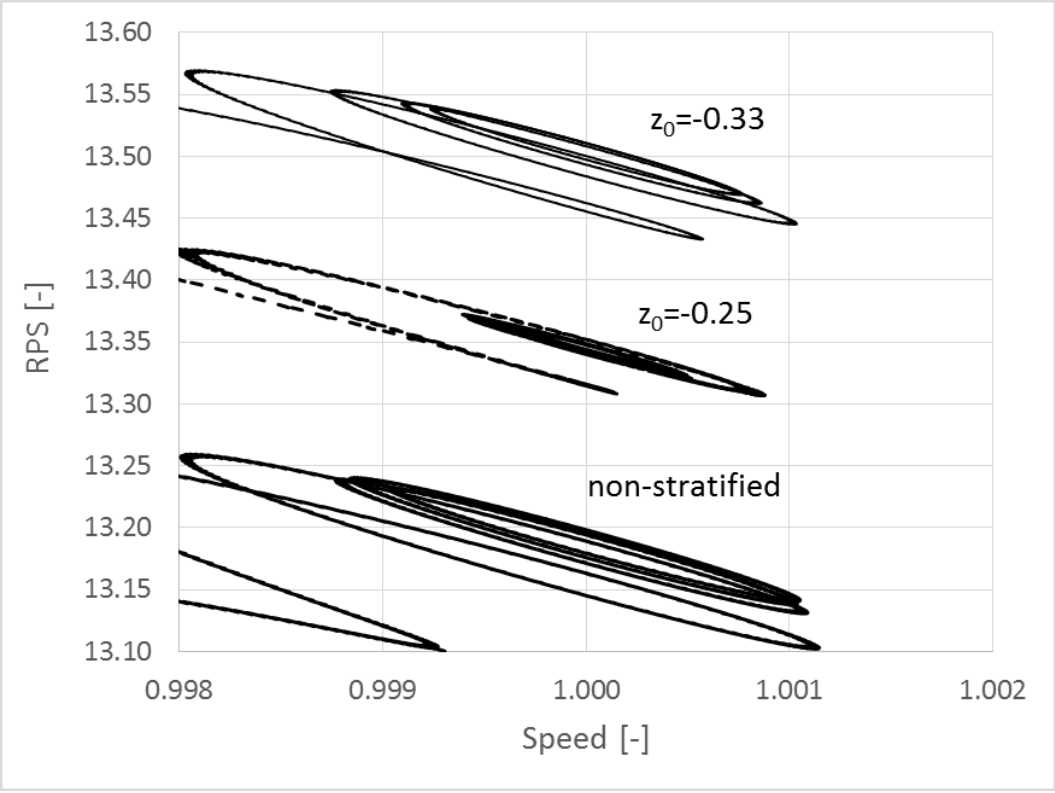

Figure 4.16: Trajectories in the dimensionless speed-RPS space for all cases of the self-propelled submarine Joubert BB2. As the speed controller converges to the target unit dimensionless speed the dimensionless RPS converges to its self-propulsion value.

Figure 4.16 displays trajectories in the dimensionless speed-RPS space, showing the convergence of the speed controller as the propeller rotational speed is changed as the target speed is reached. The case with the pycnocline located at $z_0/L_0 = -0.33$ requires the highest RPS, and thus is subject to more resistance, while the case with no stratification has the lowest resistance.

4.4 Propulsion and Energy Consideration

The presence of a stratified background can affect the energy balance for a self-propelled vessel. Just as increased output from the propeller is needed to overcome the surface waves generated by a moving ship, any internal wave generated due to the presence of stratification incurs an energetic deficit in the ship system. The energy changes are however small, and can be masked by other changes in the ship configuration (such as change in draft and attitude) that are also a result of the presence of the stratified fluid. In this section a potential energy budget is proposed and results for the cases presented previously are discussed.

The potential energy available to generate internal waves is of interest. The rate of change of total potential energy can be computed as (Winters *et al*., 1995; Tseng and Ferziger, 2001):

$$\frac{dE_{tot}}{dt} = -\oint_S \rho(\boldsymbol{x},t) gz\boldsymbol{u}.\hat{\boldsymbol{n}}\, ds + \int_V \rho(\boldsymbol{x},t) wg dV + \oint_S \alpha gz\boldsymbol{\nabla}\rho.\hat{\boldsymbol{n}}\, ds - \oint_A \alpha g\left(\rho_{top} - \rho_{bottom}\right) dA \tag{4.4}$$

where z is the vertical spatial coordinate (positive upward). The first term on the right-hand side of Eq. (4.4) represents the change in potential energy due to the advective fluxes across the boundaries of the domain, the second term relates to exchange between potential and

kinematic energy via buoyancy flux, the third term shows the change due to the diffusive mass flux through the boundaries of the domain, and the last term represents the change in potential energy based on diapycnal mixing in the fluid domain. These last two terms are small for the near-field and will be neglected. The potential energy leaving the exit plane of the computational domain per unit time is then the potential energy available to generate internal waves, though part of this energy will be spent on turbulent and diffusive mixing.

Equation (4.4) has the problem of including the free surface energy, which in the case of surface ships is typically much higher than the energy due to deviation from stable stratification. The energy leaving the exit plane per unit time, due only to deviation from stable stratification can alternatively be evaluated as follows:

$$P_{av} = \oint_A [\rho - \rho(z)][z - z(\rho)] g \boldsymbol{u}.\hat{\boldsymbol{n}}\, dA = \oint_A I_x\, dA \tag{4.5}$$

where the integrand explicitly evaluates the work needed to translate a particle of density ρ with excess density $\rho - \rho(z)$ from its current depth z respect to the free surface to its stable depth $-z(\rho)$. $\rho(z)$ is the stable equilibrium density stratification given in Fig. 4.13, and $z(\rho)$ is the depth at which a fluid particle of density ρ is found in stable stratification, or essentially the inverse of the density distribution shown in Fig. 4.13. In Eq. (4.5) I_x is the potential power flux crossing the plane due to deviations from stable stratification, referred here as potential power flux.

The proposed method was applied to self-propulsion results for R/V Athena. The total potential energy per unit time available for generation of internal waves, computed with Eq. (4.5), is estimated to be $2\,kW$. Though this is a small fraction of the effective power, the small density difference on the stratified layers means that significant internal waves can still be produced. Note that part of this energy will be dissipated on turbulent

density mixing. Calculations for R/V Athena have the disadvantage of containing several competing processes affecting the outcome for a propulsion analysis, including uncertainty in the separation of potential energy from the internal and the surface wave, and different draft and attitude for the vessel for different density distributions. A further difficulty in assessing the effect of stratification on propulsion for this case is that the propellers operate at higher density (approximate $1005\ kg/m^3$, as shown in Fig. 4.3) than the density of the fluid surrounding the hull which can improve propeller thrust, simply due to the increase of density, while any buoyant effects such as reduction of vertical mixing are negligible given the dominant effect of the propeller motion. Given that all these complexities, a complete energy budget study was not performed.

Table 4.6: Comparison of Joubert BB2 performance in uniform and stratified flows at 10 *knots*.

Parameter	Stratified		Constant density
	$\frac{z_0}{L_0} = -0.25$	$\frac{z_0}{L_0} = -0.33$	
Effective power (kW)	443.5	469.0	434.8
Propeller rotational speed (RPS)	0.978	0.99	0.966
Torque (kN-m)	80.3	83.9	78.6
Thrust (kN)	86.2	91.2	84.5
Shaft power (kW)	493.6	521.3	477.6
Advance velocity (m/s), thrust id. method	3.52	3.52	3.48
Propeller efficiency (%), thrust id. method	61.6	61.5	61.5
Power available to potential energy (kW)	8.7	34.2	---
Estimated potential energy flux (Eq. 10, kW)	7.3	33.5	---

Simulations for the Joubert BB2 submarine, on the other hand, by restricting vertical motions of the vessel and using essentially a two layer system, allow for a clear separation of the generation of internal waves from other effects affecting the total resistance of the vessel. Table 4.6 presents results for the two stratified conditions, one with the propeller operating at the pycnocline, the second with the whole submarine above the interface, and

their comparison to unstratified conditions. The corresponding effective power (P_E) of submarine with self-propulsion velocity of U_s and ship total resistance of R_T can be obtained as:

$$P_E = R_T \times U_0 \tag{4.6}$$

The ship total resistance can be expressed as:

$$R_T = \frac{1}{2} C_T \, \rho_0 A_w U_s^2 \tag{4.7}$$

where C_T is the resistance coefficient and A_w is ship wetted area. According to Table 4.6, both cases of stratified flow have more effective power than the non-stratified flow with constant density. Also, comparing the effective power of stratified cases shows that when the submarine moves above the pycnocline, its effective power is about 6% more than the case of the propeller operating at the pycnocline. The same behavior is also observed for the propeller rotational speed. The propeller operating above the pycnocline region needs to move faster to overcome the resistance of friction, waves and eddies and reach the self-propulsion speed. In general, propeller parameters including torque, thrust and efficiency can be calculated by following the equations:

Thrust: $$T = K_T \rho_0 n^2 D^4 \tag{4.8}$$

Torque: $$Q = K_Q \rho_0 n^2 D^5 \tag{4.9}$$

where K_T is the thrust coefficient, K_Q is the torque coefficient, n is the propeller rotational speed, and D is the propeller diameter. Finally, from these variables, a value for propeller efficiency can be obtained as the ratio between the thrust power P_T, which the propeller delivers to the water, and the power P_D, which is delivered to the propeller:

$$\eta = \frac{P_T}{P_D} = \frac{T}{Q}\frac{U_A}{2\pi n} = \frac{K_T}{K_Q}\frac{J}{2\pi} \tag{4.10}$$

where $P_T = TU_A$ is the thrust power and $J = U_A/nD$ represents the advance number of the propeller with U_A the advance velocity. As it is shown in Table 4.6, both thrust and torque increase in the case of stratified flow and as a result and considering Eq. (4.10) the propeller efficiency is approximately the same for both cases. The potential energy flux for both stratified cases is much larger compared to the shaft power than it is for the previous case, and consistent with the increase in total resistance. The potential energy flux is about 5 times larger for the case with a deeper interface, as the initial internal wave setup is larger for that case, and mixing due to direct interaction of the pycnocline with the vessel is negligible. Figures 4.17 and 4.18 illustrates the distribution of I_x in different longitudinal planes for two stratification conditions. The thrust identity method (ITTC, 1978) was used to obtain the advanced velocity and the propeller efficiency, based on the values for thrust from the simulation and the open water curve characteristics for propeller 7371R (Overpelt, 2015). The propeller efficiency is essentially unchanged with differences of about 0.1% across the different cases, while power varies as much as 8%. The lack of strong dependence of propeller efficiency on stratified conditions, supports the assumption that the stratification is too weak compared to the inertial forces resulting from the operation of the propeller to have a strong effect on the propeller dynamics. Though the stratification and boat speed conditions evaluated herein are not as dramatic as those in a dead water situation, the trends show a considerable increase in torque when operating in strong stratification. Note that these computations are performed changing the propeller rotational speed to achieve self-propulsion. If the situation is such that the engine power is constant as the ship transitions

from well mixed to stratified conditions, the increase in torque will result in a reduction in RPM and consequent slowdown of the vessel.

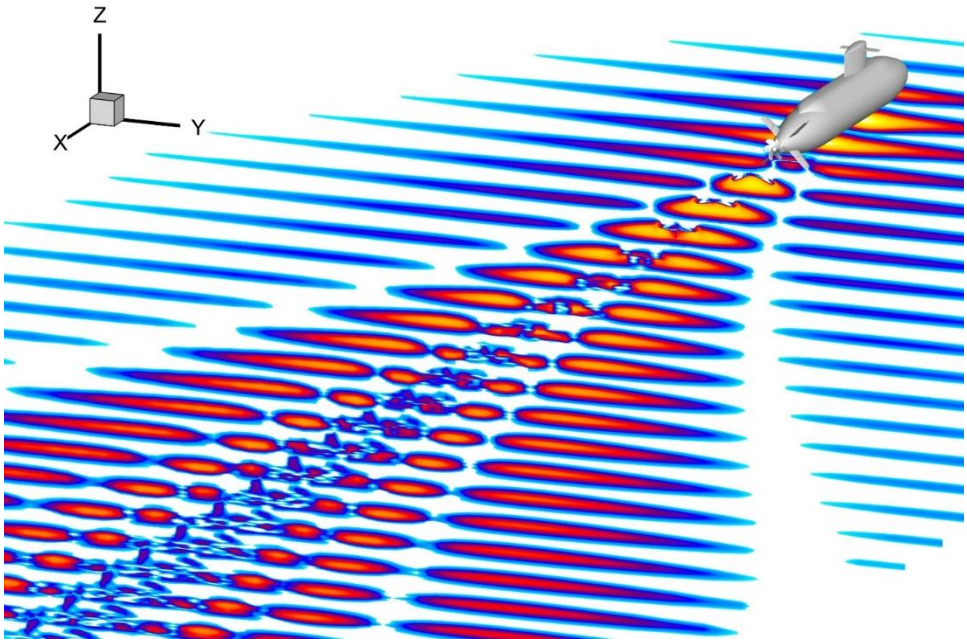

Figure 4.17: Potential power flux I_x as defined by Eq. (4.5), for self-propelled Joubert BB2 and pycnocline at $z_0/L_0 = -0.33$.

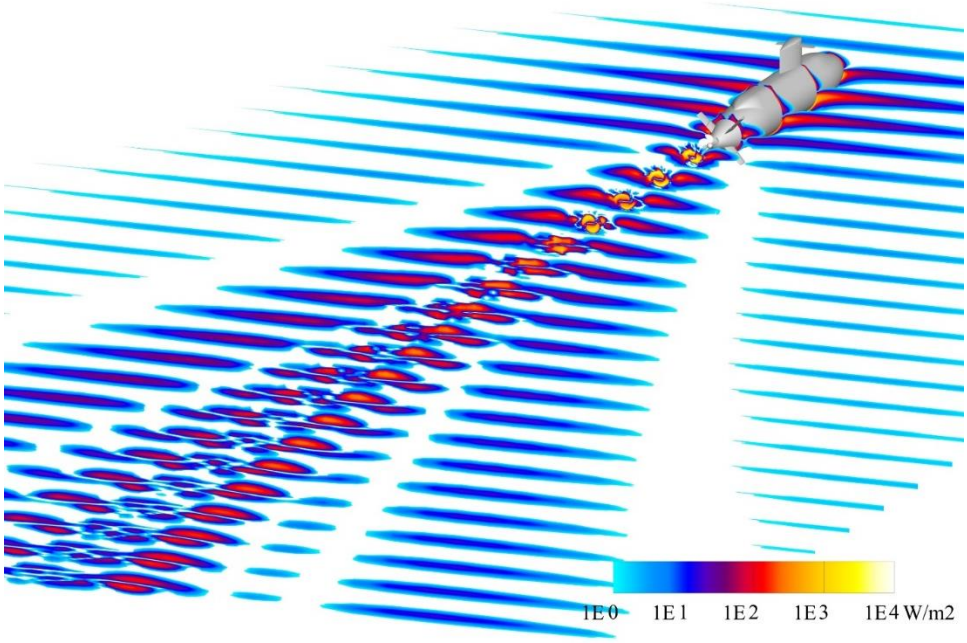

Figure 4.18: Potential power flux I_x as defined by Eq. (4.5), for self-propelled Joubert BB2 and pycnocline at $z_0/L_0 = -0.25$.

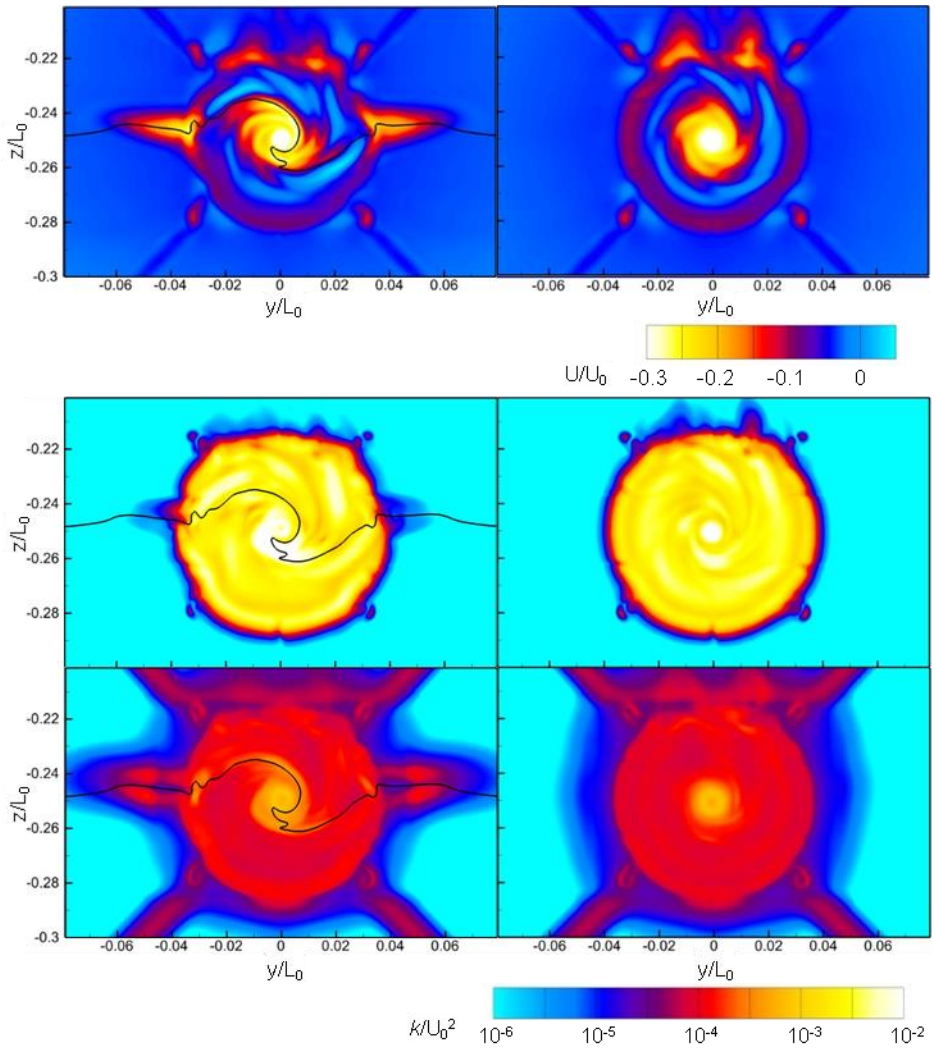

Figure 4.19: Mean velocity field 0.12 ship lengths downstream from the propeller for the self-propelled Joubert BB2. Left column: stratified case with the pycnocline at the propeller shaft; right column: non-stratified case. The top panels show mean longitudinal velocity; center panels show resolved turbulent kinetic energy; bottom panels show modeled turbulent kinetic energy. The position of the $\rho = \rho_0 + \Delta\rho/2$ contour is shown as a solid black line.

Figures 4.19 and 4.20 are useful to explain the variations observed in the wake of the propeller, based on the mean flow around it, but they are not sufficient to explain the origin of the low velocity region near the density interface. The boundary layer for the submarine is presented in Fig. 4.21, which shows that the origin of the low speed region at the interface is a thickening of the boundary layer as a result of up-swelling flow reaching

the interface. This upflow reaches the interface and rises it, while at the same time the no penetration condition across the interface forces low velocity flow out of the boundary layer, in a similar fashion to what occurs in free surface flows where the boundary layer thickens at the free surface/hull interface (Longo *et al.*, 1998). The boundary layer thickening occurs as the changes in pressure distribution due to the presence of the stratification affect the angle of attack of the submarine. This effect is clearly observed also by an increase in vorticity generated at the sail planes, far away from the stratification, that can only be explained by a change of direction of the incoming flow to the foil.

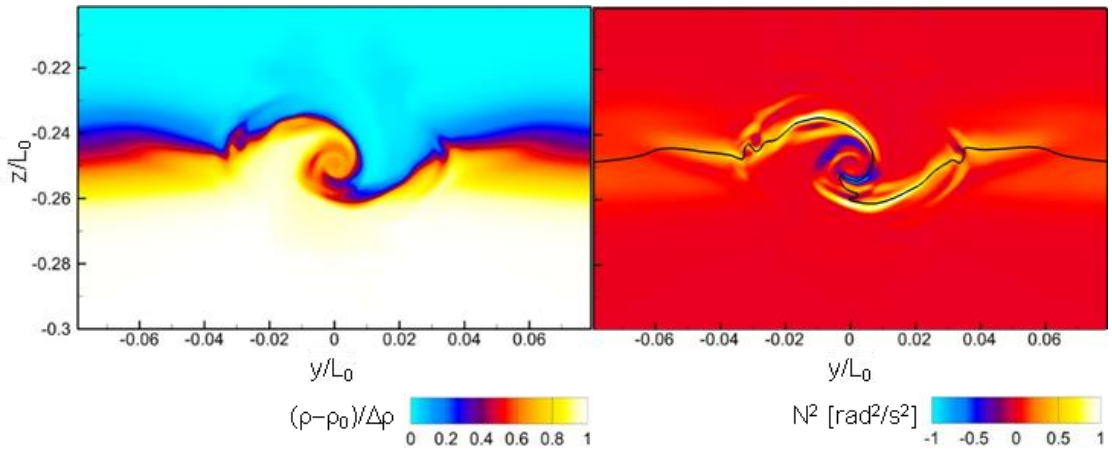

Figure 4.20: Density field 0.12 ship lengths downstream from the propeller for the self-propelled Joubert BB2, for stratified case with the pycnocline at the propeller shaft. Left: mean density; right: mean vertical density gradient, expressed as buoyancy frequency.

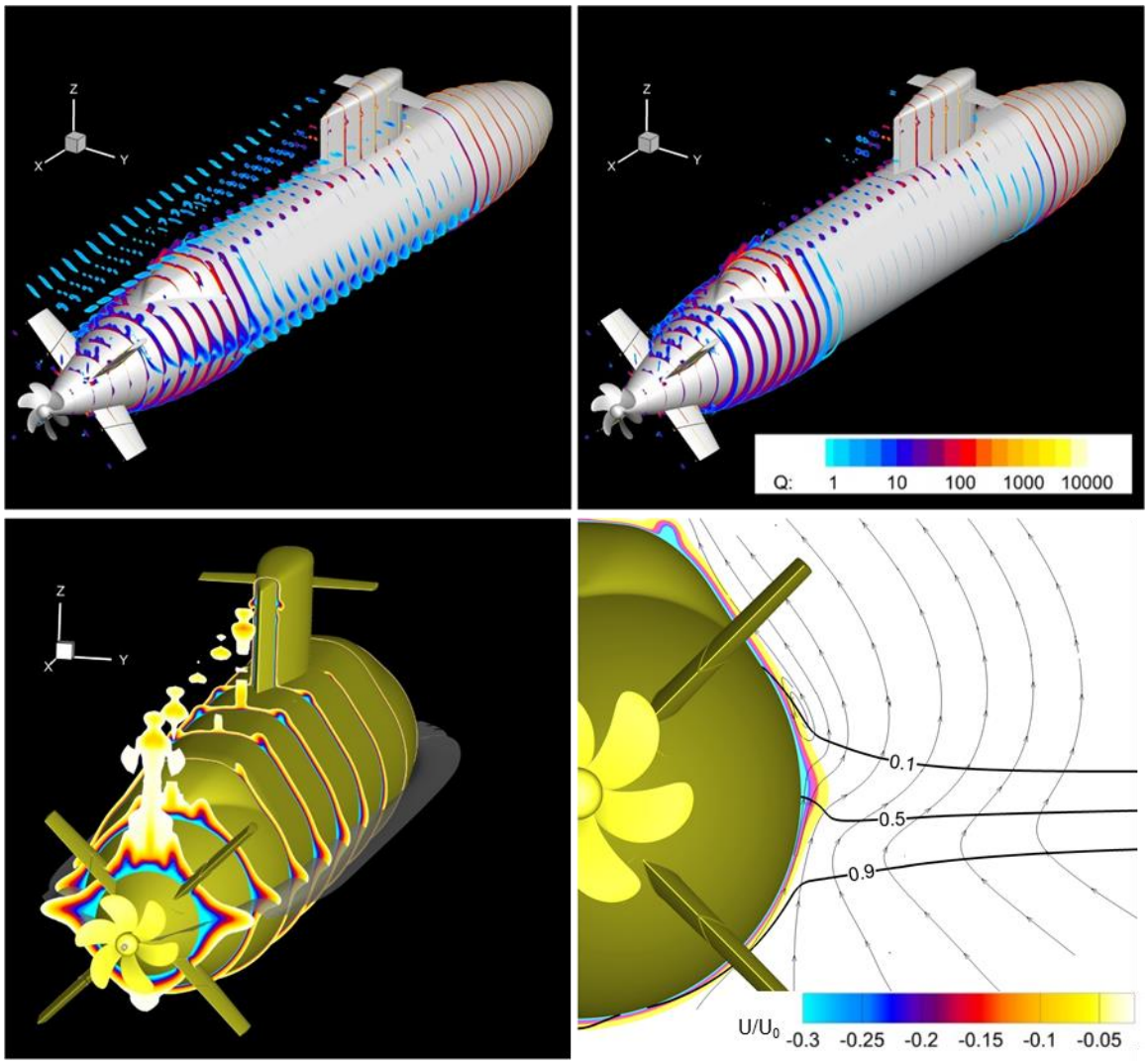

Figure 4.21: Top left: mean Q in the boundary layer of the Joubert BB2 submarine for the stratified case with the interface at the propeller shaft; top right: same for non-stratified case. Bottom left: mean longitudinal velocity on axial cross sections showing the boundary layer; bottom right: boundary layer and transverse streamlines in the mid-ships plane; three isosurfaces of mean density are also shown.

4.5 Summary

The methodology implemented in the naval hydrodynamics code REX was used to simulate the research vessel Athena and the notional Joubert BB2 submarine advancing in a stratified fluid. The computations were performed for a relatively strong stratification condition measured at the Kitimat Bay Station, in the case of R/V Athena, and for two-layer hyperbolic tangent profiles for Joubert BB2. Density disturbances on the near wake for both were analyzed. According to the results, it is observed that these near-field wakes are mostly affected by two different processes for both vessels: the separation at the wet transom and propeller mixing in the case of R/V Athena, and the disturbance of the background density profile by the presence of the vessel for the case of the submarine. The generation of an internal wave for the surface ship case is not as evident from these simulations, as it is for the submarine. This is probably related to differences in stratification strength between the two cases, extension and discretization levels of wake refinements and vertical location of the vessel with respect to the density profile. While vertical position cannot be realistically changed for surface ships, the simulations presented for the submarine case show clearly that distance to the pycnocline strongly affect the internal wave generation due to the presence of the vessel.

CHAPTER 5 DEAD WATER PHENOMENON

5.1 Introduction

In this chapter simulation of the dead-water phenomenon is performed using the numerical model implemented into REX. As it is mentioned in Chapter 1 this phenomenon takes place when the upper part of the ocean consists of layers with different densities because of large differences in either salt concentrations (for instance, fresh water from a glacier above the salty water of the ocean) or temperature. A ship passing through this environment, creates waves under the free surface and at the interface between layers of different densities. In fact, the presence of a background stratification in the water column results in a large change in resistance coefficient, order of magnitude larger than the changes in density causing it. In terms of force, it means that at the most unfavorable conditions, the resistance experienced is equivalent to that of a vessel moving two to three times faster in non-stratified conditions. If the required thrust to overcome such resistance exceeds the vessel engine capacity, the maximum speed of the vessel can be severely limited. This phenomenon, known as the dead-water effect, has been known for long time, and it is simply an expression of the relative energetic importance of the generated internal wave with respect to the vessel resistance at very low speeds. The dead-water phenomenon occurs when a ship sails in stratified seas with low speed close to the speed of the fastest internal wave and it causes the boat to lose steering power and speed. More generally, this phenomenon has been investigated in few experimental and theoretical projects to describe the importance of stratification in the ocean (Ekman, 1904; Miloh and Tulin, 1988; Tulin and Miloh, 1991; Miloh *et al*., 1993; Tulin *et al*., 2000; Mercier *et al*., 2011; Chen *et al*..

2007; Grue, 2015). However, a short review of available work reveals that there is a lack of comprehensive numerical studies related to the dead water phenomenon. Beyond the educational aspect based on historical experience, it is interesting to return to this phenomenon and try to better understand the nature of the interaction between the waves generated at the interface between the layers of different densities and the boat. This Chapter analyzes the dead-water phenomenon using computational fluid dynamics for the R/V Athena operating in a two-layered fluid. Detailed information about this research vessel is presented in chapter 4. The study includes for the first time results of effects on friction resistance, not available from analyses using potential flow. The dynamics of the formation of the internal waves are analyzed in the context of the time evolution of the resistance and the dynamics of the vessel, discussing the conditions at which the vessel can overcome the increased resistance and the dead-water speed limit, as well as the presence of a hysteretic behavior in the speed-resistance curve.

5.2 Simulation Condition of Dead Water Phenomenon

The dead water phenomenon does not always exist and it only occurs under special circumstances depending on adjustable parameters including the height of fresh water, h_1, the height of the salt water, h_2, the density difference between two layers, $\Delta\rho$, and the draft of the boat, D. Therefore, to simulate this phenomenon, a two-layer fluid is characterized by their respective height and density. The height and density corresponding to each layer are characterized as h_i and ρ_i, respectively, where $i = 1$ corresponds to the top layer and $i = 2$ the bottom layer. In this simulation, the density values for top and bottom layers are chosen

as $\rho_1 = 1000\, kg/m^3$ and $\rho_2 = 1030\, kg/m^3$, and the density profile is provided using the hyperbolic tangent function as:

$$\rho_H(z) = \rho_0 + \frac{\Delta\rho}{2}\left[1 - \tanh\frac{a(z - z_0)}{L_0}\right] \tag{5.1}$$

with z_0 the center of the pycnocline, the thin layer in a naturally stratified body of water with the largest density gradient, and a the parameter controlling the layer thickness. (see Fig. 5.1). Eq. (5.1) represents an interface that transitions from ρ_1 to ρ_2 in $0.006\, L_0$ with smooth derivatives and a maximum dimensionless density gradient $\partial\tilde{\rho}/\partial z = 175$. The background stratification is similar to that used for BB2 in the Chapter 4 (hyperbolic tangent, 3% density difference between layers), but a layer value $a = 350$ in Eq. (5.1) is used.

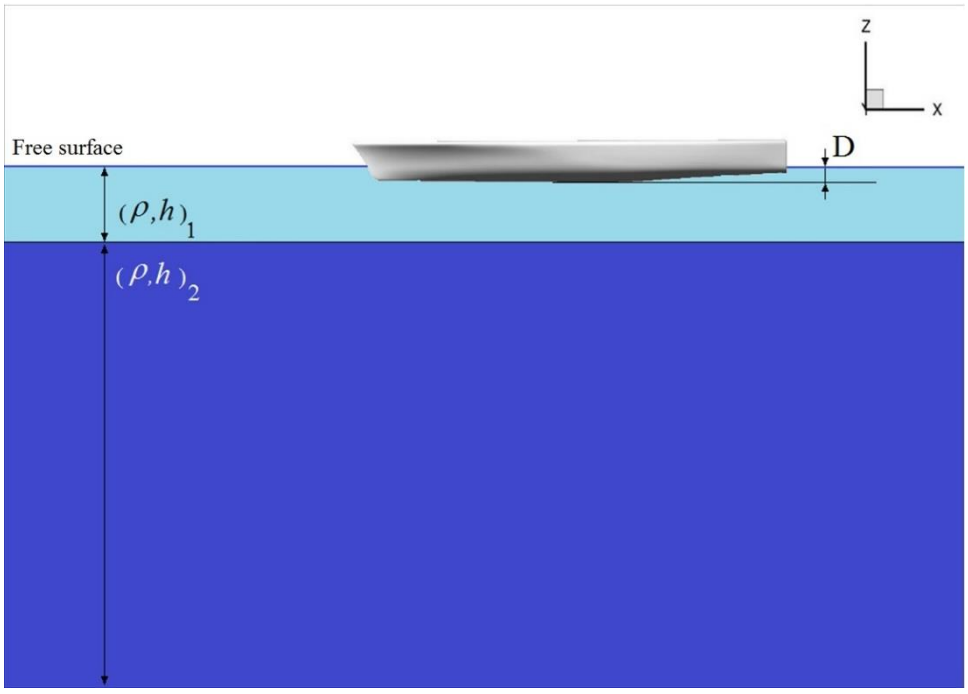

Figure 5.1: Bare hull R/V Athena geometry in two-layer fluid flow.

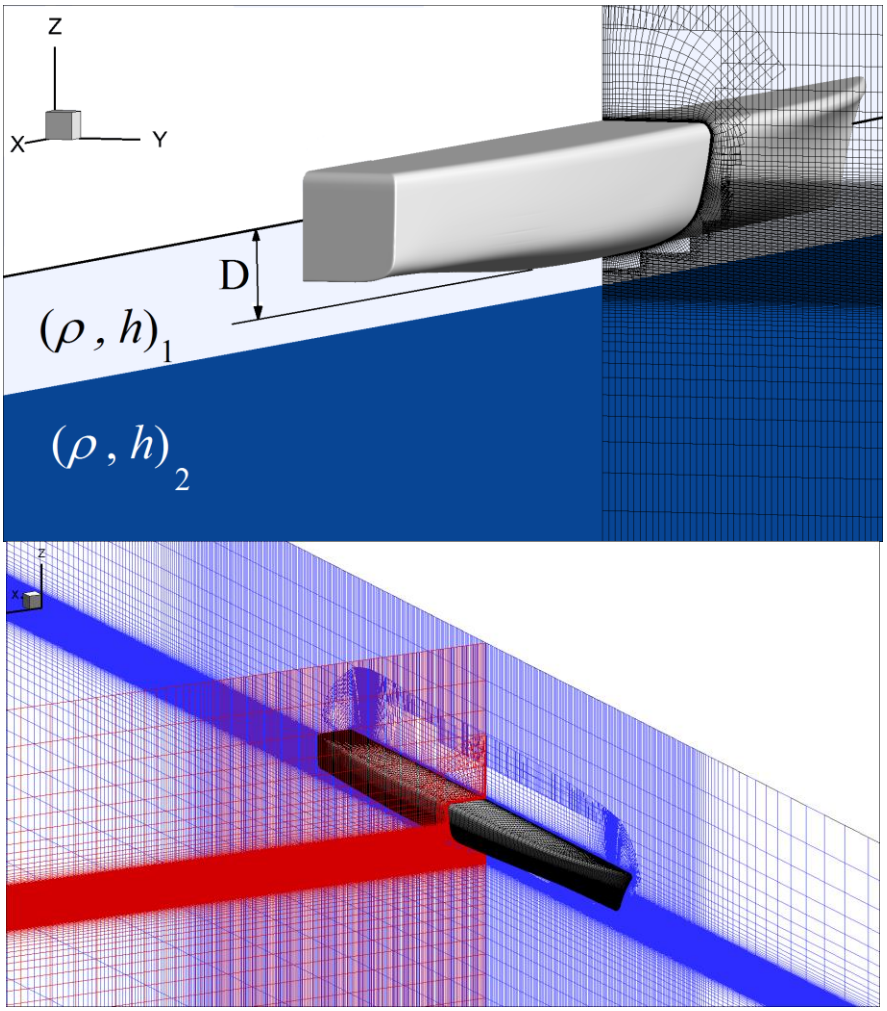

Figure 5.2: Grid topology for bare hull R/V Athena and undisturbed pycnocline position.

As the ship surface, the bare hull geometry of US Navy research vessel Athena is chosen to simulate the dead water phenomenon in the stratified flow. The ship model used in this study has the length of $L_0 = 5.69\,m$ and draft of $D = 0.205\,m$. The ship moves with zero pitch, heave or roll in a two-layer fluid as the stratified environment. The overset grid topology of bare hull R/V Athena is shown in Fig. 5.2. The grid contains two grid blocks including the bare hull and background with about 17 and 22 million grid points, depending on the position of the density interface and expected internal wave amplitude, which

requires appropriate refinement, distributed for parallel computation into 69 to 89 processors, respectively. A very large (twenty by ten ship lengths) background is used as it is anticipated that forward travelling waves occur for $c > U_0$. This background grid follows the ship but is not allowed to pitch, heave or roll so that the refinement part of this grid is designed to resolve both free surface and interface between two-layer fluid. The grid system is generated using hyperbolic solvers provided by the commercial grid generation software Gridgen. Only half of the bare hull for R/V Athena is simulated and symmetry conditions are used on the mid-plane.

The non-dimensional density profile and hydrostatic pressure distribution are imposed as initial and inlet boundary conditions using an input file into the code Also, since it is assumed that the simulation is performed for ocean water, the fluid Prandtl number is set into $Pr = 1$, and turbulent Prandtl number is set into $Pr_t = 0.9$. As the turbulence model, DDES model is chosen for all computations. The far-field boundary conditions set into the background grid includes the inlet condition with zero velocities and imposed density profile, outlet condition with zero second derivative for velocities and zero gradient for other variables, and also zero gradient for all variables at the other four boundaries. All the computations are conducted on Helium and Neon supercomputers at the University of Iowa. Fourth and second order hybrid methods are chosen for the momentum and level-set equations respectively, and the convergence tolerance is set into 10^{-5} for both equations. To solve the density transport equation, second order implicit Euler method for time discretization, second-order upwind for convection term and second-order-centered scheme for diffusion term are chosen and the convergence tolerance of the density field is set into 10^{-5}. The time step is set into $\Delta t = 0.005$ to properly resolve the both free surface and

interface between two layers throughout the computation domain and obtain accurate numerical solutions of both stratified and non-stratified conditions. The only difference between the stratified flow with density profile and the non-stratified cases is that in the case of non-stratified flows the Richardson number is set to $Ri = 0$ and the momentum equation is independent from the density transport equation.

5.3 Ship Moving in Two-layer Stratified Flow

It is known that the increase in resistance is maximum for $Ri_H \sim O(1)$, with the Richardson number is defined with an appropriate vertical length-scale:

$$Ri_H = \frac{\Delta\rho}{\rho_0}\frac{g h_1}{{U_0}^2} \tag{5.2}$$

This condition is therefore dependent on stratification strength, interface depth (assuming for simplicity a two layer system) and ship speed. By choosing 3% density difference between layers and reference place for the interface as $h_1/D = 1.5$, the reference velocity can be calculated from Eq. (5.2) . According to the definition of the bulk Richardson number and using the information about R/V Athena in model scale, the bulk Richardson number, Froude number and Reynolds number are calculated and they are set into $Ri = 1.33$, $Fr = 0.15$ and $Re = 6.37 \times 10^6$ for all cases of stratified flow. The simulations are performed for different positions of interface as h_1/D where D is the draft of R/V Athena. Non-stratified simulations are identical to simulations with stratification except for setting Richardson number into $Ri = 0$ and no stratification in the initial and boundary conditions.

As the ship evolves through a stable stratified background it disturbs the flow and creates internal waves that propagate downstream. For the two-layer stratified flow the

pattern of these internal waves depends on the densimetric Froude number defined as (Molih *et al*., 1993):

$$Fr_h = \frac{U_s}{c^*} \tag{5.3}$$

where c^* represents the celerity of the longest internal waves and it is expressed as:

$$c^* = \sqrt{g'h'} = \sqrt{\left(g\frac{\Delta\rho}{\rho_1}\right)\left(\frac{h_1 h_2}{h_1 + h_2}\right)} \tag{5.4}$$

where geometric parametric h_1 and h_2 are lower and upper layer depths, and ρ_1 and ρ_2 are corresponding densities which are shown in Fig. 5.1. Also $g' = g(\rho_2 - \rho_1)/\rho_1$ is modified acceleration of gravity due to buoyancy and the internal waves are restored by this reduced gravity. Generally, the dead water phenomenon occurs when the densimetric Froude number has the order of $Fr_h = O(1)$. For an infinitely deep lower layer with $h_1 \ll h_2$, we assume that $h_1 = h$ and $\rho_1 = \rho_0$. Therefore, the densimetric Froude number and Richardson number can be represented as:

$$Fr_h = \frac{1}{\sqrt{Ri_h}} = \frac{U_s}{\sqrt{gh\frac{\Delta\rho}{\rho_0}}} \tag{5.5}$$

with the same $O(1)$ requirement for maximum resistance. In fact, the resistance induced by the internal wave peaks at $Fr_h = 1/\sqrt{Ri_h} \sim O(1)$, with $Ri_h = gh\Delta\rho/\left(\rho_0 {U_s}^2\right)$. Thus the same Richardson number (or densimetric Froude number) can be achieved varying the depth of the pycnocline (h/D in dimensionless form, with D the draft of the ship) or the ship speed, U_s. Simulations were conducted in three modes:

- Varying densimetric Froude number in the range $0.64 \leq Fr_h \leq 1.82$ by changing pycnocline depth ($0.375 \leq h/D \leq 3$) and maintaining speed at $U_s = 0.79\ m/s$ (1.53 *knots*, in full scale).
- Varying densimetric Froude number in the range $0.68 \leq Fr_h \leq 2.73$ by changing speed ($U_s = 0.59\ m/s$ to $2.37\ m/s$, 1.14 to 4.59 *knots*, in full scale) at a constant pycnocline depth $h/D = 1.5$.
- Maintaining constant densimetric Froude number at $Fr_h = 0.77, 0.83, 0.91$ and 1.27 by changing speed and pycnocline depth simultaneously in the range $0.375 \leq h/D \leq 2$.

Resistance coefficients for all cases including the resistance coefficient R_t for non-stratified flow are calculated and presented in next sections.

5.3.1 Grid Study of Ship Moving in Two-layer Stratified Flow

To evaluate grid convergence, three different grids are generated for the Athena geometry to estimate numerical errors due to grid size. Only the starboard side of the ship is simulated, taking advantage of the centerplane symmetry of the problem. For the case $h/D = 1.5$, the grid system including hull and background blocks is created using Gridgen with 21.9 million points as the Medium grid system (see Fig. 5.2). Using a post-processing tool, the Medium grids are input into the post-processing tool and a series of three, 1D interpolations are performed to create Fine and Coarse grid systems with the grid refinement ratio of $r_G = \sqrt{2}$. Only two cases are simulated using three grids due to cost; all other cases are run with the Medium grids. The resulting Coarse, Medium, and Fine grids have roughly 7.7M, 21.9M and 61.5M grid points, respectively. The simulations required for the grid study are run with different time steps so that the Courant number is the same, resulting in

$\Delta t = 0.007, 0.005$ and 0.0035 for the Coarse, Medium and Fine grids, respectively. The system is distributed for parallel computation to between 69 to 89 processors, with all computations conducted at the Helium and Neon clusters at the University of Iowa. Non-slip boundary conditions are imposed at the hull, while inlet and exit are imposed at the upstream and downstream faces of the background grid, respectively, centerplane symmetry at $y = 0$, and far-field conditions on the other faces. Initial and inlet conditions impose also the density stratification profile in Eq. (5.1).

Simulations are performed in model scale, though results are reported in dimensionless form or, when relevant, in full scale using only Froude scaling with no Reynolds number corrections. The Reynolds, Froude and bulk Richardson numbers are $Re = 6.75 \times 10^6$, $Fr = 0.15$ and $Ri = 1.33$, , respectively, computed with reference length and speed of $L_0 = 5.69\ m$ and $U_0 = 1.12\ m/s$ ($47\ m$ and $3.21\ m/s$ in full scale).

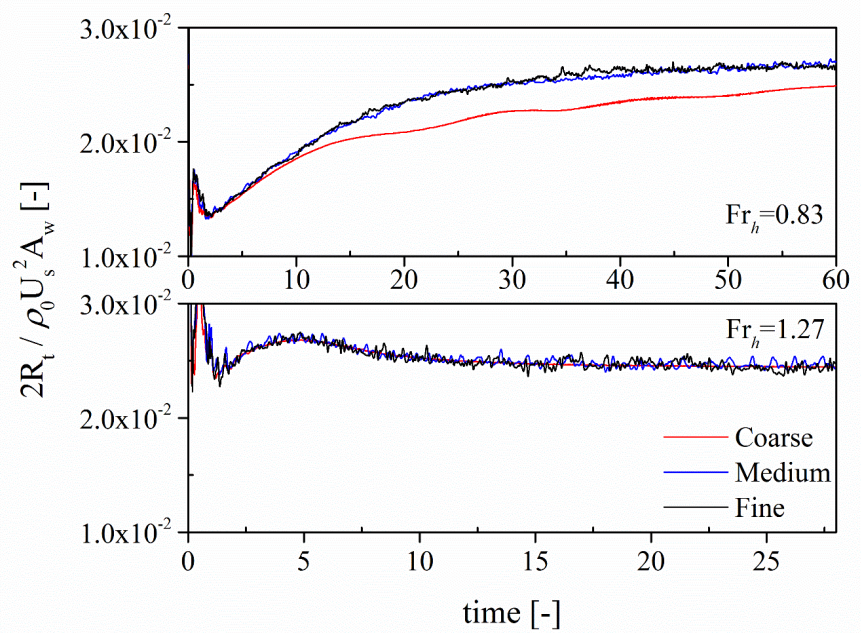

Figure 5.3: Time history of resistance coefficient for three different grid systems at $h/D = 1.5$.

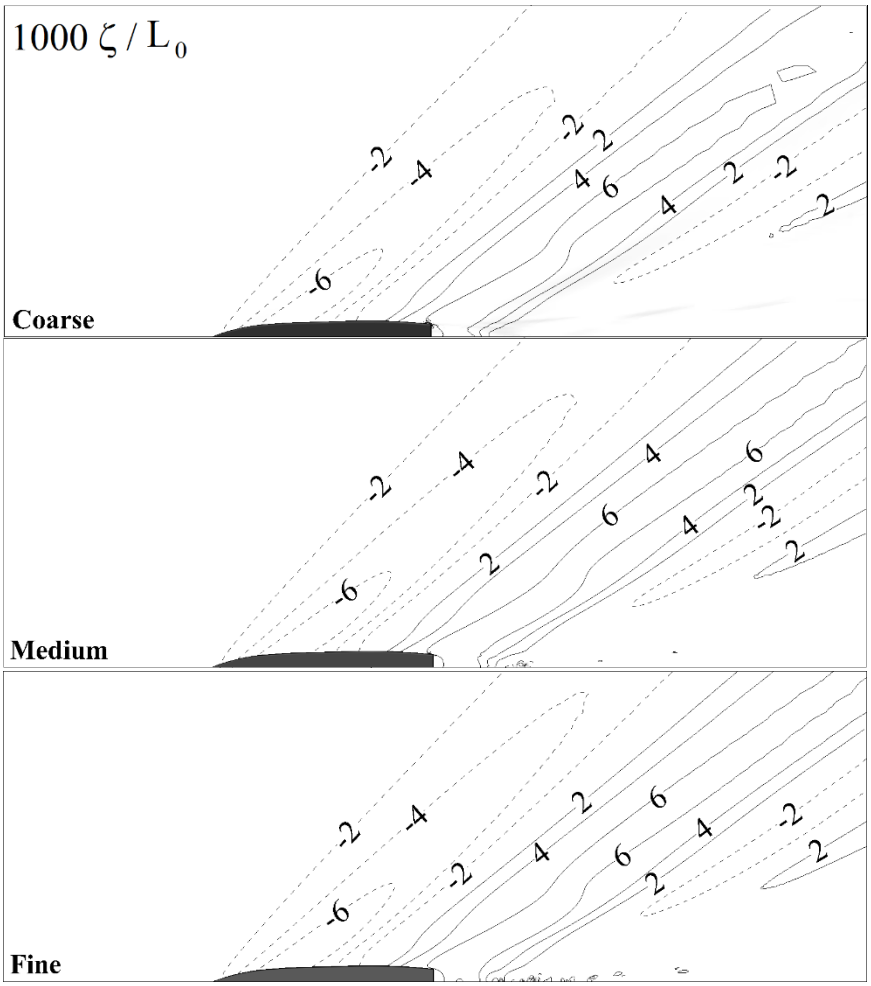

Figure 5.4: Internal wave elevation for all grids at $Fr_h = 1.27$.

Two speeds at constant pycnocline depth $h/D = 1.5$ are used to evaluate grid convergence, resulting in $Fr_h = 0.83$ and $Fr_h = 1.27$. Figure 5.3 shows the time histories of resistance for these conditions. In the case of lower speed ($Fr_h = 0.82$) the densimetric Froude number is close to critical where the resistance changes rapidly with Fr_h and there is significant difference between coarse and medium grids, but the difference between medium and fine grids is very small. The coarse grid is unable to properly resolve the internal wave, particularly at the stern, but the medium and fine grids predictions are very

close, as shown in Fig. 5.4. At higher speed the resistance due to the internal wave is less sensitive to Fr_h, and the three grids predict similar results.

5.3.2 Ship Moving in Two-layer Stratified Flow with Constant Speed and Various Pycnocline Positions

As the first case the simulations are performed using a fixed towed configuration for constant ship speed and different pycnocline depths. For different pycnocline positions varying from 0.5 to 3.5 of the upper layer depth and for densimetric Froude number in the range of $Fr_h \approx 0.59 - 1.58$ R/V Athena is moved in both two-layer stratified and homogeneous non-stratified environments and the results are analyzed to find the critical interface position with maximum resistance coefficient. For each case the resistance coefficient is calculated and its variation at different interface positions for both stratified and non-stratified flows is shown in Fig. 5.5. It is observed that the maximum resistance coefficient occurs at $h/D = 1.5$ and it is about five times larger than the resistance found for an equivalent non-stratified condition. It is interesting to note that regardless of the ship draught the resistance coefficient only depends on densimetric Froude number. Also, by increasing pycnocline position the resistance of stratified flow and non-stratified flow eventually will have the same value and the ship cannot affect the interface any longer. Figure 5.6 shows instantaneous results of internal wave on the interface between two layers of fluids for the different cases simulated. The movement of the ship disturbs the interface between the two layers in its wake. Therefore, the flow of fluid over the ship generates a negative pressure in the opposite direction of ship motion which raises the rear interface. According to Fig. 5.6 the elevation of internal wave in the case of $h/D = 1.5$ is greater than

the other cases which means that more work is required to create these waves. Finally, for the case of $h/D = 3$ ship barely affects the interface and it behaves close to the non-stratified condition.

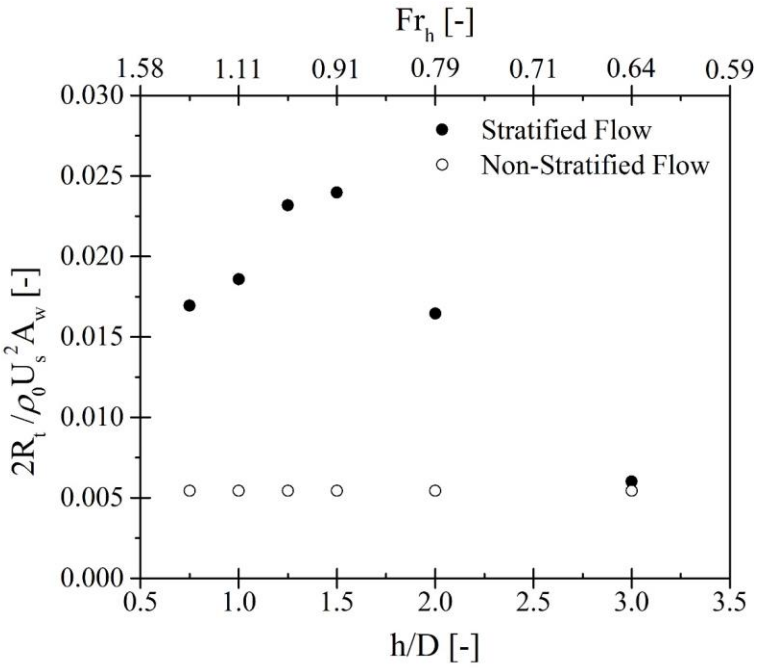

Figure 5.5: The variation of resistance coefficient at different pycnocline positions for both stratified and non-stratified flows. The densimetric Froude number scale is also provided for variable interface position.

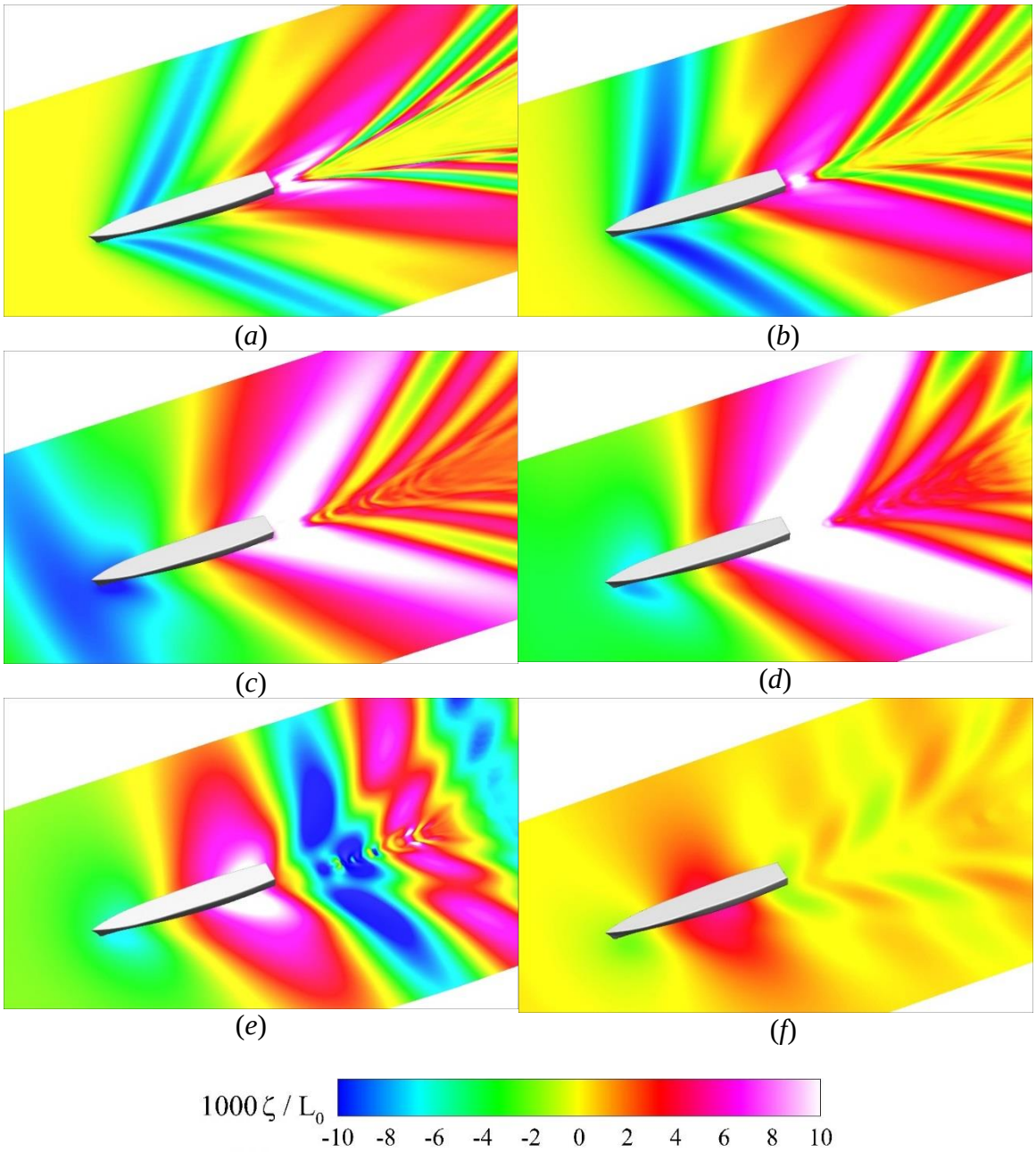

Figure 5.6: The internal wave elevation on interface (as iso-surfaces of ($\rho = \rho_0 + \Delta\rho/2$) for (a) $h/D = 0.75$ (b) $h/D = 1$ (c) $h/D = 1.25$ (d) $h/D = 1.5$ (e) $h/D = 2$ and (f) $h/D = 3$. Wave elevation is shown as thousandths of ship length.

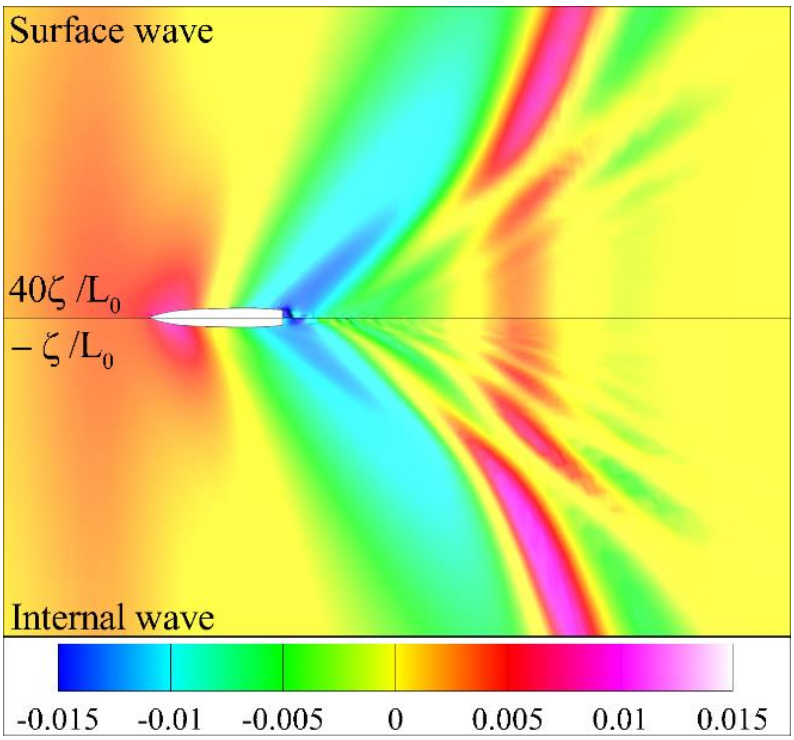

Figure 5.7: Internal wave and surface wave elevations for $Fr_h = 0.91$ and $h/D = 1.5$.

The comparison between internal and surface waves are shown for $h/D = 1.5$ with densimetric Froude number of $Fr_h = 0.91$ in Fig. 5.7. It is interesting to notice that the surface waves are coupled with the structure of the internal waves and both waves have the same structure. The free surface waves, created by the interaction of the air/water interface with the advancing ship, are of very small wavelength and height due to the low Froude numbers ($Fr < 0.05$) at which the ship operates when presenting dead water effects (the grid density used in this work is too coarse to resolve these very small free surface waves), and in non-stratified flow the free surface is essentially flat. In stratified flow, the free surface mirrors the internal wave with opposite sign: peaks in the free surface appear in troughs in the internal wave and vice versa. This occurs because the flow is accelerated in restricted areas (peaks in the internal wave), reducing the pressure and sucking in the free surface. The opposite occurs in troughs in the internal wave. Figure 5.7 shows that the amplitude of

the free surface elevation is approximately 2.5% that of the internal wave for $Fr_h = 0.91$ and $h/D = 1.5$.

After finding the maximum resistance for a specific h/D, the second simulation is perfumed for different Froude and Reynolds number to capture the behavior of the resistance force on the ship hull.

5.3.3 Ship Moving in Two-layer Stratified Flow with Constant Pycnocline Position and various Speeds

As the second case the simulations are performed using constant positions of interface as $h/D = 1.5$ and various ship towed speeds. For different ship speeds R/V Athena is towed in both two-layer stratified and homogeneous non-stratified environments and the variation of resistance coefficient versus ship speed is shown in Fig. 5.8. As the same behavior as the resistance in different interface positions, the maximum peak of resistance occurs at $Fr_h \approx 0.9$ and the amplitude of internal wave resistance decreases rapidly for both low and high Fr_h which is in agreement with theoretical results provided by Miloh *et al*. (1993). In fact, it is expected that the maximum resistance occurs at $Fr_h = 1$; but the dead water phenomenon shifts the maximum resistance to $Fr_h \approx 0.9$ with subcritical ship speed. The sharp increase of resistance coefficient at subcritical speeds provides the explanation for the dead-water phenomenon occurring while a ship moves slowly in stratified flow and these results support the hypothesis of highest resistance associated with internal waves of celerity approximately equal to the ship speed, equivalently to the well-known result of maximum surface wave resistance occurring for wave celerity similar to the ship speed.

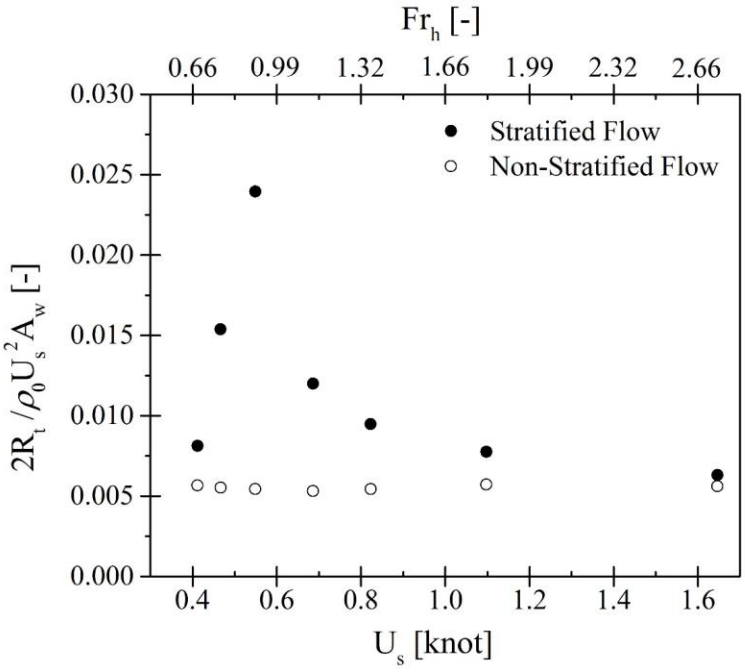

Figure 5.8: The variation of resistance coefficient at different ship speeds for both stratified and non-stratified flows. The densimetric Froude number scale is also provided for variable ship speed.

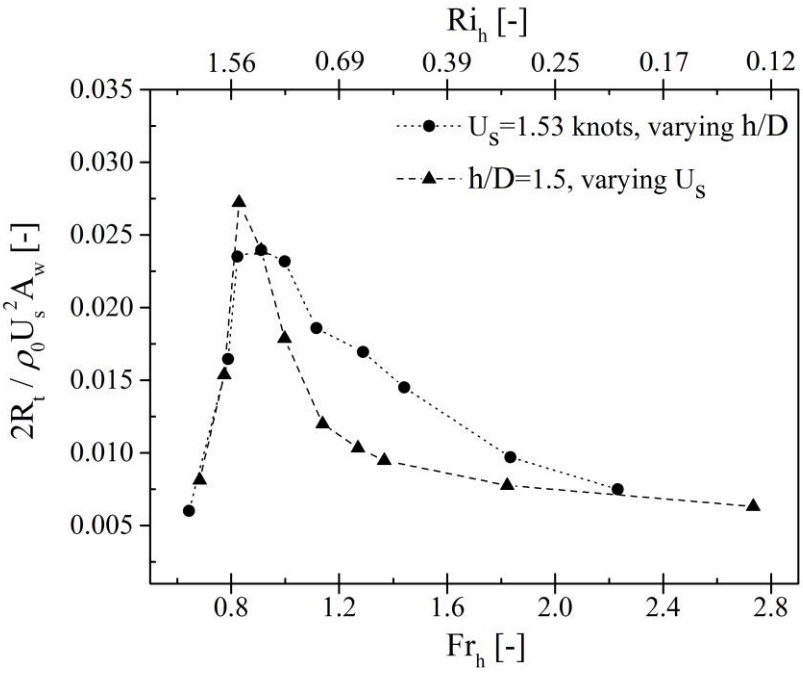

Figure 5.9: The comparison of resistance coefficient for two different operational modes as a function of densimetric Froude number (Richardson number).

It is interesting to compare the resistance variation for both cases of constant velocity and constant interface position with Ri_h at the same figure. Figure 5.9 shows the variation of internal wave resistance with both Fr_h and Ri_h. At subcritical densimetric Froude number, Fr_h, the resistance is approximately the same regardless of whether the depth or the speed are varied. However, at larger Fr_h there are differences in resistance between two cases of fixed speed and interface position. Figure 5.10 shows that depending on internal Froude number being smaller or larger than critical internal Froude number, the internal wave pattern is very different.

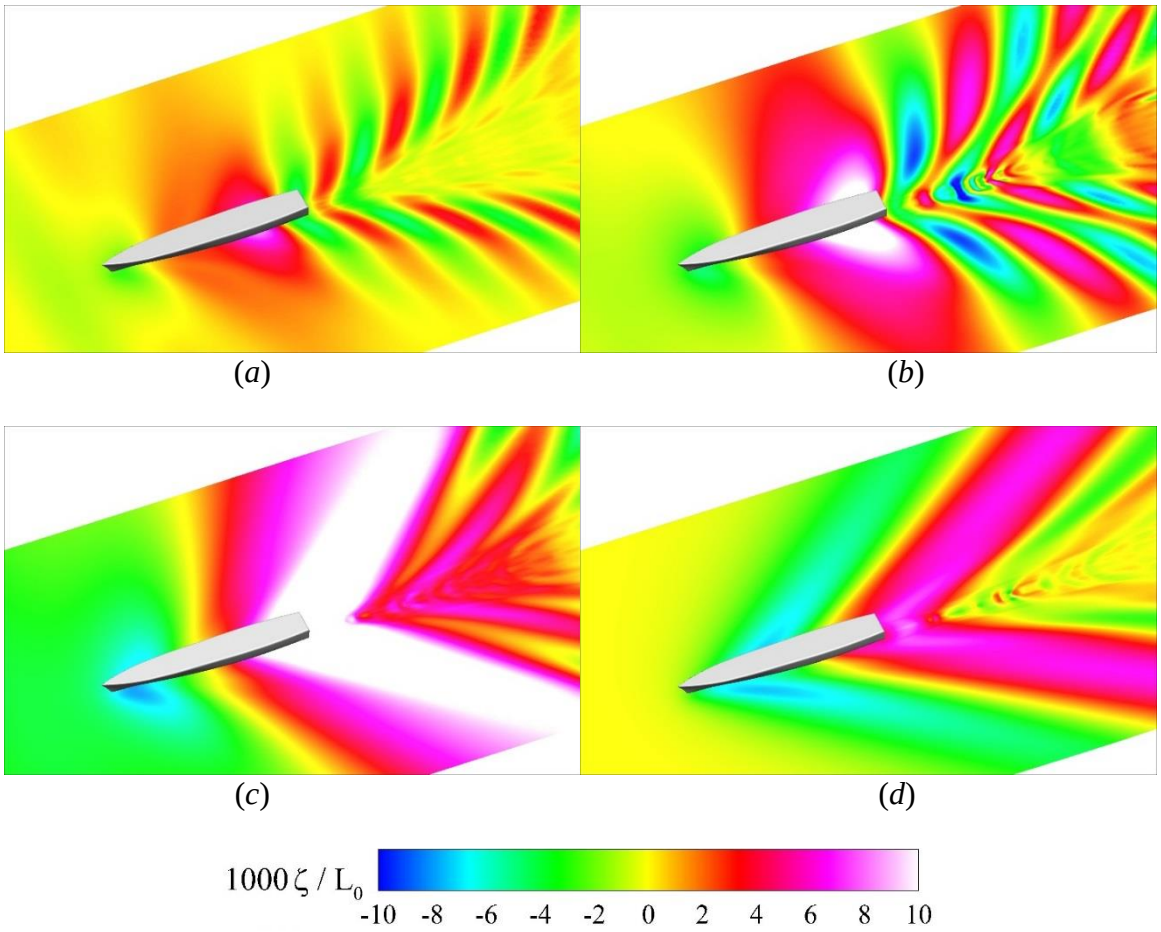

Figure 5.10: The internal wave elevation on interface for different ship speed of (a) $U_s = 0.41\ knots$ (b) $U_s = 0.45\ knots$ (c) $U_s = 0.53\ knots$ (d) $U_s = 0.79\ knots$ in model scale. Wave elevation is shown as thousandths of ship length.

5.3.4 Ship Moving in Two-layer Stratified Flow with Constant Densimetric Froude Number

For computations maintaining constant pycnocline depth or ship speed, the resistance coefficient is approximately the same at subcritical Fr_h regardless of whether the pycnocline depth or the speed are varied. This is expected as a subcritical Fr_h corresponds to strong stratification conditions that dominate over other effects. However, at larger Fr_h

the resistance coefficient is higher when the same densimetric Froude number is achieved decreasing the pycnocline depth instead of increasing the ship speed. The depth of the pycnocline, however, plays a significant role when evaluated at constant densimetric Froude number.

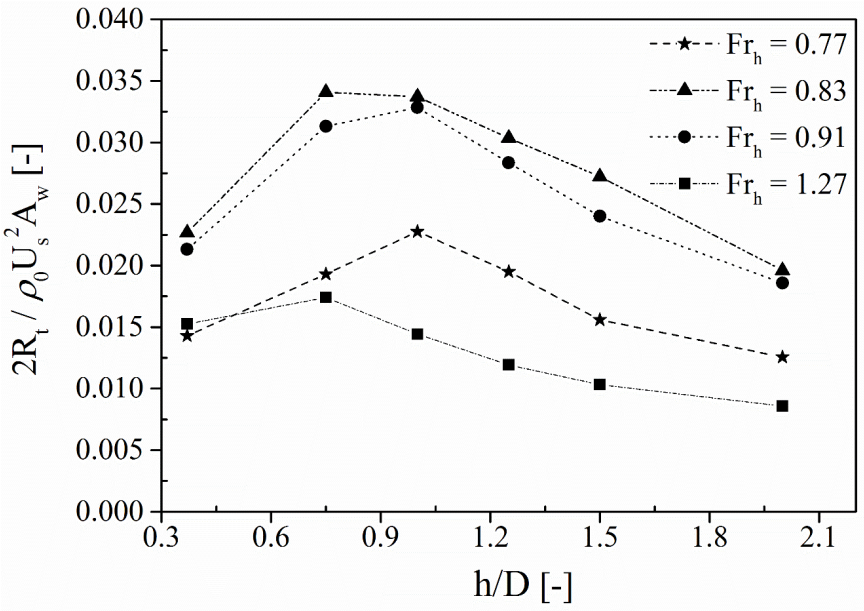

Figure 5.11: Resistance coefficient as a function of h/D at constant Fr_h.

Figure 5.11 shows the variation of the resistance coefficient with pycnocline depth for different densimetric Froude numbers. The resistance coefficient peaks for pycnocline depths in the range $0.75 \leq h/D \leq 1$, conditions where the density interface is touching the bottom of the hull. This indicates strong near-field effects of the interactions between the hull and the internal wave, which will be discussed in next section. Using a strongly nonlinear potential flow method, Grue (2015) reported similar trends for the effects the draft of a hull form acting on an interface at fixed depth. Resistance coefficients for all cases are shown in Fig. 5.12, which also includes the resistance coefficient for non-stratified flow

which offers rich information. The resistance peaks between $Fr_h = 0.83$ and $Fr_h = 0.91$, depending on the location of the pycnocline, and decreases rapidly for lower and higher Fr_h. These results are in agreement with the study of Miloh *et al*. (1993) for a prolate spheroid, which peaked at $Fr_h = 0.88$. Notice also that the resistance coefficient is about 6 times higher than for the case without stratification.

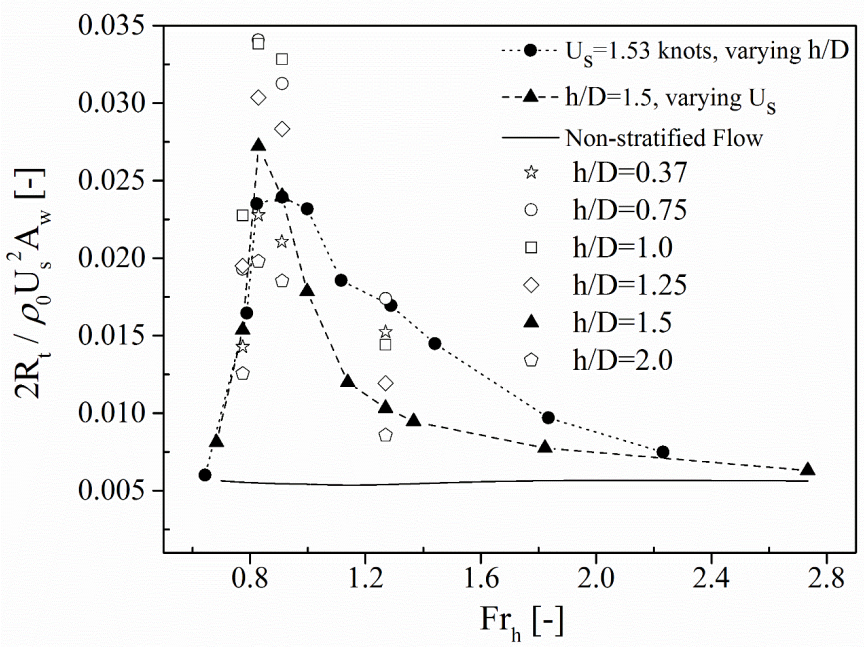

Figure 5.12: Resistance coefficient as a function of Fr_h and different h/D or ship speeds for three different operational modes.

Of particular interest is the change in friction resistance in stratified flow, which cannot be predicted with potential flow methods. Figure 5.13 shows that increases in friction resistance are considerable, and as it is the case with the total resistance coefficient, peak at $Fr_h = 0.8$~0.9. The friction resistance peaks for pycnocline depths in the range $1 \leq h/D \leq 1.25$ for subcritical Fr_h, with much smaller influence of interface depth at supercritical $Fr_h = 1.27$. This increase in frictional resistance is a result of thinning of the boundary layer caused by a favorable pressure gradient and local flow acceleration due to the constraint that

the density interface presents to the flow. This phenomenon will be further discussed in Section 5.3.6. Note that at the viscous component contributes with 16% of the total resistance at the peak for stratified flow, while for non-stratified flow the friction accounts for approximately 80% of the total resistance.

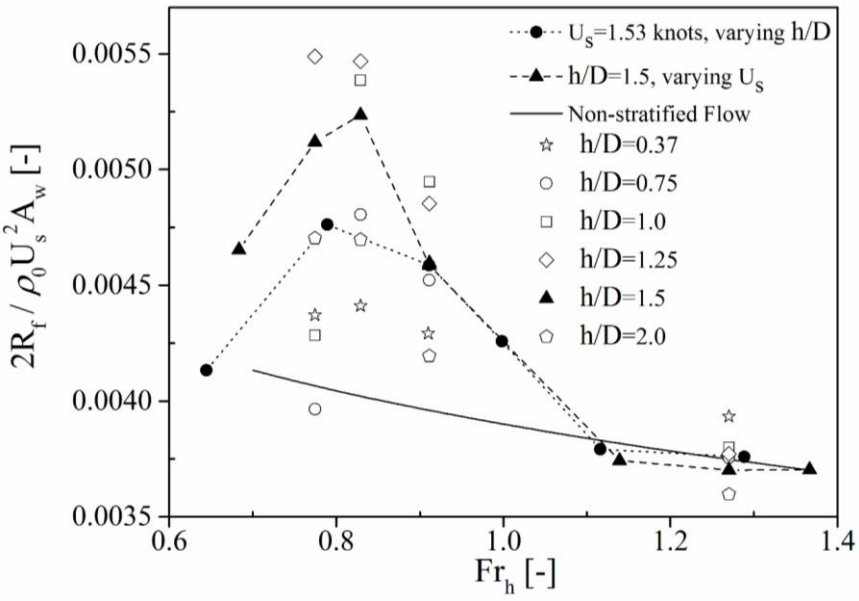

Figure 5.13: Friction resistance coefficient as a function of Fr_h and different h/D or speeds.

5.3.5 Internal Wave of Dead Water

As has been well established by other researchers (Lacaze *et al*., 2013), the internal waves are characterized mainly by the densimetric Froude number and dimensionless obstacle height h/D, as shown in Figs. 5.14-5.15, and display similar characteristics to free surface waves. The highest amplitude in Fig. 5.14, which shows the internal wave for $h/D = 1$, occurs at $Fr_h = 0.83$, coincident with the peak in resistance coefficient in Fig. 5.12. The occurrence of the peak at subcritical Fr_h has been previously reported by Miloh *et al*. (1993)

and Duchene (2011), and corresponds to dispersion effects due to finite depth of the top layer. Notice also that a distinct wake in the internal wave is observed, another characteristic that cannot be captured with potential flow methods. At subcritical densimetric Froude numbers ($Fr_h = 0.77$ and 0.83) the presence of transverse waves is clear. $Fr_h = 0.91$ behaves as a near critical densimetric Froude number, slightly lower than the expected $Fr_{h,c} = 1$. This behavior has been reported also in the experiments of Lacaze *et al*. (2013) who attribute the difference to the lack of excitation of faster, long waves than the ship length that would be able to travel upstream. At the supercritical condition $Fr_h = 1.27$ the transversal waves disappear and a Mach cone is observed (Rabaud and Moisy, 2013).

The effect of depth on the internal waves is shown in Figs. 5.15 for $Fr_h = 0.91$. The wave field far from the ship is fairly independent of the depth of the pycnocline, but effects are strong near the body. Most noticeably, immediately downstream of the stern the internal wave forms a pattern similar to a "rooster tail" for surface waves, shown in the inserts and most noticeably for $h/D \leq 1$. This pattern is typical of dry conditions in transom stern ships like R/V Athena operating at high Froude numbers (Bhushan *et al*., 2009). At higher h/D a rooster tail is still visible but separates farther downstream of the stern and produces two peaks and a trough.

At higher pycnocline depths the recovery point of the rooster tail occurs further downstream, causing the crest locus of the stern divergent wave to move downstream as well. In the wake of the ship a stationary pattern is observed, similar to the one reported by Lacaze *et al*. (2013). Higher densimetric Froude numbers result in narrower internal wave wakes, see Figs. 5.15, as is also the case in surface waves, with higher pycnocline depths having the same effect.

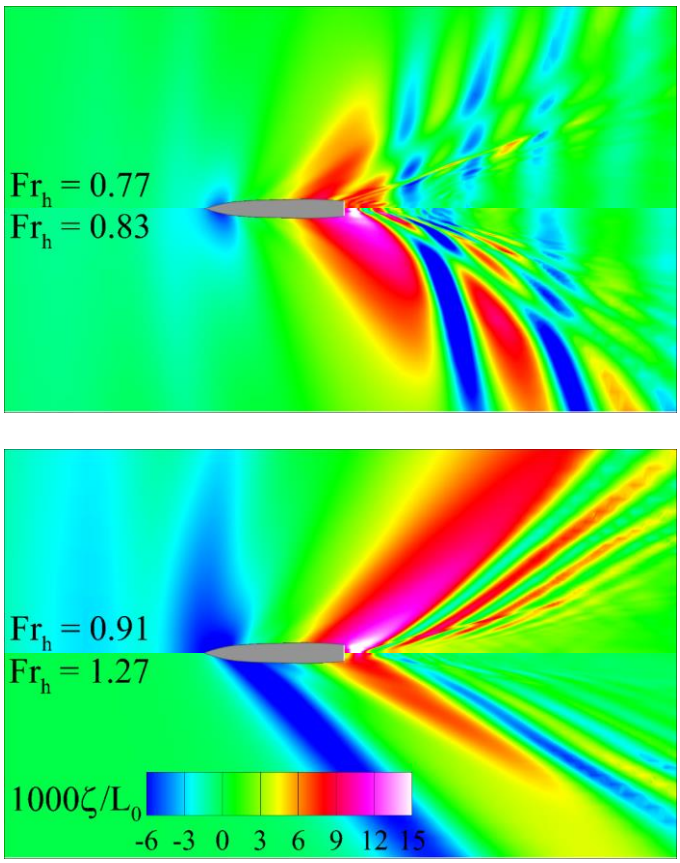

Figure 5.14: Internal wave elevation as a function of Fr_h for $h/D = 1$.

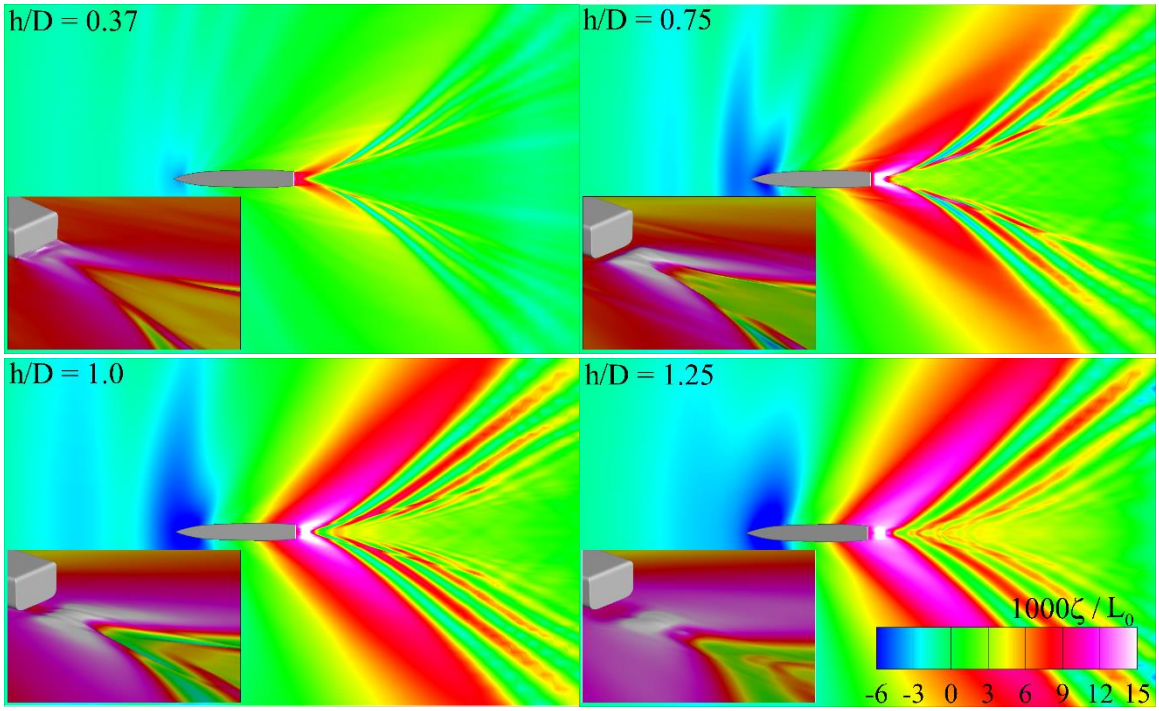

Figure 5.15: Internal wave elevation as a function of depth for $Fr_h = 0.91$.

5.3.6 Flow Field of Dead Water

The presence of the pycnocline imposes interfacial forces that strongly affect the flow. Not considering the small mixing caused by turbulence, the sharp interface effectively acts as a slip boundary condition for the flows in both sides of it. The large-amplitude internal wave occurring for cases close to peak resistance influence the flow field significantly. Figure 5.16 shows the dimensionless cross (V/U_0) and axial (U/U_0) velocities on the interface for the case with $Fr_h = 0.91$ and $h/D = 1.5$. The presence of the internal wave causes considerable inflow in the stern of the ship, where the crest of the internal wave exists and restricts the passage area, resulting in an acceleration of the flow and higher axial velocities than for the non-stratified case.

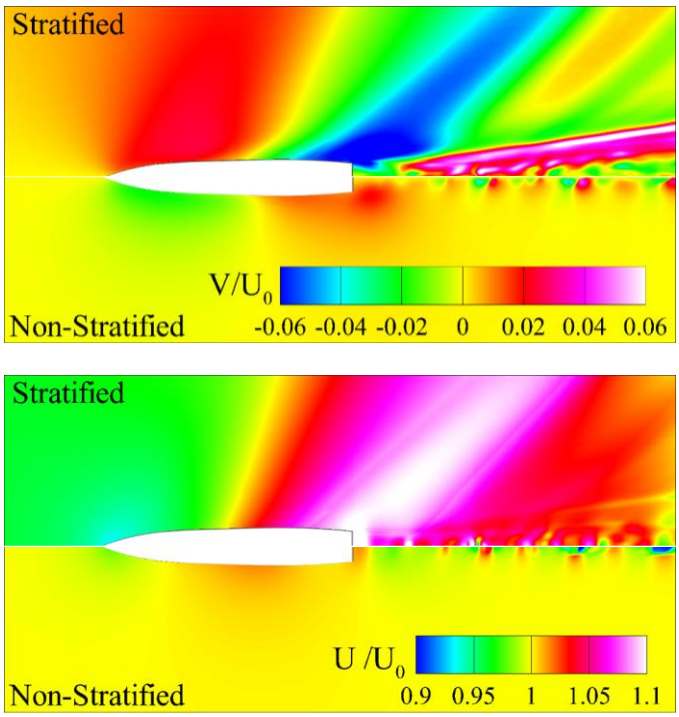

Figure 5.16: Cross (top) and axial (bottom) velocity at the internal wave for $Fr_h = 0.91$ and $h/D = 1.5$.

This can be seen in Fig. 5.17 as a low pressure, high-velocity region below the ship in the downstream half of the hull. This higher velocity and resulting favorable pressure gradient result in a much thinner boundary layer than for the non-stratified flow case (for which a scalar with the same initial distribution as density is passively transported by the flow to produce an equivalent iso-surface), with the consequent increase in friction resistance shown in Fig. 5.13. Similar effects were also reported for a submarine near a density interface by Martin *et al*. (2016). It is interesting to note that the presence of stratification flattens the interface in the wake, both due to the effect of restitutive buoyancy forces and inhibition of turbulent mixing and stirring, resulting in more consistent vortex detachment from the transom stern than for non-stratified flow. The higher axial velocity in

the stratified case also results in higher vortex detachment frequency. The vortex detachment dynamics play an important role in the behavior of the wake of the ship.

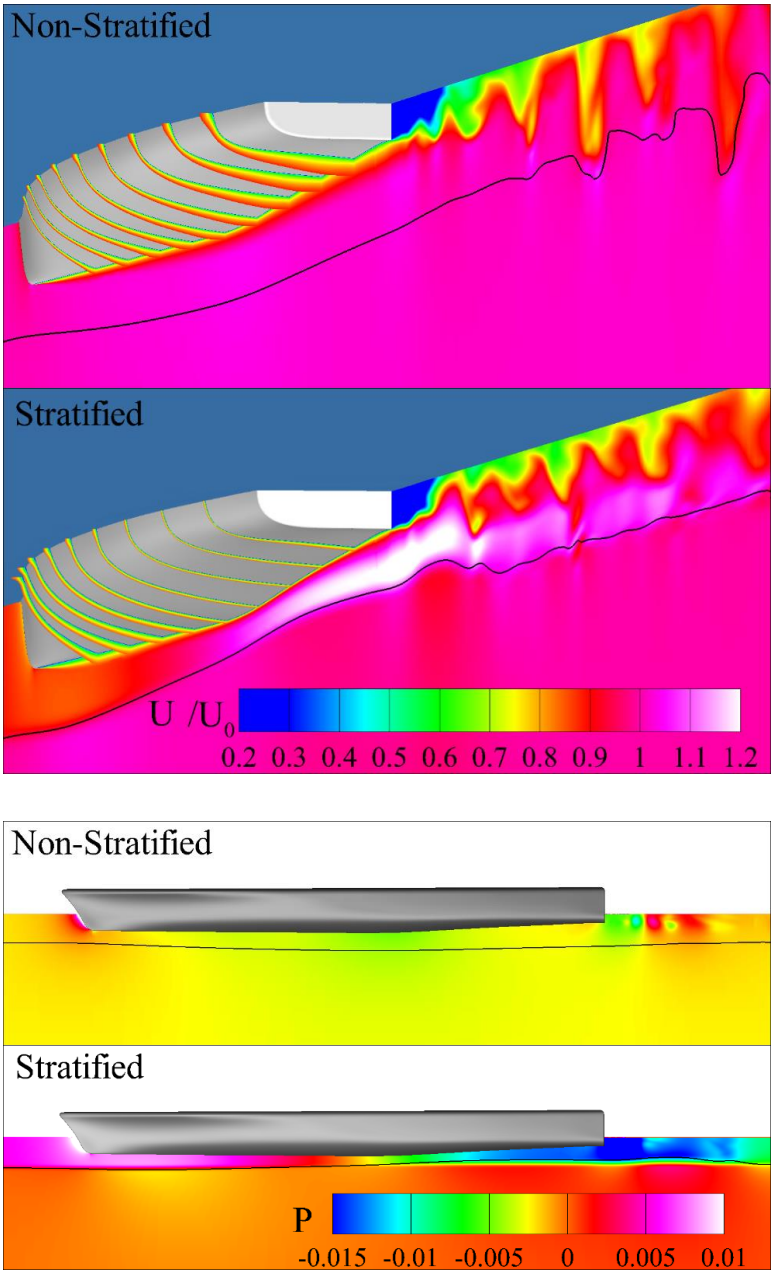

Figure 5.17: Boundary layer and vortical structures in the wake represented by axial velocity (top panels) and pressure (bottom panels) for $Fr_h = 0.91$ and $h/D = 1.5$. The line indicates the pycnocline (internal wave interface) for the stratified case, and an equivalent iso-surface for a transported passive scalar for the non-stratified case.

5.3.7 Wave and Resistance Dynamics

In previous sections, the simulations were performed for constant speed; however, due to the nature of the dead water phenomenon where the ships move with low speed, the hypothesis of constant speed of the ship cannot be reliable. As it is mentioned by Ekman (1904) the dead water is not stationary and there is a fluctuation in the ship speed due to the generation of internal waves and their breaking at the stern part of the ship. Towing the ship with constant force or using an engine with constant power allows the ship to move with varying speed, and the dead water phenomenon can be simulated more properly than the case of steady state. Therefore, the simulation is performed using a constant thrust force to evaluate the effect of stratification on total resistance.

The resistance reported in section 5.3.4 was obtained after running long enough to achieve a steady state or a statistically stationary value. In reality, an impulsive simulation where the ship speed is imposed suddenly to a system in rest involves an initially very large force as the geometry overcomes the virtual mass acceleration. There is then a transient as the boundary layer develops and the internal wave system evolves. Figure 5.18 shows the evolution of the resistance coefficient at different Fr_h for $h/D = 1.5$, highlighting the transient nature of the process. At low densimetric Froude number the resistance coefficient slowly decreases as approaches steady state. The opposite occurs at $Fr_h = 0.91$, where resistance grows slowly over time. Higher or intermediate densimetric Froude numbers attain final resistance coefficients faster, but still take 10~20 ship lengths to converge. After a relatively fast transient resulting from the formation of the boundary layer (occurring in 2~3 ship lengths), the transient behavior is dominated by the formation of the internal waves, which is a slow process.

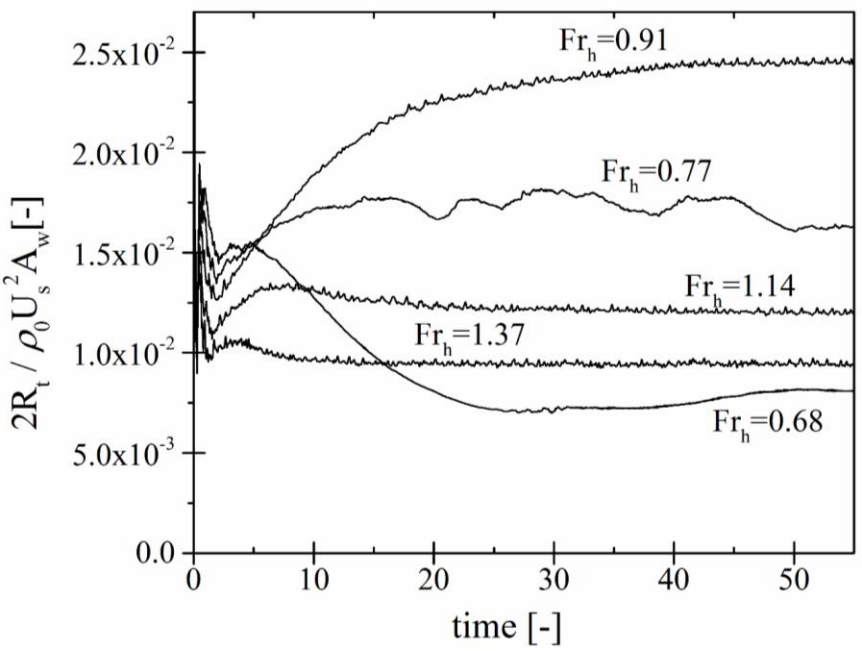

Figure 5.18: Time histories of resistance coefficients for different densimetric Froude numbers at $h/D = 1.5$.

To evaluate the impact of the internal wave dynamic response to the operation of a surface craft, consider a constant thrust propulsion system, with dimensionless thrust $C_T = T/\rho_0 U_0^2 L_0^2$. Figure 5.19 shows the resistance/velocity evolution for runs at constant dimensionless thrust $C_T = 5.0 \times 10^{-5}$, starting from rest with a pycnocline depth of $h/D = 1.5$. The symbols in Fig. 5.19 represent the steady-state resistance for each speed, which exhibits a local maximum of $R_t/(\rho_0 U_0^2 L_0^2) = 5.1 \times 10^{-5}$ at $U_s = 1.55$ *knots*, corresponding to $Fr_h = 0.91$ in Fig. 5.18. If the internal wave formed quickly, the ship should never be able to overcome the peak of resistance, since the imposed thrust is lower. However, the internal wave takes some time to form, and it causes an increase in resistance force. Thus a slow acceleration will result in higher resistances and a consequent added difficulty to overcome the dead water effect.

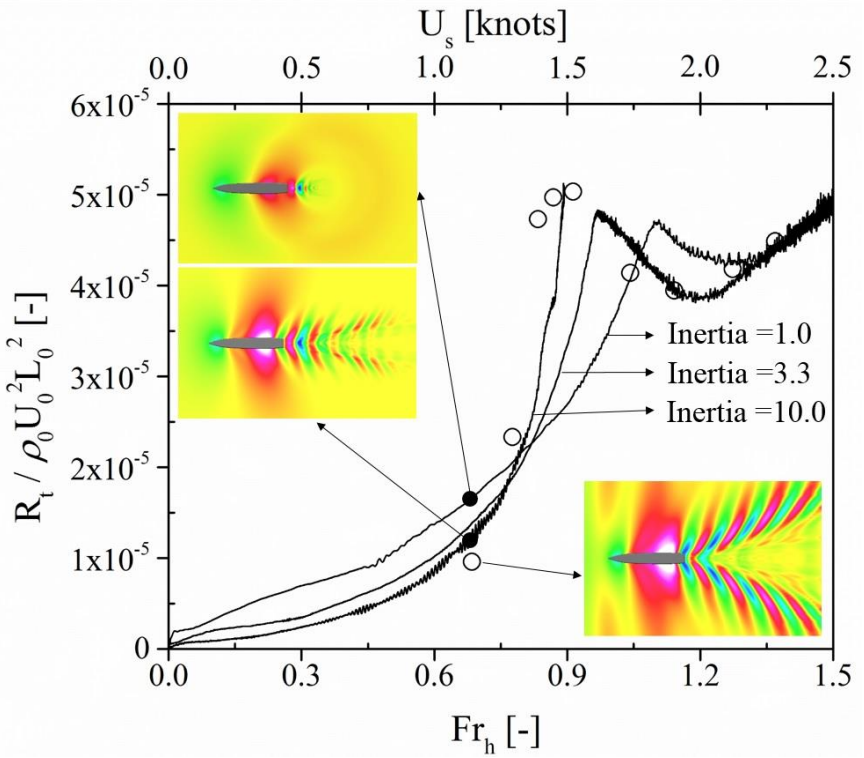

Figure 5.19: Evolution of speed and dimensionless resistance for constant thrust $C_T = 5.0 \times 10^{-5}$ simulations with different inertia at $h/D = 1.5$. Open symbols correspond to steady-state obtained imposing a constant speed (as in Fig. 5.12).

In Fig. 5.19 three accelerations at constant thrust are shown, resulting from three different inertia values: the actual inertia of the ship, 3.3 times the inertia of the ship and 10 times the inertia of the ship. The lowest acceleration case follows closely the steady-state resistance points and is unable to overcome the dead water resistance. In this case the resistance is lower than for faster accelerations at lower speeds, consistent with Fig. 5.18 that shows that the resistance decreases as the internal wave develops at low densimetric Froude numbers, and the resistance is higher at higher speeds where Fr_h approaches 0.91. Faster accelerations result in higher resistance at lower speeds and lower resistance at higher speeds, overcoming the peak in resistance at $Fr_h = 0.91$, transitioning to the unstable region of the resistance curve and accelerating until the resistance again equals the thrust at a higher

densimetric Froude number. The internal wave fields when the ship reaches $Fr_h = 0.7$ are shown in Fig. 5.19, with the fully developed internal wave field corresponding to an infinitely slow acceleration (equivalent to steady state at every ship speed), the slowest acceleration considered, for which the internal wave field is similar to the steady state near the vessel but has not been able to fully radiate to the whole domain, and a high acceleration, where the internal wave field is barely starting to form. The presence of the unstable negative slope resistance region in Fig. 5.19 causes hysteresis in the speed/resistance curve when operating at constant thrust, as well as problems maintaining speed between 1.5 and 2 *knots*. In this region a higher speed results in lower resistance, which causes acceleration of the ship unless the thrust is reduced. Conversely, lower speeds result in increased resistance, and deceleration of the ship unless the thrust is increased.

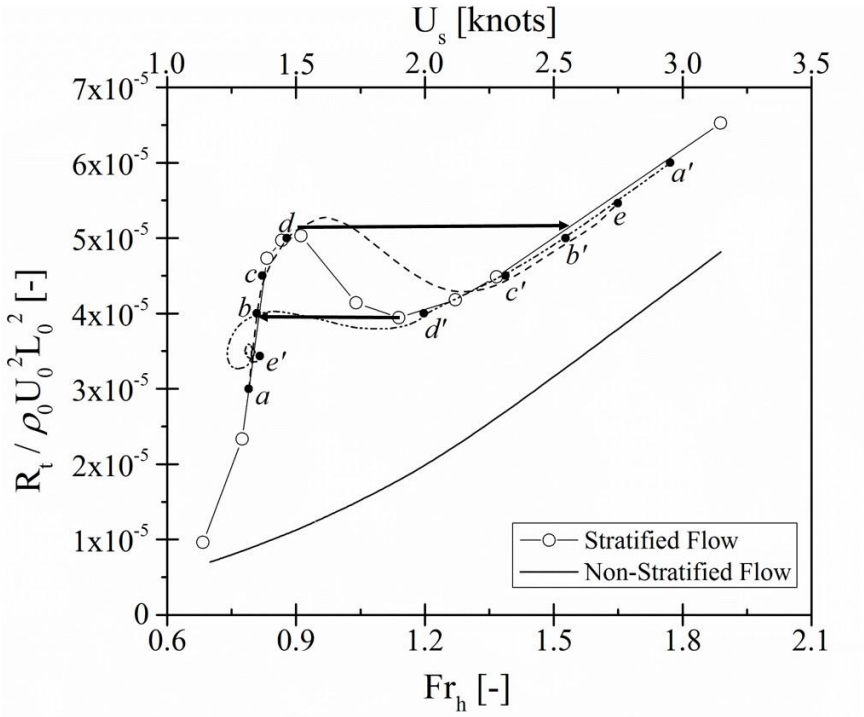

Figure 5.20: Resistance/speed curves and hysteresis at $h/D = 1.5$.

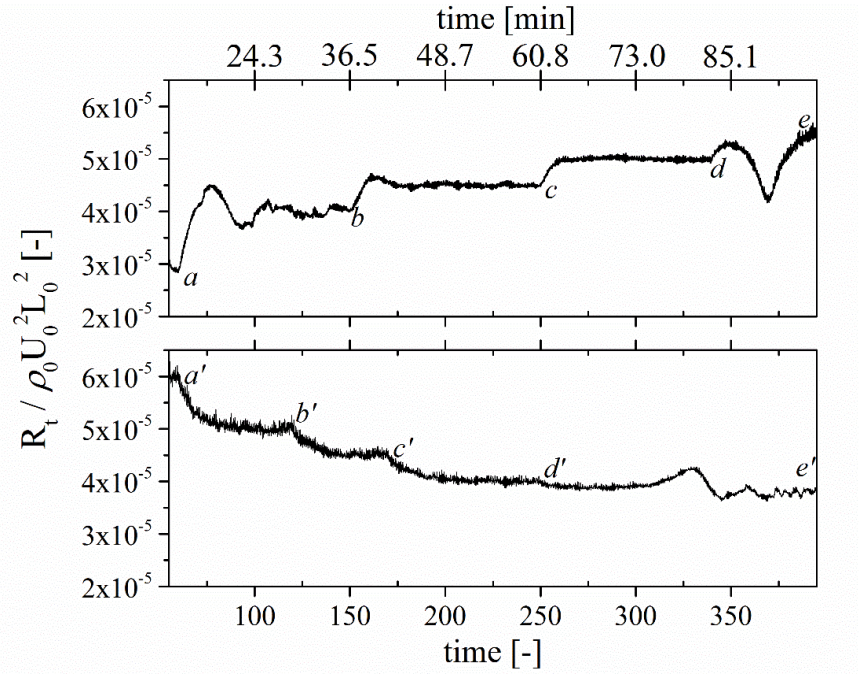

Figure 5.21: Resistance as a function of time for increasing (top) and decreasing (bottom) imposed thrust values.

Figure 5.20 shows the resistance/speed curves at $h/D = 1.5$ resulting from the step increases and decreases in thrust shown in Fig. 5.21. In Fig. 5.20 the empty symbol points indicate the steady-state resistance at each speed, and the full symbol points show the speed at each thrust force indicated in Fig. 5.21. Starting from $C_T = 3.0 \times 10^{-5}$, the dimensionless thrust is increased to 4.0×10^{-5} then , $4.5 \times 10^{-5}, 5.0 \times 10^{-5}$ and 5.5×10^{-5}, waiting for steady state to be reached before the next increase, simulating a slow increase in thrust. For thrust below the peak in steady-state resistance at $R_t/(\rho_0 U_0^2 L_0^2) = 5.1 \times 10^{-5}$ the resistance/speed curve follows well the steady-state curve (points (*a*), (*b*), (*c*) and (*d*) in Fig. 5.20). When the thrust is increased beyond the peak in steady-state resistance in the transition from points (*d*) to (*e*), the ship experiences initially a higher resistance than the steady-state resistance curve, since the internal wave needs some time to evolve to the new instantaneous speeds and was initially in the configuration offering the highest wave

resistance. The transition from points (*d*) to (*e*) runs through the unstable region of the resistance curve, resulting in a considerable jump in velocity from 1.55 to 2.74 *knots*. The change in the wave amplitude from point (*a*) to (*d*) can be seen in Figs. 5.22a-5.22b. It is interesting to note how the resistance force can be affected from point (*d*) to (*e*).

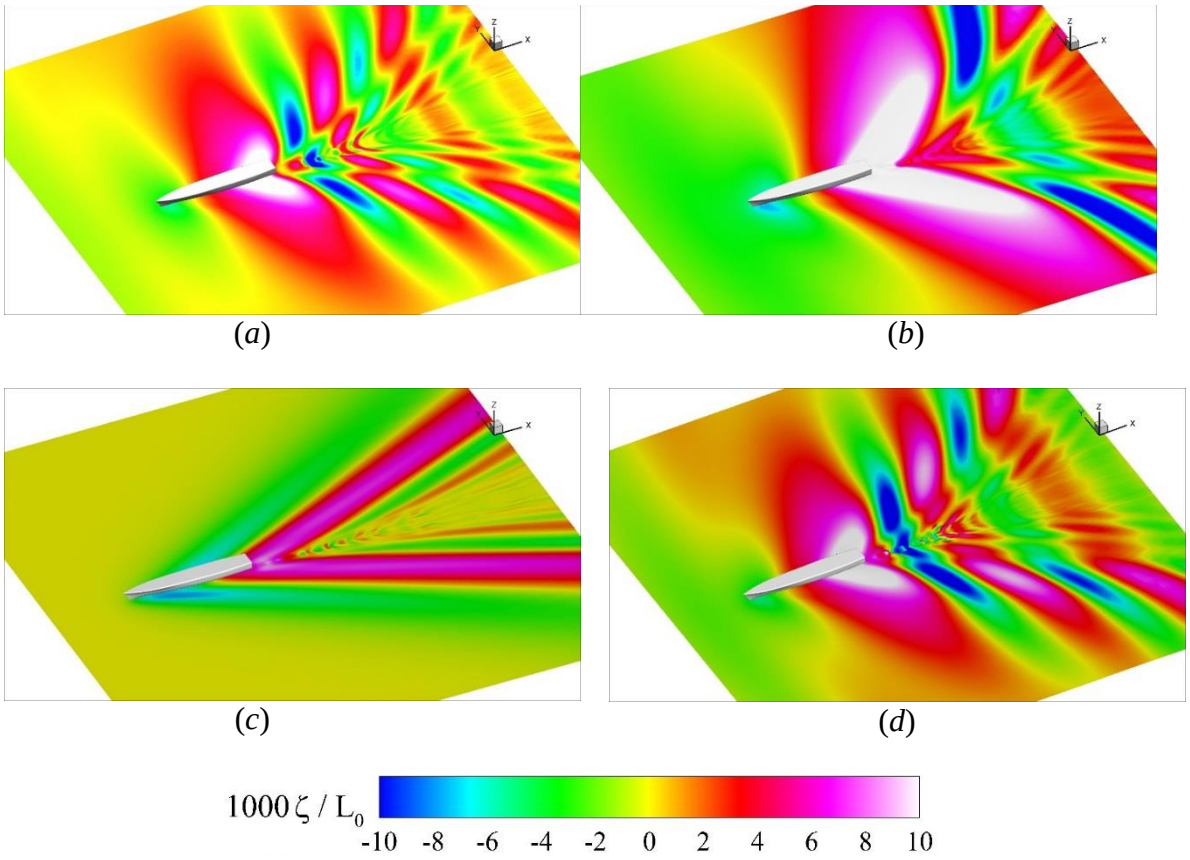

Figure 5.22: The internal wave elevation on interface for different resistance coefficients of (*a*) $C_T = 3.0 \times 10^{-5}$ (*b*) $C_T = 5.0 \times 10^{-5}$ (*c*) $C_T = 6.0 \times 10^{-5}$ (*d*) $C_T = 3.5 \times 10^{-5}$ in model scale. Wave elevation is shown as thousandths of ship length.

A series of step decreases in thrust, staring from steady-state at $C_T = 6.0 \times 10^{-5}$, and going through 5.0×10^{-5} then , $4.5 \times 10^{-5}, 4.0 \times 10^{-5}$ and 3.5×10^{-5}, results in similar behavior compared to increasing thrust. Prior to reaching the local minimum steady-state resistance at approximately $2\,knots$, the resistance evolves following the steady-state

resistance curve. When the thrust is decreased from point (*d'*) to (*e'*) the resistance cannot follow the unstable region of the curve and jumps from a velocity of 2 $knots$ to 1.5 $knots$. Note that since the transient resistance is higher than the final steady-state resistance the ship speed undershoots its final value in point (*e*'). Note in Fig. 5.21 that for each thrust increase the internal wave development and achieving steady-state takes several minutes in full scale, including the transition from point (*d*) to point (*e*). This jump through the unstable region of the resistance curve is so slow that a speed controller can easily maintain velocity even though it would require constant action. The change in the wave amplitude from point (*a'*) to (*d'*) can be seen in Figs. 5.22c-5.22d. The region between point (*d*) and (*d'*) with unstable condition is the region where the ship experiences the dead water phenomenon with a hysteretic behavior in ship speed.

5.4 Summary

The methodology implemented in the naval hydrodynamics code REX was used to simulate dead water phenomenon for R/V Athena advancing in a stratified fluid. The ship forward speed was drastically reduced to boost buoyancy forces and reproduce the effect of dead water. A large resistance increase of over six times the non-stratified value was observed. It was confirmed that the dead water effect is limited to a relatively narrow range of conditions; furthermore it was observed that for the more energetic flows (relatively weaker buoyancy with respect to inertia) the resistance is not only a function of Richardson number, and relative distance of the vessel to the density interface is important. A possible explanation for this disparity based on the observed flow features was presented.

CHAPTER 6 CONCLUSION AND FUTURE RECOMMENDATIONS

6.1 Conclusion

A methodology to compute density stratified flows in the near-field of ship and submarine wakes is presented. The approach uses a density transport equation and modifications to the mass and momentum conservation equations and turbulence model equations to include appropriate effects due to changes in density. Boundary and initial conditions are also modified to impose a background density distribution. The methodology was implemented in the naval hydrodynamics code REX. Tests were performed for the cases of a heated square cavity, for which also grid and time step studies were performed, and a sphere advancing in a stably stratified fluid, showing in both cases good agreement with available experimental or numerical data.

Simulations were performed for the research vessel Athena and the notional Joubert BB2 submarine advancing in a stratified fluid. The computations were performed for a relatively strong stratification condition measured at the Kitimat Bay Station, in the case of R/V Athena, and for two-layer hyperbolic tangent profiles for Joubert BB2. Density disturbances on the near wake for both were analyzed.

It is observed that these near-field wakes were mostly affected by two different processes for both vessels: the separation at the wet transom and propeller mixing in the case of R/V Athena, and the disturbance of the background density profile by the presence of the vessel for the case of the submarine. The generation of an internal wave for the surface ship case was not as evident from these simulations, as it was for the submarine. This was probably related to differences in stratification strength between the two cases, extension

and discretization levels of wake refinements and vertical location of the vessel with respect to the density profile. While vertical position could not be realistically changed for surface ships, the simulations presented for the submarine case showed clearly that distance to the pycnocline strongly affected the internal wave generation due to the presence of the vessel.

The generation of the internal waves required power that were reflected in an increase in resistance. This was shown clearly for the submarine, which was computed with the density change interface at two depths and also for a constant density. Moreover, when the interface was located deeper, immediately below the stern planes, produced a stronger internal wave and more resistance than when the interface was located at the propeller shaft plane.

The presence of a stratification interface against the solid surface of a hull had similar effects as those of a free surface in a juncture flow, where the boundary layer thickened due to the generation of streamwise vortices that took low velocity fluid from the boundary layer away from the hull. In the case of the submarine with the density interface at shaft depth this caused a significant velocity deficit into the propeller, which deformed considerably the vortical structures in the propeller wake.

Finally the dead water problem, in which under certain conditions a vessel advancing in a stratified fluid experiences a considerable increase in resistance respect to the equivalent case without stratification, was studied using computational fluid dynamics (CFD). The advance of a vessel in presence of a density interface (pycnocline) resulted in the generation of an internal wave that in the most adverse conditions could increase the total resistance coefficient by almost an order of magnitude. This thesis analyzed the effects of stratification on total and friction resistance, the near-field wake, internal and free surface

waves, and resistance dynamics. Some of these effects were reported for the first time, as limitations of previous efforts using potential flow were overcome by the use of a viscous free surface CFD solver. A range of densimetric Froude numbers from subcritical to supercritical were evaluated changing both the ship speed and pycnocline depth, using as platform the Research Vessel Athena. It was found that the presence of the internal wave caused a favorable pressure gradient, acceleration of the flow in the downstream of the hull, resulting in thinning of the boundary layer and increased of the friction resistance coefficient of up to 30%. The localized peak in resistance caused by the internal wave results in an unstable region which causes a hysteretic behavior in the resistance/speed curve when operating at constant thrust. The characteristic times of the resistance/speed are very slow, in the order of minutes, dominated by the time required to form the internal waves, thus making maintaining speed with an active controller possible.

6.2 Future Recommendations

As the future work it is recommended that presented simulation can be extended to focus on study of far-field wake produced by maritime vehicles advancing in a stable stratified fluid. The near-field wave behind the vehicle will be simulated and the solution will be used as the inlet condition for the far-field wakes. The methodology for approach is shown in Fig. 6.1.

The presented model consists of a scalar transport equation for the density, changes in the definition of the piezometric pressure to maintain a zero piezometric pressure in the far-field and free surface, and modifications to the turbulence model to account for turbulence generation or suppression by density gradients. For density changes caused by

variations in salinity or temperature, in which the water remains incompressible (meaning that pressure changes do not affect density), most terms needed are accounted for, including density changes in the momentum and continuity equations, but at this time the viscosity is still considered independent of density. Future work will include viscosity change effects too, though viscosity changes little with the salinity and temperature variations in the ocean.

Moreover, since both lid driven cavity problem and flow over sphere are laminar, the effect of the turbulence model implemented in to the code is not addressed. Though admittedly important, verification of a full turbulent case with density stratification can be considered as a future study.

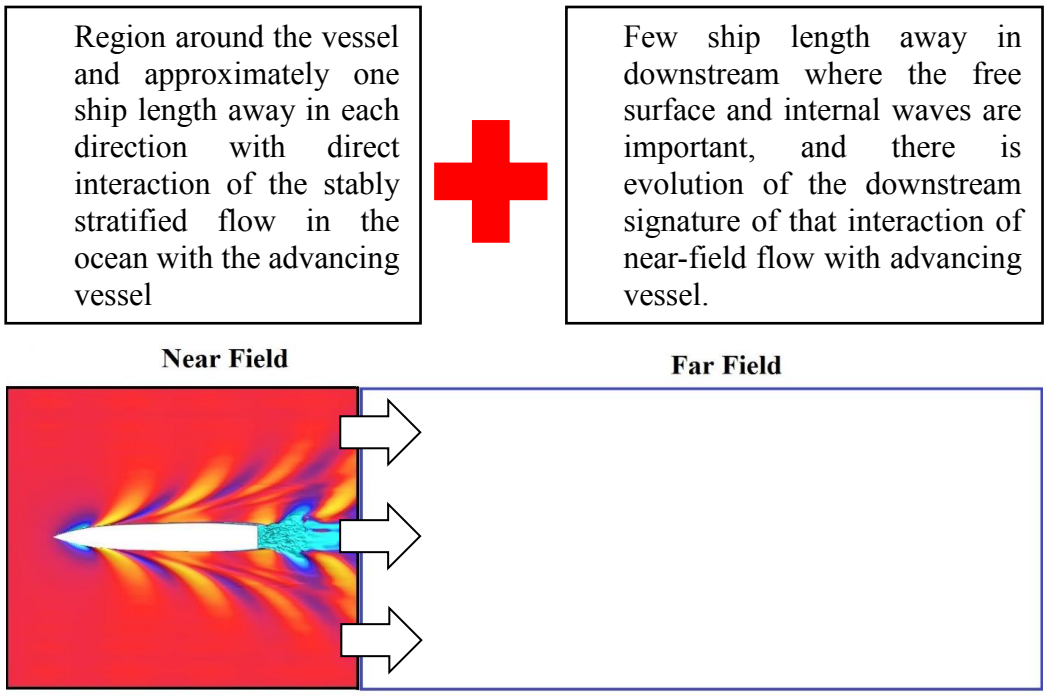

Figure 6.1: Coupling the near and far-field stratified flow solvers to simulate ship wake field by using input from the exit plane of the near-field to predict the internal waves in far-field.

REFERENCES

Al-Amiri, A. M., Khanafer, K. M., Pop, I., 2007. Numerical simulation of combined thermal and mass transport in a square lid-driven cavity. International Journal of Thermal Sciences 46:662-671.

Anderson, B., Chapuis, M., Erm, L., Fureby, C., Giacobello, M., Henbest, S., Jones, D., Jones, M., Kumar, C., Liefvendahl, M., Manovski, P., Norrison, D., Quick, H., Snowden, A., Valiyff, A., Widjaja, R., and Woodyatt, B., 2012. Experimental and computational investigation of a generic conventional submarine hull form. In 29th Symposium on Naval Hydrodynamics, Gothenburg, Sweden.

Ashok, A., Van Buren, T., Smits, A. J., 2015. Asymmetries in the wake of a submarine model in pitch. Journal of Fluid Mechanics 774: 416-442.

Bellevre, D., de Tuesta, A. D., Perdon, P., 2000. Submarine maneuverability assessment using computational fluid dynamic tools. In In Proc. 23th Symposium on Naval Hydrodynamics, Val de Reuil, France, 820-832.

Bettle, M. C., Gerber, A. G., Watt, G. D., 2009. Unsteady analysis of the six DOF motion of a buoyantly rising submarine. Computers & Fluids 38(9): 1833-1849.

Bettle, M. C., Gerber, A. G., Watt, G. D., 2014.Using reduced hydrodynamic models to accelerate the predictor–corrector convergence of implicit 6-DOF URANS submarine manoeuvring simulations. Computers & Fluids 102: 215-236.

Bhushan, S., Xing, T., Carrica, P. M., Stern, F., 2009. Model- and Full-Scale URANS Simulations of Athena Resistance, Powering, Seakeeping, and 5415 Maneuvering. Journal of Ship Research 53(4):179-198.

Bhushan, S., Xing, T., Stern, F., 2012.Vortical structures and instability analysis for Athena wetted transom flow with full-scale validation. Journal of Fluids Engineering 134 (3): 031201-18.

Boger, D., Dryer, J. 2006. Prediction of Hydrodynamic Forces and Moments for Underwater Vehicles Using Overset Grids. 44th AIAA Aerospace Sciences Meeting and Exhibit. Reno, Nevada, USA.

Bonneton, P., Chomaz, J. M., Hopfinger, E. J., 1993. Internal waves produced by the turbulent wake of a sphere moving horizontally in a stratified fluid. Journal of Fluid Mechanics 254: 23-40.

Boyer, D. L., Davies, P. A., Fernando, H. J. S., Zhang, X., 1989. Linearly Stratified Flow Past a Horizontal Circular Cylinder. Philosophical Transactions of the Royal Society of London. Series A, Mathematical and Physical Sciences 328(1601): 501-528.

Brucker, K. A., Sarkar, S., 2010. A comparative study of self-propelled and towed wakes in a stratified fluid. Journal of Fluid Mechanics 652: 373-404.

Carrica, P. M., Castro, A. M., Stern, F., 2010. Self-Propulsion Computations Using Speed Controller and Discretized Propeller with Dynamic Overset Grids. Journal of Marine Science and Technology 15: 316-330.

Carrica, P. M., Wilson, R. V., Stern, F., 2007a. An unsteady single-phase level set method for viscous free surface flows. International Journal for Numerical Methods in Fluids 53: 229-256.

Carrica, P. M., Wilson, R. V., Noack, R. W., Stern, F., 2007b. Ship motions using single-phase level set with dynamic overset grids. Computers & Fluids 36(9): 1415-1433.

Castro, A. M., Carrica, P. M., 2013. Bubble Size Distribution Prediction for Ship Flows: Model Evaluation and Numerical Issues. International Journal of Multiphase Flow 57: 131-150.

Chase, N., Carrica, P. M., 2013. Submarine Propeller Computations and Application to Self-Propulsion of DARPA Suboff. Ocean Engineering 60: 68-80.

Chase, N., Michael, T., Carrica, P. M., 2013. Overset simulation of a submarine and propeller in towed, self-propelled and maneuvering conditions. International Shipbuilding Progress 60 (1-4): 171-205.

Chen, C. W., Chen, C. Y., Yang, P. H. C., Chen, T. H., 2007. Analysis of experimental data on internal waves with statistical method. Engineering Computations: International Journal for Computer-Aided Engineering and Software 24(2): 116-150.

Chomaz, J. M., Bonneton, P., Butet, A., Hopfinger, E. J., Perriek, M., 1991. Gravity wave patterns in the wake of a sphere in a stratified fluid. In Proc. Turbulence 89: Organized Structures and Turbulence in Fluid Mech. (M. Lesieur, O. Mitais Eds.), 489-503. Kluwer.

Crapper, G. D., 1967. Ship waves in a stratified ocean. Journal of Fluid Mechanics 29(4): 667-672.

Crook, L. B., 1981. Powering Predictions for the R/V Athena (PG 94) Represented by Model 4950-1 with Design Propellers 4710 and 4711. David W. Taylor Naval Ship Research and Development Center, DTNSRDC/SPD-0833-05.

Day, W. G. Jr., Reed, A. M., Hurwitz, R. B., 1980. Full-Scale Propeller Disk Wake Survey and Boundary Layer Velocity Profile Measurements on the 154-Foot Ship R/V Athena. David W. Taylor Naval Ship Research and Development Center, DTNSRDC/SPD-0833-01.

Duchene, V., 2011. Asymptotic models for the generation of internal waves by a moving ship, and the dead-water problem. Nonlinearity 24: 2281-2323.

Ekman, H. W., 1904. On Dead Water. The Norwegian North Polar Expedition 1883-1886, Vol. V, Ch. XV, Christiania, Norway.

Fissel, D. B., Borg, K., Lemon, D. D., Brich, J. R., 2010. Marine Physical Environment, Enbridge Northern Gateway Project Technical Report, ASL Environmental Sciences Sidney, BC.

Hanazaki, H., 1988. A numerical study of three-dimensional stratified flow past a sphere. Journal of Fluid Mechanics 192: 393-419.

Hopfinger, E. J., Flor, J. B., Chomaz, J. M., Bonneton, P., 1991. Internal waves generated by a moving sphere and its wake in a stratified fluid. Experiments in Fluids 11: 255-261.

Huang, J., Carrica, P. M., Stern, F., 2008. Semi-coupled air/water immersed boundary approach for curvilinear dynamic overset grids with application to ship hydrodynamics. International Journal for Numerical Methods in Fluids 58(6): 591-624.

Hudimac, A. A., 1961. Ship waves in a stratified ocean. Journal of Fluid Mechanics 11: 229-243.

Grue, J., 2015. Nonlinear dead water resistance at subcritical speed. Physics of Fluids 27: 082103.

ITTC, 1978. Recommended Procedures and guidelines: 1978 ITTC Performance Prediction Method. International Towing Tank Conference Report 7.5-02-03-01.4.

Jenkins, D., 1984. Resistance Characteristics of the High Speed Transom Stern Ship R/V Athena in the Bare Hull Condition Represented by DTNSRDC Model 5365. Ship Performance Dept. Research & Development Report, DTNSRDC-84/024.

Johansen, P. J., Castro, M. A., Carrica, P. M., 2010. Full-Scale Two-Phase Flow Measurements on Athena Research Vessel. International Journal of Multiphase Flow 36(9): 720-737.

Kumar, C., Manovski, P., Giacobello, M., 2012. Particle Image Velocimetry Measurements on a Generic Submarine Hull Form. 18th Australasian Fluid Mechanics Conference Launceston, Australia.

Lacaze, L., Paci, A., Cid, E., Cazin, S., Eiff, O., Esler, J. G., Johnson, E. R., 2013. Wave patterns generated by an axisymmetric obstacle in a two-layer flow. Experiments in Fluids 54: 1618.

Li, J., Castro, A. M., Carrica, P. M., 2015a. A Pressure–Velocity Coupling Approach for High Void Fraction Free Surface Bubbly Flows in Overset Curvilinear Grids. International Journal for Numerical Methods in Fluids 79: 343-369.

Li, Y., Castro, A. M., Sinokrot, T., Prescott, W., Carrica, P. M., 2015b. Coupled CFD/Multibody Dynamics Approach for Wind Turbine Simulations. Renewable Energy 76: 338-361.

Lin, J. T., Pao, Y. H., 1973. Turbulent wake of a self-propelled slender body in stratified and non-stratified fluids: analysis and flow visualizations. Technical Report 11, Flow Research Inc.

Lin, J. T., Pao, Y. H., 1974a. The turbulent wake of a propeller-driven slender body in a stratified fluid. Technical Report 14, Flow Research Inc.

Lin, J. T., Pao, Y. H., 1974b. Velocity and density measurements in the turbulent wake of a propeller-driven slender body in a stratified fluid. Technical Report 36, Flow Research Inc.

Lin, J. T., Pao, Y. H., 1979. Wakes in stratified fluids. Annual Review of Fluid Mechanics 11: 317-338.

Lin, Q., Lindberg, W.R., Boyer, D. L., Fernando, H. J. S., 1992a. Stratified flow past a sphere. Journal of Fluid Mechanics 240: 315-354.

Lin, Q., Boyer, D. L., Fernando, H. J. S., 1992b. Turbulent wakes of linearly stratified flow past a sphere. Physics of Fluids A 4:1687-1696.

Lofquist, K. E. B., Purtell, L. P., 1984. Drag on a sphere moving horizontally through a stratified liquid. Journal of Fluid Mechanics 148: 271-284.

Longo, J., Huang, H. P., Stern, F., 1998. Solid/free surface juncture boundary layer and wake. Experiments in Fluids 25: 283-297.

Ma, H., Tulin, M. P., 1993. Experimental Study of Ship Internal Waves-The Supersonic Case. Journal of Offshore Mechanics and Arctic Engineering 115:16-22.

Martin, J. E., Esmaeilpour, M., Carrica, P. M., 2016. Near-Field Wake of Surface Ships and Submarines Operating in a Stratified Fluid. 31st Symposium on Naval Hydrodynamics, Monterey, CA.

Menter, F. R., 1994. Two-Equation Eddy-Viscosity Turbulence Models for Engineering Applications. AIAA Journal. 32:1598-1605.

Mercier, M. J., Vasseur, R., Dauxois, T., 2011. Resurrecting dead-water phenomenon. Nonlinear Processes in Geophysics 18: 193-208.

Meunier, P., Spedding, G. R., 2006. Stratified propelled wakes. Journal of Fluid Mechanics 552: 229-256.

Miles, J. W., 1961. On the stability of heterogeneous shear flow. Journal of Fluid Mechanics 10: 496-508.

Miloh, T., Tulin, M. P., 1988. A theory of dead-water phenomena. Proc. 17th Symposium on Naval Hydrodynamics, National Ac. Press.

Miloh, T., Tulin, M. P., Zilman, G., 1993. Dead-Water Effects of a Ship Moving in Stratified Seas. Journal of Offshore Mechanics and Arctic Engineering 115: 105-110.

Nansen, F., 1897. Farthest North: The Epic Adventure of a Visionary Explorer. Library of Congress Cataloging-in-Publication Data.

Nicolaou, D., Garman, J. F. R., Stevenson, T. N., 1995. Internal waves from a body accelerating in a thermocline. Applied Scientific Research 55(2): 171-186.

Noack, R., 2005. SUGGAR: A General Capability for Moving Body Overset Grid Assembly. 17th AIAA Computational Fluid Dynamics Conference, Toronto, ON, Canada.

Noack, R. W., Boger, D., Kunz, R., Carrica, P. M., 2009. Suggar++: An Improved General Overset Grid Assembly Capability. AIAA Paper 2009-3992. doi:10.2514/6.2009-3992.

Overpelt, B., 2015. Free Running Manoeuvring Model Tests on a Modern Generic SSK Class Submarine (BB2), PACIFIC 2015 International Maritime Conference, Sydney, NSW, Australia.

Phillips, A. B., Turnock, S. R., Furlong, M., 2010. Influence of turbulence closure models on the vortical flow field around a submarine body undergoing steady drift. Journal of Marine Science and Technology 15(3): 201-217.

Rabaud, M., Moisy, F., 2013. ShipWakes: Kelvin or Mach Angle?. Physical Review Letters-PRL 110, 214503.

Radko, T., 2001. Ship Waves in a Stratified Fluid. Journal of Ship Research 45(1): 1-12.

Schooley, A. H., Stewart, R. W., 1963. Experiments with a self-propelled body submerged in a fluid with a vertical density gradient. Journal of Fluid Mechanics 15(1): 83-96.

Shih, L., Koseff, J. R., Ivey, G. N., Ferziger, J. H., 2005. Parameterization of turbulent fluxes and scales using homogeneous sheared stably stratified turbulence simulations. Journal of Fluid Mechanics 525: 193-214.

Spedding, G. R., Browand, F. K., Fincham, A. M., 1996. Turbulence, similarity scaling and vortex geometry in the wake of a towed sphere in a stably stratified fluid. Journal of Fluid Mechanics 314: 53-103.

de Stadler, M. B., Sarkar, S., Brucker, K. A., 2010. Effect of the Prandtl number on a stratified turbulent wake. Physics of Fluids 22: 1-15.

de Stadler, M. B., Sarkar, S., 2012. Simulation of a propelled wake with moderate excess momentum in a stratified fluid. Journal of Fluid Mechanics 692: 28-52.

Stern, F., Kim, H. T., Patel, V. C., Chen, H. C., 1998. A Viscous-Flow Approach to the Computation of Propeller-Hull Interaction. Journal of Ship Research 32(4): 246-262.

Stern, F., Wilson, R. V., Coleman, H. V., Paterson, E. G., 2001. Comprehensive approach to verification and validation of CFD simulations - Part 1 and 2: methodology and procedures. ASME Journal of Fluids Engineering 124: 793-802.

Stevenson, T. N., 1973. The phase configuration of internal waves around a body moving in a density stratified fluid. Journal of Fluid Mechanics 60: 759-767.

Sutherland, B. R., 2005. Internal wave propagation. Modern Applied Mathematics (ed. J. C. Misra), 372-422. New Delhi: Narosa Press.

Thrope, S. A., 1973. Experiments on instability and turbulence in a stratified shear flow. Journal of Fluid Mechanics 61(4): 731-751.

Toxopeus, S., 2008. Viscous-flow calculations for bare hull DARPA SUB OFF submarine at incidence. International Shipbuilding Progress 55: 227-251.

Travin, A. Shur, M., Strelets, M., 2002. Physical and Numerical Upgrades in the Detached Eddy Simulation of Complex Turbulent Flows. Advanced in LES of Complex Flows. Friedrich, R. and Rodi, W., Editors, 239-254.

Tseng, Y. H, Ferziger, J. H., 2001. Mixing and available potential energy in stratified flows. Physics of Fluids 13(5): 1281-1293.

Tulin, M. P., Miloh, T., 1991. Ship Internal Waves in Shallow Thermocline: the Supersonic Case. Proceedings of the 18th Symposium on Naval Hydrodynamics, Ann Arbor, Michigan, 567-584.

Tulin, M. P., Miloh, T., Wang, P., 2000. The generation and propagation of ship internal waves in a generally stratified ocean at high densimetric froude numbers. Journal of Ship Research 44: 197-227.

Vasseur, R., Mercier, M., Dauxois, T., 2008. Dead Waters: Large amplitude interfacial waves generated by a boat in a stratified fluid, APS DFD Meeting, Gallery of Fluid Motion, http://hdl. handle.net/1813/11470.

Venayagamoorthy, S. K., Koseff, J. R., Ferziger, J. H., Shih., L. H., 2003. Testing of RANS turbulence models for stratified flows based on DNS data. Annual Research Briefs, Center for Turbulence Research, NASA-AMES, 127-138.

Wilcox, D. C., 1988. Reassessment of the scale-determining equation for advanced turbulence models. AIAA Joirnal, 26:1299-1310.

Winters, K.B., Lombard, P. N., Riley, J. J., D'asaro, E.A., 1995. Available potential energy and mixing in density-stratified fluids. Journal of Fluid Mechanics 289: 115-128.

Woodhead, T. J., 1983. The phase configuration of the waves around an accelerating disturbance in a rotating stratified fluid. Wave Motion 5: 157-165.

Xing, T., Carrica, P. M., Stern, F., 2010. Large-scale RANS and DDES computations of KVLCC2 at drift angle 0 degrees. Proceedings, Workshop on Numerical Ship Hydrodynamics, Gothenburg, Sweden.

Yeoh, G. H., Tu, J., 2010. Computational techniques for multi-phase flows. Butterworth-Heinemann/ IChemE.

Yeung, R. W., Nguyen, T. C., 1999. Waves generated by a moving source in a two-layer ocean of finite depth. Journal of Engineering Mathematics 35: 85-107.